THEORETICAL STUDIES OF STRUCTURAL AND ELECTRONIC PROPERTIES OF OVERLAYERS ON SEMICONDUCTOR SURFACES

Submitted by Mehmet Çakmak to the University of Exeter as a thesis for the degree of Doctor of Philosophy in Physics,

June, 1999

I certify that all material in this thesis which is not my own work has been identified and that no material is included for which a degree has previously been conferred upon me.

For my mother, my father and my sisters

Abstract

In this thesis we report the results of *ab initio* density functional calculations of equilibrium atomic geometry, electronic states and chemical bonding for the adsorption of elemental S and H_2S on chosen semiconductor surfaces. The results are in good agreement with the available experimental results and indicate the need for further experimental work.

In Chapter 2 of this thesis, I describe the formalism of the *ab initio* pseudopotential theory and the computational procedures which are used in this thesis. In the following chapter, a few experimental techniques are discussed, which we subsequently use their results to compare with our theoretical calculated results.

In Chapter 4 the passivation of S on InP(110) is investigated. Two sets of geometries are used; non-reacted geometries and reacted geometries. For non-reacted full-monolayer coverage, the epitaxially continued layer structure is found to be the most energetically favourable and it exhibits a good semiconducting nature. For an ordered reacted model with the adsorbate S atoms exchanged with their neighbouring P atoms, the average vertical distance between the top two layers is in agreement with x-ray standing wave analysis, but is characterized by a small band gap. In Chapter 5 adsorption of the H_2S molecule on the InP(110), GaAs(110) and GaP(110) surfaces is investigated within a dissociative adsorption model. In general the adsorption of H_2S on the three semiconductors shows similar behaviour. In Chapter 6 the adsorption of elemental S on Si(001) is investigated using three adsorption models; hemisulfide-(2×1) structure, monosulfide-(1×1) structure, and disulfide-(1×1) structure. An analysis of the surface free energy suggests that the monosulfide structure is more stable than the hemisulfide and disulfide structures. This result is also used to investigate the adsorption of elemental S on the Ge(001) surface. In Chapter 7, the adsorption of the H_2S molecule on the Si(001) and Ge(001) surfaces are investigated within two dissociative adsorption geometries. In both geometries studied in this thesis, the fundamental band gap is free of surface states, with the highest occupied state lying below the valence band maximum. In Chapter 8 the results are summarised and we outline possibilities for future work.

Contents

Acknowledgements . . . 8

List of Published Papers . . . 9

1 Introduction **23**

1.1 Introduction . . . 23

1.2 Bulk Semiconductors . . . 25

1.2.1 Diamond/Zinc-Blende Crystal Structures . . . 25

1.2.2 Bulk electronic states . . . 26

1.3 Semiconductors Surface . . . 27

1.3.1 Modelling surfaces within a repeated slab scheme . . . 29

1.3.2 Surface States . . . 30

1.3.3 Energy Gap . . . 31

1.3.4 Passivation of Surface States . . . 31

1.4 Sensitivity of results . . . 35

1.5 Summary of the structure of this thesis . . . 36

Bibliography . . . 38

2 Theory **41**

2.1 Introduction . . . 41

2.2 The fundamental problem . . . 41

2.3 Electron-Electron Interaction . . . 43

2.3.1 Wave-function Approaches . . . 43

2.3.1.1 Hartree Theory . . . 43

2.3.1.2 Hartree-Fock Theory . . . 44

2.3.2 Density functional Approaches . . . 45

2.3.2.1 Thomas-Fermi Theory 45

2.3.2.2 Density Functional Theory 45

2.3.2.3 Local Density Approximation 48

2.4 Electron-Ion interaction 49

2.4.1 All-electron methods 49

2.4.2 Pseudopotential method 50

2.5 Translation of electronic Kohn-Sham equations into momentum space 51

2.5.1 Structure factor 54

2.5.2 Non-local atomic form-factor 54

2.6 Energy derivative with respect to ionic position 57

2.7 Brillouin zone summation 58

2.8 Plane Wave LDA Code 59

2.9 Surface Brillouin Zone 61

2.9.1 Surface Brillouin Zone for the (110) surfaces 62

2.9.2 Surface Brillouin Zone for the (001) surfaces 64

2.10 Summary 65

Bibliography 66

3 Experimental Techniques 68

3.1 Introduction 68

3.2 Structural Measurements 69

3.2.1 Low Energy Electron Diffraction (LEED) 69

3.2.2 Reflection High Energy Electron Diffraction (RHEED) . . . 70

3.2.3 Scanning Tunneling Microscope (STM) 71

3.2.4 X-ray Standing Wave (XSW) 72

3.3 Surface Chemical Compositions 73

3.3.1 Photoelectron Spectroscopy (PS) 73

3.3.2 Auger Electron Spectroscopy (AES) 74

3.4 Summary 75

Bibliography 76

4 S-covered InP(110) surface **78**
4.1 Introduction 78
4.2 The clean (110) surface 79
4.2.1 Projected Bulk Band Structure 79
4.2.2 The III-V(110) surface 80
4.2.3 Atomic geometry, electronic states and chemical bondings for the clean InP(110) surface 82
4.3 The S-deposited InP(110) surfaces 83
4.3.1 Non-reacted surface structures 85
4.3.1.1 Full monolayer coverage 85
4.3.1.2 Half monolayer coverage 91
4.3.2 Reacted surface structures 93
4.3.2.1 Exchange Model 94
4.3.2.2 Diffuse-reacted and other models 98
4.4 Summary 100
Bibliography 102

5 Adsorption of H_2S on InP(110), GaAs(110) and GaP(110) **104**
5.1 Introduction 104
5.2 The H_2S-deposition models on the III-V(110) surfaces 105
5.3 H_2S-deposition onto InP(110) 109
5.3.1 Atomic Geometry 109
5.3.2 Electronic states and Chemical bondings 110
5.4 H_2S-deposition onto GaAs(110) 113
5.4.1 Atomic Geometry 113
5.4.2 Electronic states and Chemical bondings 115
5.5 H_2S-deposition onto GaP(110) 117
5.5.1 Atomic Geometry 117
5.5.2 Electronic states and Chemical bondings 118
5.6 Discussion of results for H_2S adsorption on InP, GaAs and GaP . . 119
5.7 Summary 120
Bibliography 122

6 Adsorption of S on Si(001) and Ge(001) 124

6.1 Introduction . . . 124
6.2 The Clean IV-(001)-(2×1) surfaces . . . 126
6.3 S adsorption on IV(001) . . . 127
6.3.1 Atomic geometries, Electronic states and Chemical bondings 128
6.3.1.1 Hemisulfide-Si(001)-(2×1) . . . 128
6.3.1.2 Monosulfide-Si(001)-(1×1) . . . 132
6.3.1.3 Disulfide-Si(001)-(1×1) . . . 134
6.3.2 Relative stability of hemi-, mono- and disulfide phases . . . 138
6.4 S adsorption on Ge(001) . . . 140
6.4.1 Atomic geometries, Electronic states and Chemical bondings 140
6.4.1.1 Monosulfide-Ge(001)-(1×1) . . . 141
6.5 Summary . . . 145
Bibliography . . . 146

7 H_2S on Si(001) and Ge(001) 149

7.1 Introduction . . . 149
7.2 Results and Discussions . . . 150
7.2.1 The monohydride-IV(001)-(1×2) surface . . . 150
7.2.2 Partially dissociated H_2S on Si(001) and Ge(001) . . . 153
7.2.2.1 H_2S on Si(001)-(1×2) . . . 156
7.2.2.2 H_2S on Ge(001)-(1×2) . . . 157
7.2.3 Fully dissociated H_2S on Si(001) and Ge(001) . . . 160
7.2.3.1 H_2S on Si(001)-(1×2) . . . 160
7.2.3.2 H_2S on Ge(001)-(1×2) . . . 163
7.2.4 Monolayer deposition of elemental sulfur on Ge(001)-(1×1) . 164
7.3 Summary . . . 165
Bibliography . . . 166

8 Concluding Remarks 168

8.1 Summary of Results . . . 168
8.2 Future Work . . . 170

8.2.1 Adsorption of Te on Si(001) 170
8.2.2 Si_2H_6 and Ge_2H_6 on the group-IV(001) surfaces 170
8.2.3 Growth Simulations 171
Bibliography 173

Acknowledgements

This work would not have been successfully completed without the unsparing and conscientious help of a few very important persons. First and foremost, I wish to express my sincere gratitude to my supervisor, Dr. G. P. Srivastava, for his invaluable academic as well as unfailing moral support, without which this thesis would not have been possible. Under his guidance, I have learned not only a great deal of physics but also how to teach, work hard and communicate effectively. Equally important has been the support and hospitality that I have received during my time in Exeter from the Srivastava family. I would also like to thank Prof. J. C. Inkson, head of the School of Physics, for providing support and all the necessary facilities for my Ph.D. research. I wish also to express my thanks to Dr. T. W. Preist for his constant support. I would also like to thank Dr. J. M. Rowe for his valuable technical support.

I wish to express my sincere thanks to the University of Gazi, Turkey, for award of a studentship.

Thanks are extended to several dear friends on the second floor of the school of physics, Exeter, their collaborations and helps during my time in Exeter, specially Steve, Hüseyin, Simon, Binoy, Andrew and J. Matthias and the other members of the second floor.

Outside England, many thanks to Prof. Dr. Kemal Çolakoğlu and Prof. Dr. Atilla Özmen. I would also thank Doç. Dr. E. Kasap, Doç. Dr. S. Özçelik, Mr. M. T. Güllüoglu and Mr. G. Ugur for helping to make the logistics of this Ph.D. more straightforward.

Special thanks are due to my mother, father, sisters, brothers in-law, nephew, nieces as I could never have completed this thesis without their love and support, I simply could not have come this far.

List of Published Papers

Portions of Chapters 4-7 have appeared in the following published articles, listed in reverse chronological order:

1. 'Adsorption of partially and fully dissociated H_2S molecule on the Si(001) and Ge(001) surfaces', M. Çakmak and G. P. Srivastava, *in press* Phys. Rev. B, (1999).

2. 'Ab initio study of the adsorption of H_2S onto the Si(001) surface', M. Çakmak and G. P. Srivastava, *in press* Surf. Sci., (1999).

3. 'Adsorption and desorption of S on and off Si(001) studied by Ab initio Density Functional Theory', M. Çakmak and G. P. Srivastava, J. Appl. Phys. 84, 6070 (1998).

4. '*Ab initio* study of atomic geometry, electronic states and bonding for H_2S-adsorption on III-V(110)-(1×1) surfaces', M. cCakmak and G. P. Srivastava, Phys. Rev. B 57, 4486 (1998).

5. 'Theoretical study of the GaAs(110)-(1x1)-H_2S surface, M. Çakmak and G. P. Srivastava, Sur. Sci. 404, 658 (1998).

6. 'An *ab initio* calculation of the adsorption of H_2S onto InP(110)-(1×1) surface', M. Çakmak and G. P. Srivastava, Appl. Sur. Sci. 123/124, 52 (1998).

7. 'Structural, electronic and vibrational properties of the InSb(110) surface', H. M. Tütüncü, M. Çakmak and G. P. Srivastava, Appl. Surf. Sci. 123/124, 146 (1998).

8. 'Calculation of atomic geometry, electronic states and bonding for the S-deposited InP(110) surface', M. Çakmak and G. P. Srivastava, Phys. Rev.

B 56, 1928 (1997).

9. 'A theoretical study of sulphur adsorption on InP(110)', M. Çakmak and G. P. Srivastava, Sur. Sci. 377, 592 (1997).

List of Figures

1.1 (a) The zinc-blende structure. (b) The face-centred cubic structure. The zinc-blende structure becomes the diamond structure when cations and anions are identical. 26

1.2 Electronic bulk band structure of (a) GaAs and (b) Si, calculated by pseudopotential technique. Occupied and unoccupied surface states are shown by thick and thin curves, respectively. The symmetry points in the Brillouin zone are explained in chapter 2. 28

1.3 Si atomic structure of the (001) face. Schematic representation of bulk region, surface region, vacuum region and dangling bonds. . . . 29

1.4 A model surface super cell. 30

1.5 Electronic energy levels for (a) an undoped semiconductor sample, (b) band bending and Fermi level pinning at equilibrium (i.e. Schottky barrier), and (c) band bending and Fermi level pinning at equilibrium (i.e. Ohmic contact). 33

2.1 Nonlocal ionic pseudopotential for In and P generated using Bachelet *et al.* The potentials for angular momentum l=0, l=1, and 2 are shown. The dash line represents the Coulomb (All-electron) potential. 56

2.2 The first Brillouin zone of a face-centred cubic lattice. 62

2.3 Surface Brillouin zones for the primitive (1×1) unit cell for the (a) (110), (b) (001) surfaces and (c) for the (2×1) unit cell of the (001) surface. 64

3.1 Schematic drawing of a LEED apparatus. 70

3.2 Simple presentation of the diffracted beams from a crystal. 73

3.3 Simple presentation of absorption by a single atom of photon and emission of a photo electron. 74
3.4 Schematic Auger Electron transition. At energy level E_1 the electrons are expelled by either an impinging electron or a photon, leaving a hole. An electron from E_2 may fall into the hole at E_1 and the energy thus released is absorbed by another electron which gets ejected from the solid. The second electron is called the Auger electron. 75

4.1 Projected bulk spectrum is shown by hatched regions. 80
4.2 Schematic (a) top and (b) side views of the surface geometry of the III-V(110) surface. 81
4.3 Schematic side view of the relaxed surface geometry of the InP(110) surface. The relaxation parameters refer to Tab. 4.1. 83
4.4 Electronic band structure of the clean InP(110) surface. Projected bulk spectrum is shown by hatched regions. Occupied and unoccupied surface states are shown by thick and thin curves, respectively. The angle-resolved photoemission results are indicated by open circles [16]. 84
4.5 Schematic side views and top views of surface geometries for non-reacted S overlayers on InP(110). (a), (b) and (c) show the ECLS, EOTS, and S-dimer at the P-site, respectively for 1 ML coverage. (d), (e) and (f) show the interchain bridging structure, modified epitaxial on-top structure with bonding only to In, and epitaxially continued layer structure with bonding only to In (the so-called 'defect' model), respectively for 1/2 ML coverage. 86
4.6 Schematic side views and top views of surface geometries for reacted S overlayers on InP(110): (a) and (b) are the exchange-reacted and the diffused-reacted, (c) and (d) are the substitution and substitution-adatom model, respectively. 87
4.7 Schematic detailed side view of relaxed atomic geometries for the InP(110)/S for (a) the ECLS, (b) the interchain bridging. 88

4.8 Electronic band structure of the InP(110)-S interface: for the 1 ML ECLS geometry. Projected bulk spectrum is shown by hatched regions. Occupied and unoccupied surface states are shown by thick and thin curves, respectively. 90

4.9 Electronic total charge density plots for the ECLS in (a) a vertical plane containing the P-S bond, (b) in a vertical plane containing the In-S bond. The charge density values are normalised to 80 electrons per unit cell volume of 631.26 Å^3. 91

4.10 Electronic total charge density plots for the ECLS in along the line joining the two S atoms. The charge density values are normalised to 80 electrons per unit cell volume of 631.26 Å^3. 92

4.11 Electronic charge density plots for the highest occupied (a) and lowest unoccupied (b) states at the InP(110)-S (1 ML ECLS) interface at $\bar{M}$. The contour values are normalised to 2 electrons per unit cell volume of 631.26 Å^3. 92

4.12 Electronic band structure of the InP(110)-S interface: for the 1/2 ML interchain bridging geometry. Projected bulk spectrum is shown by hatched regions. Occupied and unoccupied surface states are shown by thick and thin curves, respectively. 94

4.13 Total charge density along the S-In and S-P bonds for the 1/2 ML interchain bridging geometry, with normalisation of 76 electrons per unit cell volume of 631.26 Å^3. 95

4.14 Schematic detailed side view of relaxed atomic geometries for the InP(110)/S for (a) exchange-reacted and (b) diffuse-reacted models. 96

4.15 Electronic band structure of the InP(110)-S interface: for the exchanged-reacted geometry. Projected bulk spectrum is shown by hatched regions. Occupied and unoccupied surface states are shown by thick and thin curves, respectively. 97

4.16 Electronic total charge density plots for the exchange-reacted in (a) a vertical plane containing the P-S bond, (b) in a vertical plane containing the In-S bond. The charge density are normalised to 76 electrons per unit cell volume of 631.26 Å^3. 98

4.17 Electronic total charge density plots for the exchange-reacted in along the line joining the P and S atoms in the top layer. The charge density are normalised to 76 electrons per unit cell volume of 631.26 Å^3. 99

4.18 Electronic band structure of the InP(110)-S interface: for the diffuse-reacted geometry. Projected bulk spectrum is shown by hatched regions. Occupied and unoccupied surface states are shown by thick and thin curves, respectively. 100

5.1 Schematic side view for the H_2S adsorption on III-V(110), (a) Model I as proposed by Dudzik *et al.* [11] and (b) Model II as proposed by us. 107

5.2 Schematic relaxed atomic geometry for Model II of H_2S adsorption on III-V(110) with the key parameters, (a) side view and (b) top view. 108

5.3 Electronic band structure of the InP(110)-H_2S interface. The projected bulk spectrum is shown by hatched regions. The calculated electronic states are shown by thick curves and the experimental results of Dudzik *et al.* [14] are indicated by open symbols. The experimental data has been rigidly shifted upwards by 0.5 eV as discussed in the text. 111

5.4 Electronic total charge density plots of the InP(110)-H_2S interface in (a) a vertical plane containing the P-H^+ bond, and (b) a vertical plane containing the S-H^- bond. The contour values are normalised to 72 electrons per unit cell volume of 631.26 Å^3. 112

5.5 Electronic charge density plots for individual surface states for the relaxed geometry of the InP(110)-H_2S interface: (a) S_1 and (b) S_2 at $\bar{M}$ in a horizontal plane. The contour values are normalised to 2 electrons per unit cell volume of 631.26 Å^3. 113

5.6 Electronic charge density plots for individual surface states for the relaxed geometry of the InP(110)-H_2S interface: (a) S_3 at $\bar{M}$ (b) S_4 at $\bar{M}$ in a horizontal plane. The contour values are normalised to 2 electrons per unit cell volume of 631.26 Å^3. 114

5.7 Electronic charge density plots for individual surface states for the relaxed geometry of the InP(110)-H_2S interface: S_5 at $\bar{M}$ in a vertical plane. The contour values are normalised to 2 electrons per unit cell volume of 631.26 Å^3. 115

5.8 Electronic band structure of the GaAs(110)-H_2S interface. The projected bulk spectrum is shown by hatched regions. The calculated electronic states are shown by thick curves and the experimental results of Dudzik *et al.* [11] are indicated by solid symbols. 116

5.9 Electronic charge density plots for individual surface states for the relaxed geometry of the GaAs(110)-H_2S interface: (a) S_2 (b) S_3, and (c) S_4 at $\bar{M}$ in a horizontal plane. The contour values are normalised to 2 electrons per unit cell volume of 631.26 Å^3. 117

5.10 Electronic band structure of the GaP(110)-H_2S interface. The projected bulk spectrum is shown by hatched regions and the electronic states are shown by thick curves. 118

5.11 Electronic charge density plots for individual surface states for the relaxed geometry of the GaP(110)-H_2S interface: (a) S_3 at $\bar{M}$ (b) S_4 at $\bar{M}$. The contour values are normalised to 2 electrons per unit cell volume of 631.26 Å^3. 119

6.1 Top view of the outermost atomic layers of IV(001) for (a) the ideal bulk geometry, (b) the surface dimer model. 126

6.2 Schematic side view of the equilibrium geometries for the surface dimers at (a) the clean Si(001)-(2×1) and (b) the clean Ge(001)-(2×1) surface. 127

6.3 Surface states on Si(001)-(2×1). The dashes curves are symmetric dimer formation for the clean Si(001). The full curves are asymmetric dimer formation for the clean Si(001). 128

6.4 Schematic top view of S adsorption on the Si(001) surface, (a) the S-(2×1) (hemisulfide) structure on the Si(001)(2×1) surface, (b) the S-(1×1) (monosulfide) structure on the (1×1) surface, and (c) the S-(1×1) (disulfide) structure on the (1×1) surface: the first S atoms are bonded to the first layer Si atoms and the second S atoms are bonded to the second layer Si atoms. 129

6.5 Schematic side view of relaxed geometries of (a) hemisulfide Si(001)-(2×1), (b) monosulfide Si(001)-(1×1), and (c) disulfide Si(001)-(1×1). 131

6.6 Electronic band structure of hemisulfide Si(001)-(2×1) structure. The shadded region is the bulk (2×1) projected band structure for Si, the thick line is the occupied surface band. 132

6.7 Electronic total charge density and electronic charge density plots of the individual state for hemisulfide Si(001)-(2×1) structure. (a) On the plane cutting vertically through the Si atoms with S (Plane 1), and (b) on the plane cutting obliquely through the Si atoms so as to include the S-Si bonds (Plane 2). (c) The highest occupied surface state at $\bar{K}$, shown in Plane 1. The electron charge density is normalised to the number of electrons in the supercell (i.e. 74 electrons per unit cell for total charge density plots and 2 electrons per unit cell for the individual electronic states). 133

6.8 Electronic band structure of the S(1 ML)-Si(001)-(1×1) structure. The shadded region is the bulk (1×1) projected band structure for Si, the thick lines are the occupied surface bands and the thin line the unoccupied band. 135

6.9 Electronic total charge density and electronic charge density plots of the individual states for the S(1 ML)-Si(001)-(1×1) structure. (a) On the plane cutting vertically through the Si atoms with S (Plane 1), (b) the surface state S_1 for Plane 1 at $\bar{K}$, (c) the surface state S_2 at $\bar{K}$, on the plane cutting horizontally through the S atoms so as to included the S and the next S neighbors, and (d) the unoccupied surface state S_3 for Plane 1 at $\bar{J}$. The electron charge density is normalised to the number of electrons in the supercell (i.e. 40 electrons per unit cell for total charge density plots and 2 electrons per unit cell for the individual electronic states). 136

6.10 Electronic total charge density plots for the S(2 ML)-Si(001)-(1 × 1) structure. (a) On the plane cutting vertically through the Si atoms with S, and (b) on the plane cutting obliquely through the Si atoms with embedded the S atom. The electron charge density is normalised to the number of electrons in the supercell (i.e. 46 electrons per unit cell). 137

6.11 Schematic representation of the S_8 ring. ω_1 is the S-S-S angle, and ω_2 is the dihedral angle between successive SSS planes. Calculated structural parameters are in anstromgs (Å) and degrees. 139

6.12 Surface free energy of S/Si(001)-(2 × 1) plotted against $\mu_{\mathrm{S}} - \mu_{\mathrm{S}}^{\mathrm{bulk}}$. . 141

6.13 Calculated band structure of the 1 ML S coverage on the Ge(001)-(1×1) surface. The shaded region is the bulk (1×1) projected band structure for Ge and the thick lines represent the occupied surface bands and thin line is the lowest unoccupied surface bands. Full circles represents sharp and open circles weak feature in the ARPES spectra [33]. 142

6.14 Electronic total charge density for monosulfide Ge(001)-(1×1) structure. (a) On the plane cutting vertically through the Ge atoms with S (Plane 1), and (b) on the plane cutting horizantally through the S atoms so as to included the S and the next S neighbors (Plane 2). The electron charge density is normalised to the number of electrons in the supercell (i.e. 40 electrons per unitcell for total charge density plots). 143

6.15 Electronic charge density plots of the individual states for the 1 ML S on the Si(001)-(1×2) surface: on the plane cutting vertically through the S atom and the Si atoms, (a) the surface state S_1^s at $\bar{M}$, (b) the surface state S_2^s at $\bar{M}$, (c) the surface state S_3^s at $\bar{\Gamma}$ and (d) the surface state S_4^s at $\bar{M}$, (e) surface state S_5^s at $\bar{M}$, on the plane cutting horizontally through the S atoms and the H atoms, (f) the surface state S_6^s at $\bar{M}$ and (g) the lowest unoccupied surface state S_7^s at $\bar{M}$. The electron charge density is normalised to the number of electrons (i.e. 2 electrons per unit cell for the individual electronic states). . 144

7.1 Schematic side view of (a) monohydride, (b) and (c) possible partially dissociated H_2S geometries, and (d) fully dissociated H_2S geometry on IV(001). 151

7.2 Schematic side view with the key structural parameters for (a) monohydride-IV(001)-(1×2), (b) partially dissociated H_2S on IV(001)-(1×2), and (c) fully dissociated H_2S on IV(001)-(1×2). 152

7.3 (a) Bonding picture of the SiH_4 molecule. Other H atoms are in another plane. (b) One-dimensional charge density plot between Si and H. The maximum charge density is towards the H atom. The charge density values are normalised to 8 electrons per unit cell volume. 154

7.4 Calculated band structure of the hydrogen-terminated H-Si(001)-(1×2) surface. The shaded region is the bulk (1×2) projected band structure for Si and the thick lines represent the occupied surface states. 155

7.5 Electronic total charge density and electronic charge density plots of the individual states for the monohydride Si(001)-(1×2) structure: (a) on the plane cutting vertically through the Si atoms with the H atoms, (b) the surface state S_1 at $\bar{J}'$, (c) the surface state S_2 at $\bar{K}$, (d) the surface state S_3 at $\bar{K}$ and (e) the surface state S_4 at $\bar{K}$. The electron charge density is normalised to the number of electrons in the supercell (i.e. 70 electrons per unit cell for total charge density plot and 2 electrons per unit cell for the individual electronic states). 155

7.6 Calculated band structure of the partially dissociated H_2S on the Si(001)-(1×2) surface. The shaded region is the bulk (1×2) projected band structure for Si and the thick lines represent the occupied surface bands. 157

7.7 Electronic total charge density and electronic charge density plots of the individual states for partially dissociated H_2S on Si(001)-(1×2) structure: (a) on the plane cutting vertically through the Si atoms with $(SH)^-$ line and SiH^+, (b) the surface state S_1 at $\bar{K}$, (c) the surface state S_2 at $\bar{K}$, (d) the surface state S_3 at $\bar{K}$ and (e) the surface state S_4 at $\bar{K}$ and (f) the surface state S_5 at $\bar{K}$. The electron charge density is normalised to the number of electrons in the supercell (i.e. 76 electrons per unit cell for total charge density plot and 2 electrons per unit cell for the individual electronic states). 158

7.8 Calculated band structure of the partially dissociated H_2S on the Ge(001)-(1×2) surface. The shaded region is the bulk (1×2) projected band structure for Ge and the thick lines represent the occupied surface bands. 159

7.9 Calculated band structure of the fully dissociated H_2S on the Si(001)-(1×2) surface. The shaded region is the bulk (1×2) projected band structure for Si and the thick lines represent the occupied surface bands. 161

7.10 Electronic total charge density and electronic charge density plots of the individual states for the fully dissociated H_2S on Si(001)-(1×2) structure: (a) on the plane cutting vertically through the S atom and the Si atoms with the SiH lines, (b) the surface state S_1 at $\bar{K}$, (c) the surface state S_2 at $\bar{K}$, (d) the surface state S_3 at $\bar{K}$ and (e) the surface state S_4 at $\bar{K}$ and (f) surface state S_5 at $\bar{K}$, on the plane cutting horizontally through the S atoms and the H atoms. The electron charge normalisation is the same as in Fig. 7.7. 162

7.11 Calculated band structure of the fully dissociated H_2S on the Ge(001)-(1×2) surface. The shaded region is the bulk (1×2) projected band structure for Ge and the thick lines represent the occupied surface bands. 164

List of Tables

1.1 Calculated energy gaps for Si using different kinetic energy cut-offs. Experimental lattice parameters for Si is taken as 5.43 Å [28]. The calculated lattice parameter for Si is taken as 5.42 Å. The experimental energy gap at 0 K is 1.17 eV. 34

1.2 Experimental [36] and theoretical lattice constants (a) and energy gaps (E_g) [28] for homopolar and heteropolar type semiconductors versus theoretical calculated values. The i and d refer to inderect and direct gaps. Theoretical calculated values have been made using 12 Ry kinetic energy cut-off. 36

4.1 Structural parameters of the InP(110) surface. These parameters are indicated in Fig. 4.3. Distances are in Å and angles in degrees. . . . 83

4.2 Structural parameters of the ECLS, the interchain bridging, exchange-reacted and diffuse-reacted for S-deposited to the InP(110) surface. These parameters are indicated in Figs. 4.7 and 4.14. Distances are in Å and angles in degrees. 85

5.1 Structural parameters (in Å) of Model II (see Fig. 5.2) for the H_2S-adsorption on InP(110), GaAs(110) and GaP(110) surfaces. 109

7.1 Calculated values of the structural parameters indicated in Fig.2. Distances are in Å and angles in degrees. Experimental results for the dimer bond length lie in the range 2.20-2.47 Å for the *clean* Si(001) surface and 2.41-2.44 Å for the *clean* Ge(001) surface (see e.g. [11]). Theoretical results for the dimer bond length lie in the range 2.25-2.30 Å for the *clean* Si(001) surface and 2.36-2.46 Å for the *clean* Ge(001) surface (see [11]). All results are obtained with 8 Ry energy cut-off, except indicated otherwise. 153

Chapter 1

Introduction

1.1 Introduction

The determination of surface atomic structure and its relation to electronic properties plays a significant role in modern surface science and technology. Today's many powerful experimental techniques and theoretical models are mainly focused on semiconductor surfaces [1] and thousands of articles have been published over the last two decades about electronic properties, geometric structures, vibrational, and optical properties.

A range of experimental methods have been successfully employed in the study of semiconductor surfaces and a number of these techniques measure quantities that are directly calculable using theoretical methods. Experimentally some of these parameters can only be determined indirectly, due to a number of physical effects. Furthermore, other parameters are currently inaccessible to experimentalists.

Theoretical calculations have flourished in modern day science even though theoretically we cannot understand some physical cases which are more complicated, such as burning and melting. In theory, a model of the system is constructed, usually in the form of a set of mathematical equations. Then the model is validated by its ability to describe the system behaviour in a few selected cases such as energy bands.

Recent theoretical approaches to semiconductor studies are nearly all based on the developing of the energy band theory which was firstly done by Bloch who applied quantum mechanics to calculate the electronic band structure in a perfect crystal. This theory is based on the one-electron approximation. A periodic potential contains the interactions of one electron with all other electrons and nuclei in the solid. However, this was not ideal since it ignores the electron-electron interactions. The most reliable approach for that is based on Density Functional Theory (DFT) of Kohn-Sham-Hohenberg [2, 3] using self-consistent field theory, also known as *ab initio* calculation. This calculation starts from first principles. More detail explanation will be discussed in the following chapter.

In this chapter some of the basic concepts of semiconductor surfaces are discussed, along with some of the reasons why making predictions from theoretical calculations on such surfaces is of interest. For example, we consider passivation of elemental compound group-IV (Si or Ge) semiconductors and of binary compound III-V semiconductors. The best-known semiconductor is actually Si. It crystallises in the diamond structure with each atom bonded with four nearest neighbour atoms (i.e., tetrahedrally bonded) and is purely covalent in character. Binary compound semiconductors have properties very similar to the elemental semiconductors. The bonding becomes partly ionic due to transfer of electronic charge from the group-III atom to the group-V atom. This ionicity causes significant changes in the semiconductor properties.

The picture is further complicated by the presence of surfaces. Cleaving or growing a crystal with atoms remaining in their bulk positions would result in all the atoms at the surface having an incomplete bonding configuration. This undesirable situation can be improved by forming a new bonding configuration by one of three mechanisms; (i) reconstruction, (ii) capturing impurity atoms from environment (i.e. growth chamber) and (iii) deliberately adding adatom species. Therefore, the nature of clean and covered semiconductors surfaces has been of particular interest. With increased device miniaturisation, these surface effects may no longer be safely ignored.

1.2 Bulk Semiconductors

1.2.1 Diamond/Zinc-Blende Crystal Structures

The distribution of atomic equilibrium positions can define the structure of a solid. In ideal crystalline systems, atomic equilibrium positions form a geometric pattern that is exactly repeated throughout the solid without change in composition, dimension and orientation. For these reasons, crystalline solids have been extensively studied. For example, the Schrödinger equation needs to be solved only for points within a single pattern rather than for points throughout the whole crystal. It also makes interpretation of many experiments straight-forward due to the perfect periodicity. Crystalline periodicity may be described in terms of three dimensional geometric figures called unit cells. The crystal may be thought of as a collection of unit cells, all identical and all containing the same distribution of atoms.

For instance, the diamond structure may be generated from the face centred cubic (fcc) structure by adding a second face-centred cubic structure displaced from the first one-quarter of the way along a cube diagonal [111]. In this structure, each atom has four nearest neighbours (see Fig. 1.1). Thus, each atom gives up four electrons to form covalent bonds with its neighbouring atoms. The primitive unit cell of diamond structure consists of two atoms, which are at (0, 0, 0) and $a(\frac{1}{4}, \frac{1}{4}, \frac{1}{4})$, where a is the cubic lattice constant. The zinc-blende structure is closely related to the diamond structure, but now the two inter-penetrating fcc structures contain different atoms (see Fig. 1.1(a)). In the diamond and zinc-blende structures, the primitive unit cell can be chosen as that of a face-centred cube of side a with translation vectors (see Fig. 1.1(b)).

$$
\begin{aligned}
\mathbf{a_1} &= \frac{a}{2}(0,1,1) \\
\mathbf{a_2} &= \frac{a}{2}(1,0,1) \\
\mathbf{a_3} &= \frac{a}{2}(1,1,0).
\end{aligned}
\tag{1.1}
$$

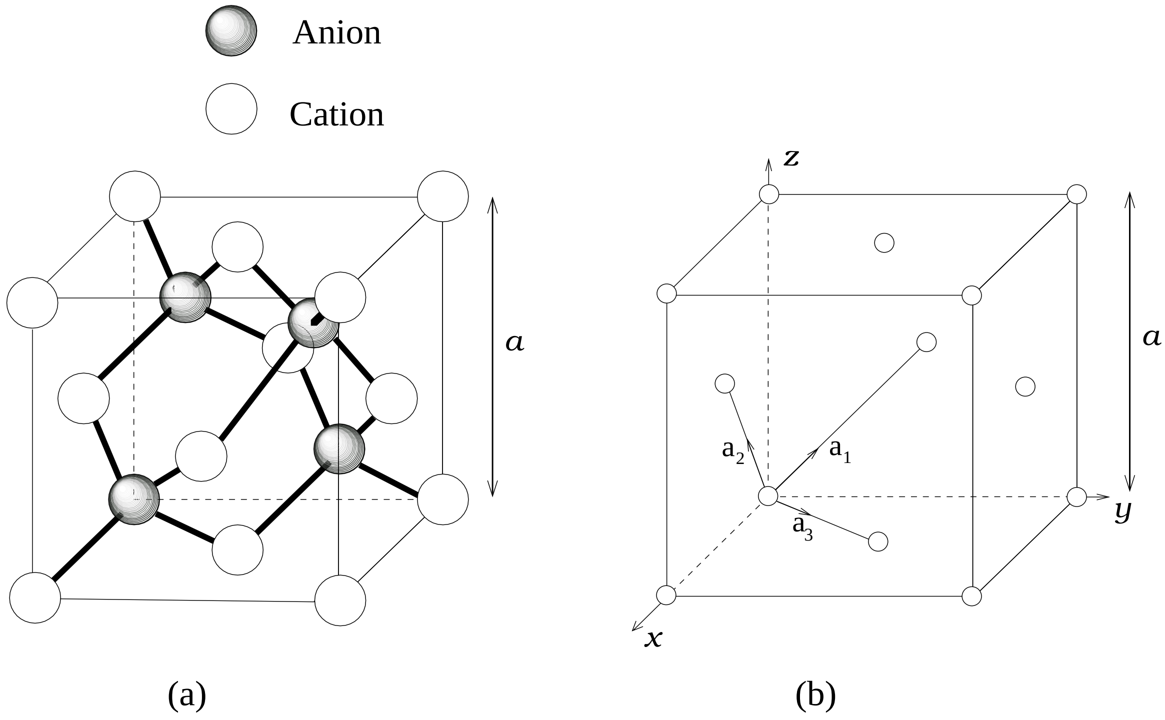

Figure 1.1: (a) The zinc-blende structure. (b) The face-centred cubic structure. The zinc-blende structure becomes the diamond structure when cations and anions are identical.

1.2.2 Bulk electronic states

The allowed electronic energy states of perfect three-dimensional (3D) crystals lie in the so-called energy-bands. More specifically, the requirement is that the underlying crystalline potential $V(\mathbf{r})$ is translationally invariant in all directions and the electrons that lie in this idealised perfectly periodic potential are referred to as *Bloch* electrons. In this case the eigenvalues of the Schrödinger equation are dependent only on the wavevector, $\mathbf{k}$, which lies in the first Brillouin zone and we would expect the eigenvalues E_k to vary continuously with wavevector. There is a solution to the Schrödinger equation for every primitive cell in the crystal, resulting in the attachment of a band index n to a particular energy solution. Bloch functions which are the solutions of the Schrödinger equation for a periodic potential must be of a special form:

$$\psi(\mathbf{r}) = u_k(\mathbf{r})\exp(i\mathbf{k}\cdot\mathbf{r}) \tag{1.2}$$

where $u_k(\mathbf{r})$ has the periodicity of the crystal lattice with $u_k(\mathbf{r})=u_k(\mathbf{r}+\mathbf{T})$ ($\mathbf{T}$ is a translational vector). The result in Eq. 1.2 expresses the Bloch theorem: the eigenfunction of the wave equation for a periodic potential are the product of a plane wave $\exp(\imath\mathbf{k}\cdot\mathbf{r})$ times a function $u_k(\mathbf{r})$ with the periodicity of the crystal lattice. It may be substituted into the (spin-independent) Schrödinger equation

$$\left(-\frac{\hbar^2}{2m}\nabla^2 + V(\mathbf{r})\right)\psi(\mathbf{r}) = E_{\mathbf{k}}(\mathbf{k})\psi(\mathbf{r}) \tag{1.3}$$

We obtain energy bands (E_k) for the wavevector $\mathbf{k}$. Once again, for the idealised concept of a crystal with perfect translational symmetry, a solution exists for every primitive cell in the structure. For theories based on Bloch states, the number of solutions (energy bands) at a particular wavevector corresponds to the number of Bloch states used in the wavefunction basis. From a fundamental point of view, the energy bands are the result of interactions between electrons in the energy states with their corresponding core ions. A total energy saving can be made via this interaction, resulting in the atoms bonding into a material. Physical and chemical properties are almost totally determined by the valence electrons. This leads to the very useful approximation of not needing to treat the core electrons with the same detail as the valence electrons.

The potential in Eq. 1.3 is very important to determine the properties of the band structure. If there is no underlying potential whenever an electron crosses a Bragg plane it can smoothly transfer from one energy-band solution to the next higher energy-band solution in energy. The action of the potential is to lift the degeneracies of these solutions at Brillouin zone edges. In the second chapter, we will show the Brillouin zone for the fcc lattice with the corresponding symmetry points. The electronic valence band structures of GaAs and Si calculated by pseudopotential method are shown in Fig. 1.2.

1.3 Semiconductors Surface

On a surface the atoms and electronic charge rearrange themselves considerably from the bulk material. Then, a surface, like a defect within the bulk crystal, breaks the fundamental 3D periodicity. The problem is now more complicated than

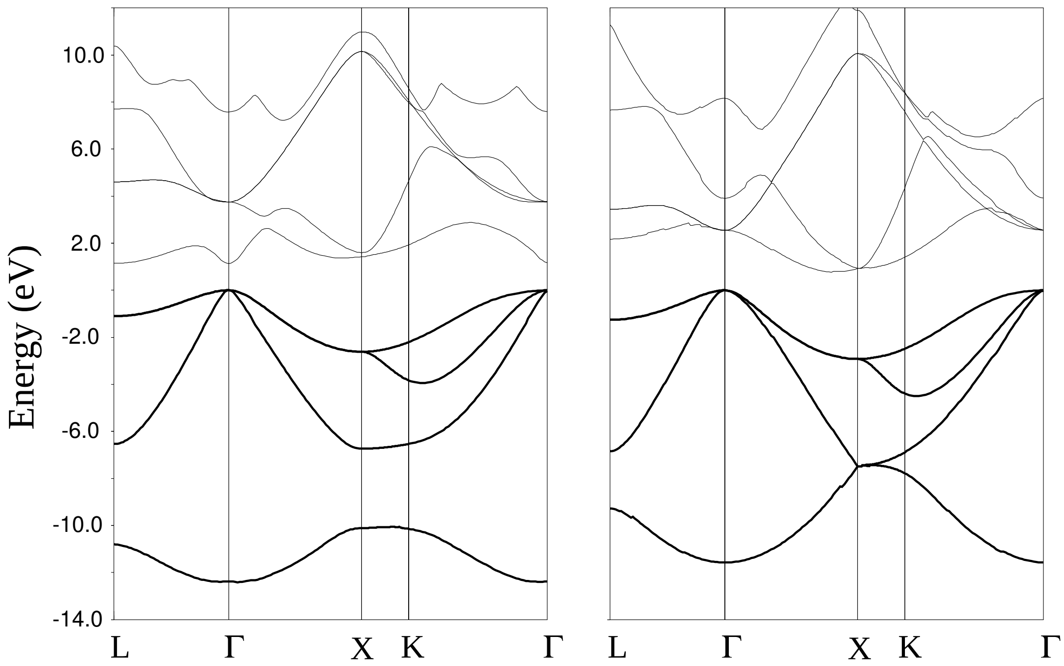

Figure 1.2: Electronic bulk band structure of (a) GaAs and (b) Si, calculated by pseudopotential technique. Occupied and unoccupied surface states are shown by thick and thin curves, respectively. The symmetry points in the Brillouin zone are explained in chapter 2.

the perfect periodic system because the equilibrium positions of the atoms inside the crystal are different from those on a surface. The boundary condition on the equations and the environment of the atoms on the surfaces is very different from that in the bulk. However, the laws of the interactions on surfaces are the same as those appropriate to the bulk.

Before we start talking about surface geometries, let us explain the Pauli exclusion principle: no more than one electron can be in a given state of a system. Two electrons may have the same spatial wave function but only if one has its spin up and the other its spin down, i.e., two spin-paired electrons. When a bond is severed, there will be unbonded orbitals outward from a surface. These orbitals are called dangling orbitals or dangling bonds which contain less than two spin-paired electrons as shown schematically in Fig. 1.3. They are unstable, allowing the surface to relax and it may *reconstruct*. In other words, on some surfaces the atoms rearrange and form a structure energetically more favourable than the truncated bulk. In surface physics, such a rearrangement is called reconstruction. Surface relaxation can still occur within the 1×1 (or primitive) periodicity caused by a reduction in the surface free energy by moving atoms away from its bulk configuration. The unit cells sometimes become larger than the primitive unit cell, such as $n \times m$ rather than 1×1. Therefore the surface is said to be $n \times m$ reconstructed. In the forthcoming chapters we will give some examples for reconstructed surface. The other consideration in the surface science is the direction of the surface. If the clean surface we create is one of the (hkl) planes, then the surface normal is in the [*hkl*] direction, e.g. Si(111)(7×7) [4] or Si(001)(2×1) [5]. The surfaces dealt with in later chapters are (110) and (001). More detailed explanation about relaxation and reconstruction of surfaces can be found in the review articles of by Duke [6] and Srivastava [7].

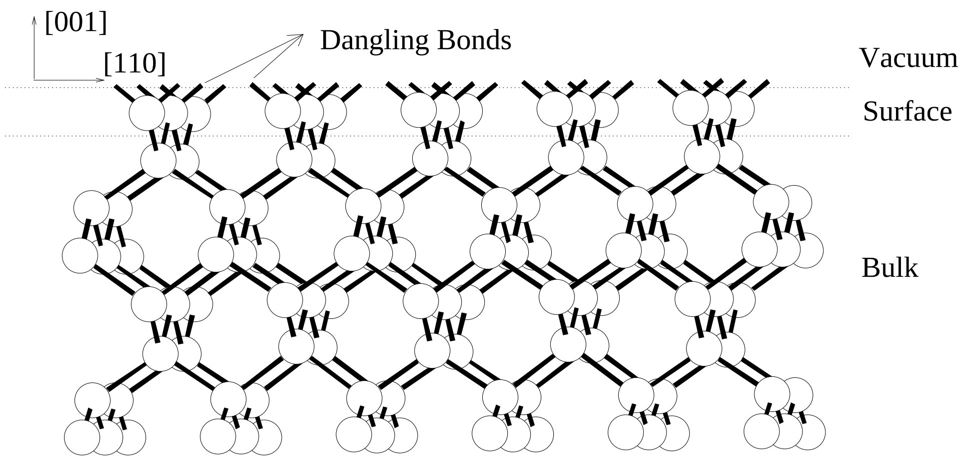

Figure 1.3: Si atomic structure of the (001) face. Schematic representation of bulk region, surface region, vacuum region and dangling bonds.

1.3.1 Modelling surfaces within a repeated slab scheme

Our approach to study surfaces is to retain the periodicity along surface normal by introducing the concept of super cell [8]. It means that a surface can be simulated within the super cell framework by choosing a unit cell to consist of a sandwich of vacuum and material and vacuum. The super cell technique allows an artificial periodicity to be imposed perpendicular to the surface so that plane waves and three-dimensional periodic boundary conditions may be used. If periodic boundary

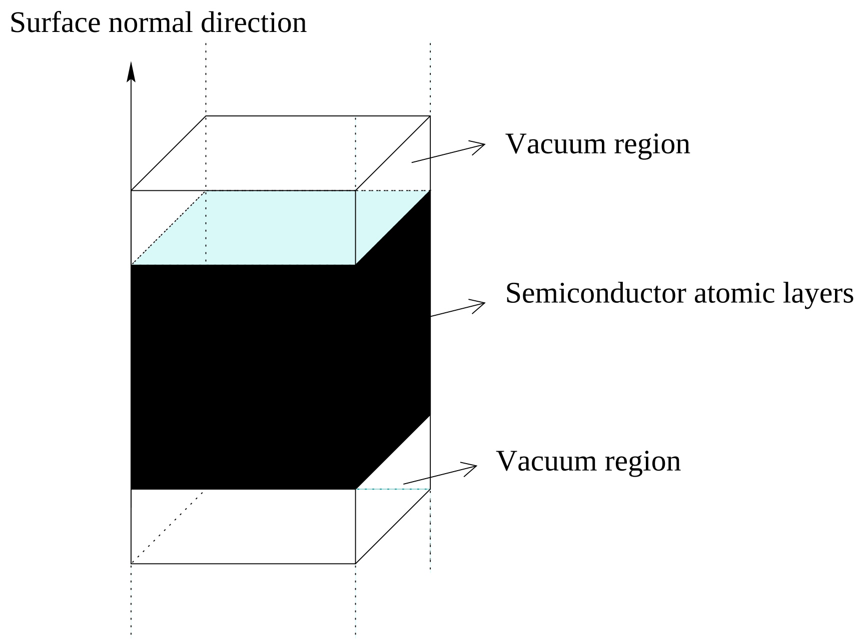

Figure 1.4: A model surface super cell.

conditions are applied to this cell then clearly the effect will be to describe a system comprising an infinite stack of semiconductor slabs, each of finite thickness and separated by finite regions of vacuum. Thus, if the slabs are thick enough, the surfaces on either side of the same slab will not interact with each other. Similarly, if the vacuum layers are wide enough, the facing surfaces of neighbouring slabs will also not interact with each other. In these circumstances it would be true to say that each surface acts in the manner of an isolated surface. Unfortunately calculations with very large super cells are very computationally intensive. A schematic super cell is shown in Fig. 1.4.

1.3.2 Surface States

Surface electronic states refer to states localised near the surface. Moreover, the dangling bonds which we referred to earlier, are partially filled bonds which give rise to additional electron states. They will form two-dimensional bands because of the translational symmetry along the surface. If these bands overlap with the continuum of either empty or occupied bulk states they are extended with interaction with those bulk states. They can be called surface resonance states. However, these bands may lie at least in part in the forbidden energy gaps. In this case they may be called surface states.

1.3.3 Energy Gap

When the electron crosses a Bragg plane, additional energy must be supplied in order for the electron to transfer from one energy band to another. These energy gaps allow the construction of electronic devices from semiconductor structures. In the case of semiconductors these energy gaps exist throughout the crystal for particular energy windows. The most important of the gaps corresponds to the one in which the Fermi-energy lies; semiconductors have no Fermi-surface. For energies below the Fermi-energy all electronic states are occupied and correspondingly all states above Fermi-energy are unoccupied. Since full bands cannot carry current, the semiconductor will act as an insulator unless energy can be supplied to force electrons into higher unoccupied (conduction) bands. Once an electron has been transferred into an upper band, there is an empty state lying in the valence band. Rather than talk about the behaviour of all the electrons left in the valence band in the presence of the empty state, it is easier to talk about the behaviour of the empty state, which is known as a 'hole'. A critical difference among the semiconductors lies in the fundamental energy gap of the semiconductor which corresponds to the energy of the bottom of the conduction band at k (E_c) minus the energy of the top of the valence band at k (E_v). It allows sensitive control over the electronic properties of the material. If their edges occur at the same k-values, the material is called a direct band gap such as GaAs as seen Fig. 1.2(a). If their edges occur at the difference k-values, it is called an indirect band gap material such as Si as seen Fig. 1.2(b). For Si, the valence edge occurs at Γ but the conduction edge occurs at near X.

1.3.4 Passivation of Surface States

In semiconductor technology, communication between the various devices is clearly very important. As a result, surface formation is very important as any contact is a surface or interface. Surface states (mentioned in the previous section) can potentially cause a problem due to the availability of electronic states in the previously forbidden region. Unoccupied surface states in the gap region can capture electrons crossing the surface. However, it is possible to control the energetic location of surface states by adsorption of certain atoms or molecules.

Presence of surface dangling bonds is highly undesirable. The existence of undesirable dangling bonds at semiconductor surfaces leads to the phenomenon of Fermi level pinning. Fig. 1.5(a) schematically shows the valence band edge, Fermi level and conduction band edge for intrinsic bulk materials. Figs. 1.5(b) and (c) show that surface (or interface) states in the gap near the valence or conduction band edge lead to the band bending effect and the Fermi level pinning. A metal-semiconductor contact with rectifying properties is called a Schotty barrier, and with a linear I-V curve it is characterised by an Ohmic behaviour [9]. The band bending can occur in two ways: if the contact is made by an n-type semiconductor, the band bending effects look like as shown in Fig. 1.5(b) (i.e. Schottky barrier). If the contact is made by a p-type semiconductor, the band bending effects look like in Fig. 1.5(c) (i.e. Ohmic contact). The Fermi level can be pinned within a fairly narrow energy range with a high density of states due to the dangling bonds.

Most reconstructions reduce the effect of eliminating these undesirable bonds. Another elimination way of these bonds is the interaction between a semiconductor and an adsorbate. The Fermi level pinning and band bending can be seen very clearly from results presented in later chapters. For example, in Chapter 6 we will be showing the clean and adsorbate Si(001) surfaces (c.f. Figs. 6.3 and 6.6). For the clean Si(001) surface with an asymmetric dimer model, the higher-lying dimer component (D_u) is fully occupied with the associated electronic state close to the bulk valence band maximum, and the lower-lying dimer component (D_d) is empty corresponding to the energy state in the upper half of the bulk silicon band gap. These are due to the two dangling-bond orbitals per dimer. The Fermi level lies between these two bands with very high density of states. It can be considered that the conduction band edge is the unoccupied state (D_d) and the valence band edge is the occupied state (D_u). These two mid-gap states present the band bending situation. When the dangling bands are passivated by sulphur atoms, these two bands push up and down in the bulk continuum. The Fermi level pinning and band bending can therefore be removed. When this happens the surface is said to be completely passivated. Basically, the passivation means removing the Fermi level pinning and band bending. It is thus desirable to explore the passivating properties of various elements when adsorbed on semiconducting surfaces. In general such deposition results in a change in the morphology of the surfaces. The reconstruction may change and the substrate relaxation will almost certainly change.

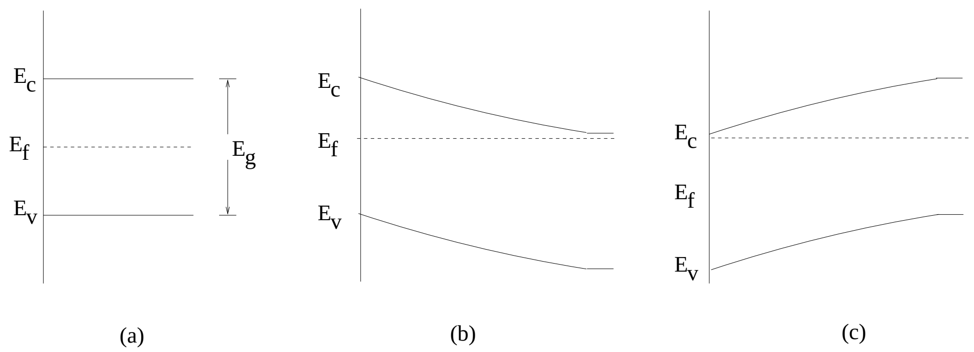

Figure 1.5: Electronic energy levels for (a) an undoped semiconductor sample, (b) band bending and Fermi level pinning at equilibrium (i.e. Schottky barrier), and (c) band bending and Fermi level pinning at equilibrium (i.e. Ohmic contact).

As the device dimensions are getting smaller and smaller, it is becoming more and more important to control the adsorption of a monolayer and even sub-monolayer coverage of such material and to understand the equilibrium atomic geometry and the resulting electronic band structure. To date, many experimental as well as theoretical studies have been carried out for the atomic geometry, electronic structure and chemical bondings of ordered overlayers of group-I, -III, -IV, -V, -VI and VII on semiconductors [7].

Recently, there has been growing interest in the adsorption of group-VI elements, such as S and Se, because of their passivating properties, especially for polar III-V(001) [10] and III-V(111) [11] surfaces. The sulphur treatment reduces surface recombination velocities, enhances the photoluminescence [10] and the metal-insulator-semiconductor C-V characteristics [12]. Using *ab initio* calculations for ordered (1×1) geometry, Ohno *et al.* explained the sulphur passivation of GaAs(001) [13] and GaAs(111) [14] surfaces in terms of the formation of Ga-S bonds, without introducing any disorder or defects near the surface. Elemental S

E_{cut} (Ry)	E_g (eV) [Using Exp. Lat. Par.]	E_g (eV) [Using The. Lat. Par.]
8	0.768	0.777
10	0.637	0.648
12	0.497	0.513
14	0.501	0.509
16	0.478	0.486
18	0.481	0.469
20	0.470	0.461

Table 1.1: Calculated energy gaps for Si using different kinetic energy cut-offs. Experimental lattice parameters for Si is taken as 5.43 Å [28]. The calculated lattice parameter for Si is taken as 5.42 Å. The experimental energy gap at 0 K is 1.17 eV.

deposition will help to obtain a better understanding of the binding structure and electronic properties of the growth of chalcogenide protective films such as GaS and InS.

Clean and adsorbate covered Si(001) and Ge(001) surfaces have also been studied very intensively by experiment and theory [15, 16, 17, 18, 19, 20]. The low temperature clean Si(001) surface is understood to reconstruct to a c(4×2) (i.e., Si dimers are centred in the (4×2) unit cell) phase consisting of alternately asymmetric dimers [21], while at room temperature the reconstruction appears (2×1). Structural studies of clean Si(001) using low energy electron diffraction (LEED) [22], reflection high energy electron diffraction [23], x-rays [24], and He atoms [25] indicate an asymmetric dimer geometry for the top surface layer, corresbonding to a (2×1) reconstruction, while surface electronic bands have been mapped by photoemission [26]. Recent well-converged *ab initio* pseudopotential total energy calculations also favour the asymmetric dimer configuration [5, 27].

Other interesting studies have carried out using H_2S molecules. The low temperature adsorption of H_2S on III-V(110) surfaces is believed to be in a dissociative form, with the presence of SH and H species [29, 30, 31, 32]. H_2S gases on Si(001) [33] and Ge(001) [34] has been investigated using Auger electron spectroscopy (AES) and photoelectron spectroscopy (UPS).

1.4 Sensitivity of results

In Tab. 1.1 we have compiled the calculated band gaps for the Si bulk using both the experimental and our theoretical lattice parameter for different kinetic energy cut-offs. Table shows that the band gaps using both experimental and theoretical lattice parameters for 12 Ry are reasonably well converged. For this case the two calculated band gaps are almost the same due to the experimental lattice parameter and theoretical lattice parameter being very close to one another. However, the calculated band gap for both lattice parameters is ∼50% smaller than the experimental band gap value for Si.

For other semiconductors, well converged band gaps using both the experimental and theoretical lattice parameters for a 12 Ry cut-off are listed in Tab. 1.2. When one uses the experimental lattice parameters, the band gaps are repeatedly smaller than the experimental band gaps, such as ∼10% smaller for InP and ∼100% for Ge as seen in Tab. 1.2. This discrepancy for the band gap results mainly from the DFT theory (and also partly due to the choice of pseudopotentials) which is a ground state theory and as such does not describe unoccupied states very well, which is why even using the experimental lattice parameter leads to too smal a band gap. Various methods exist to make corrections to the DFT results, such as the GW theory [35].

However, in our calculations the lattice parameters are smaller than the experimental lattice parameters. Generally, the theoretical lattice constants are smaller: such as ∼3.5% for InP and ∼0.2% for Si as seen in Tab. 1.2. This is mainly due to the LDA (and also partly due to the choice of pseudopotentials). This underestimation for the lattice parameters generally pushes up the energy gaps of semiconductors. This can accidently remedy the band gap problem. As can be seen from Tab. 1.2, the band gaps at theoretical lattice constants are much more respectable.

In the forthcoming chapters, one will see the relative positions of the surface states. For example, using the theoretical lattice constant, our calculation on the clean InP(110) surface shows no occupied gap states in the fundamental gap (c.f. Fig. 4.4). This is consistent with the experimental results. Another example can be taken the InP-H_2S interface in Chapter 5. We will present both the available

	Si	Ge	InP	GaAs	GaP
a (Å) [Exp.][36]	5.43	5.66	5.87	5.65	5.45
E_g (eV) [Exp.][28]	1.17 (i)	0.74 (i)	1.42 (d)	1.52 (d)	2.35 (i)
E_g (eV) [Using Exp. Lat. Par.]	0.51 (i)	0.00 (d)	1.31 (d)	1.14 (d)	1.67 (i)
a (Å) [DFT/LDA]	5.42	5.53	5.65	5.50	5.35
E_g (eV) [Using The. Lat. Par.]	0.50 (i)	0.42 (i)	1.70 (i)	1.30 (i)	1.60 (i)

Table 1.2: Experimental [36] and theoretical lattice constants (a) and energy gaps (E_g) [28] for homopolar and heteropolar type semiconductors versus theoretical calculated values. The i and d refer to inderect and direct gaps. Theoretical calculated values have been made using 12 Ry kinetic energy cut-off.

experimental data and our calculated surface states. As can be seen in Fig. 5.3, there are no surface states in the fundamental gap region as concluded from the experimental measurements and our theoretical calculations.

1.5 Summary of the structure of this thesis

This thesis starts with the theoretical approaches and a brief explanation of computational procedures. In Chapter 3, some experimental techniques are discussed such as Low Energy Electron Diffraction (LEED), Reflection High Energy Electron Diffraction (RHEED), Scanning Tunneling Microscope (STM), X-ray Standing Wave (XSW), Photoelectron Spectroscopy (PS) and Auger Electron Spectroscopy (AES). In Chapter 4, a detailed investigation of S-covered InP(110) surface is presented. The results are compared with the available experimental and theoretical results. In Chapter 5, the H_2S passivation on the III-V(110) surfaces are presented using the dissociative adsorption geometry. The calculated results are again compared with the available results. In Chapter 6, we investigate the adsorption of elemental S atom on Si(001) and Ge(001) using the proposed geometries. An analysis of surface free energy suggests that, in the allowed range of S chemical potential, the monosulfide structure is more stable than the other geometries. In Chapter 7, the H_2S passivation on Si(001) and Ge(001) surfaces is presented using partially dissociative and fully dissociative geometries. The fully dissociative structure is more energetically favourable than the partially dissociated one. Finally, Chapter 8 contains some concluding remarks on our results and prospects for future research.

Bibliography

[1] C. B. Duke, *Surface Science: The first thirty years*, Amsterdam; North-Holland, reprinted from Surf. Sci. **299/300**, 1994.

[2] P. Hohenberg and W. Kohn, Phys. Rev. B **136**, 864 (1964).

[3] W. Kohn and L. J. Sham, Phys. Rev. A **140**, 1133 (1965).

[4] G. Binning, H. Rohrer, Ch. Gerber and Phys. Rev. Lett. **50**, 120 (1983).

[5] P. Krüger and J. Pollman, Phys. Rev. Lett. **74**, 1155 (1995).

[6] C. B. Duke, Chem. Rev. **96**, 1237 (1996).

[7] G. P. Srivastava, Rep. Prog. Phys. **60**, 561 (1997).

[8] M. Schlüter, M. J. R. Chelikowsky, S. G. Louie, and M. L. Cohen, Phys. Rev. B **12**, 4200 (1975).

[9] *Physics at Surfaces*, A. Zangwill, Cambridge University Press (1988).

[10] C. J. Sandroff, R. N. Nottenburg, J. C. Bischoff and R. Bhat, Appl. Phys. Lett. **51**, 33 (1987).

[11] H. Oigawa, J. Fan, Y. Nannichi, K. Ando, K. Saiki and A. Koma, Jpn. J. Appl. Phys. **28**, L340 (1989).

[12] R. Iye and D. L. Lile, Appl. Phys. Lett. **59**, 437 (1991).

[13] T. Ohno and K. Shiraishi, Phys. Rev. B **42**, 11194 (1990).

[14] T. Ohno, Phys. Rev. B **44**, 6306 (1991).

[15] E. Kaxiras, Phys. Rev. B **43**, 6824 (1991).

[16] P. Krüger and J. Pollman, Phys. Rev. B **47**, 1898 (1993).

[17] P. Moriarty, L. Koenders, and G. Hughes, Phys. Rev. B **47**, 15950 (1993).

[18] A. Papageorgopoulos, A. Corner. M. Kamaratos, and C. A. Papageorgopoulos, Phys. Rev. B **55**, 4435 (1997).

[19] M. Göthelid, G. LeLay, C. Wigren, M. Björkqvist, M. Rad, U. O. Karlsson, Appl. Sur. Sci. **115**, 87 (1997).

[20] G. W. Anderson, M. C. Hanf, P. R. Norton, Z. H. Lu, and M. J. Graham, Appl. Phys. Lett. **66**, 1123 (1994).

[21] D. Badt, H. Wengelnik, and H. Neddermeyer, J. Vac. Sci. Technol. B **12**, 2015 (1994).

[22] B. W. Holland, C. B. Duke, and A. Paton, Surf. Sci. **140**, L269 (1984).

[23] G. Jayaram, P. Xu, and L. D. Marks, Phys. Rev. Lett. **71**, 3489 (1993).

[24] E. Fontes, J. R. Patel, and F. Comin, Phys. Rev. Lett. **70**, 2790 (1993).

[25] W. R. Lambert, P. L. Trevor, M. J. Cardillo, A. Sahai, and D. R. Haman, Phys. Rev. B **35**, 8055 (1987).

[26] L. S. O. Johanson, R. I. G. Uhrberg, P. Martensson, and G. V. Hansson, Phys. Rev. B **42**, 1305 (1990).

[27] S. J. Jenkins and G. P. Srivastava, Sur. Sci. **352-354**, 411 (1996).

[28] G. Burns, *Solid State Physics*, International Edition, Acedemic Press, 1990.

[29] E. Dudzik, R. Whittle, C. Müller, I. T. McGovern, C. Nowak, A. Märkl, A. Hempelmann, D. R. T. Zahn, A. Cafolla, W. Braun, Surf. Sci. **307**, 223 (1994).

[30] E. Dudzik, C. Müller, I. T. McGovern, D. R. Lloyd, A. Patchett, D. R. T. Zahn, T. Johal, and R. McGrath, Surf. Sci. **344**, 1 (1995).

[31] E. Dudzik, A. Leslie, E. O'Toole, I. T. McGovern, A. Patchett, D. R. T. Zahn, J. Ludecke, D. P. Woodruff and B. C. C. Cowie, J. Phys.: Condens. Matter **8**, 15 (1996).

[32] T. K. Johal, P. Finetti, V. R. Dhanak, A. W. Robinson, A. Patchett, D. R. T. Zahn, and R. McGrath, Appl. Surf. Sci. **104**, 257 (1996).

[33] E. Schröder-Bergen and W. Ranke, Surf. Sci. **236**, 103 (1990).

[34] H. J. Kuhr and W. Ranke, Surf. Sci. **189/190**, 420 (1987).

[35] S. J. Jenkins, *Quasiparticle Band Structure of Semiconductors and their Surfaces*, Ph. D thesis, Exeter University (1995).

[36] *Physics of Group IV and III-V Compounds*, Landolt-Börnstein, New Series, Group III, Vol. 17a (Springer, Berlin 1982).

Chapter 2

Theory

2.1 Introduction

This chapter presents a review of *ab initio* pseudopotential method, which will be used in the studies presented in this thesis. The essentials of the method and its implementation are outlined here, but a more detailed account may be found in the literature [1, 2, 3, 4, 5, 6, 7, 8].

2.2 The fundamental problem

The behaviour of electrons and ions in a crystalline system is described by the many body wavefunction Ψ. This wavefunction satisfies the many-body Schödinger equation

$$\hat{H}\Psi_i(\mathbf{R},\mathbf{r}) = E_i\Psi_i(\mathbf{R},\mathbf{r}), \tag{2.1}$$

where $\hat{H}$ represents the Hamiltonian, and $\Psi_i(\mathbf{R},\mathbf{r})$ the wave function, for the collection of all the ions at $\mathbf{R}$ and electrons at $\mathbf{r}$ in the system. Obviously, the many-body Hamiltonian in Eq. 2.1 cannot be solved without a large number of simplifications. The fact that the atomic nuclei are much heavier than the electrons, $\mathrm{m}_{(n,p^+)} \approx 2000$ m_e, means that the electrons will respond immediately to the movement of the nuclei. The approximation invoked is the Born-Oppenheimer or adiabatic approximation. Ignoring spin-orbit and relativistic effects the Hamiltonian may be written as

$$H = T_{\rm ion} + V_{\rm ion-ion} + T_{\rm el} + V_{\rm el-el} + V_{\rm el-ion} \tag{2.2}$$

where $T_{\rm ion}$ and $V_{\rm ion-ion}$ represent the kinetic and potential energy operators of the ions, $T_{\rm el}$ represents the kinetic energy operator of the electrons, $V_{\rm el-ion}$ represents the electron-ion interaction term and $V_{\rm el-el}$ represents the electron-electron interaction. Using the Born-Oppenheimer approximation the total wavefunction can be written as a product of the ionic and electronic wavefunctions:

$$\Psi(\mathbf{R}, \mathbf{r}) = \chi(\mathbf{R})\eta(\mathbf{R}, \mathbf{r}) \tag{2.3}$$

where $\mathbf{R}$ denotes the positions of all ions ($\mathbf{R}_i$:i=1,...,N) and $\mathbf{r}$ denotes the electron co-ordinates ($\mathbf{r}_i$:i=1,...,M). Here $\eta(\mathbf{R}, \mathbf{r})$ is an ionic wave function depending only on the electronic coordinates $\mathbf{r}$ and ionic positions, and the electronic wave function $\chi(\mathbf{R})$ depends on the ionic configuration $\mathbf{R}$. From the Eq. 2.1 and the Eq. 2.3 one obtains two coupled Schrödinger equations [1, 2]:

$$[\hat{H}_{\rm ion} + E_{\rm el}(\mathbf{R})]\chi(\mathbf{R}) = E\chi(\mathbf{R}) \tag{2.4}$$

for the ions, and

$$[\hat{H}_{\rm el}]\eta(\mathbf{R}, \mathbf{r}) = E_{\rm el}\eta(\mathbf{R}, \mathbf{r}) \tag{2.5}$$

for the electrons. The Hamiltonian for the electrons may be written as

$$\hat{H}_{\rm el} = -\frac{\hbar^2}{2m}\sum_i \nabla^2_{\mathbf{r}_i} + \sum_i V_{\rm ext}(\mathbf{r}_i) + \sum_i V_{e-e}(\mathbf{r}_i). \tag{2.6}$$

The potential $V_{\rm ext}$ consists of the external potential imposed on the electrons by nuclear configuration, $\mathbf{R}_i$, and V_{e-e} is the electron-electron interaction. The interaction between ion and electrons, $V_{\rm ext}$, may be described by one of two methods, i.e., an all-electron method or a pseudo-potential method.

2.3 Electron-Electron Interaction

Eq. 2.5 still is diffucult to solve since it has a very complicated many-particle eigenvalue problem. Two approaches, wave-function approach and density functional approach, are in common use today for the solution of the many body Schrödinger equation. They are variational techniques which reduce the many body Schrödinger equations to single particle equations.

2.3.1 Wave-function Approaches

2.3.1.1 Hartree Theory

It is possible to write the Hamiltonian of a system of interacting electrons as a sum of single-particle hamiltonians. This implies that the many-electron wave function can be written as a product of single-particle wave functions, as shown below:

$$\eta(\mathbf{r_1}, ..., \mathbf{r_N}) = \prod_{i=1}^{N} \phi_i(\mathbf{r}_i) \tag{2.7}$$

where the $\{ \mathbf{r}_i \}$ denote the electron coordinates, and the orbitals $\phi_i(\mathbf{r_i})$ are ortonormal. If the single-particle wave function ϕ minimizes $< H >$, then infinitesimal variation of ϕ causes no change in $< H >$ ($\phi \rightarrow \phi + \delta\ \phi$). Taking the expactation value of $\hat{H}$ with the wavefunction ϕ_i, and imposing the normalization of the functions ϕ_i by introduction of the Lagrange multipliers $\mathrm{E}_i^{\mathrm{H}}$ we can consider the functional

$$< \phi_1(\mathbf{r}_1), ..., \phi_N(\mathbf{r}_N) \mid \hat{H} \mid \phi_N(\mathbf{r}_N), ..., \phi_1(\mathbf{r}_1) > - \sum_i E_i^{\mathrm{H}} < \phi_i \mid \phi_i > \tag{2.8}$$

Applying the variational principle to the function ϕ_i, one obtains the corresponding Hartree single-particle equations

$$[-\frac{\hbar^2}{2m} \sum_i \nabla_{\mathbf{r}_i}^2 + V_{\mathrm{ext}}(\mathbf{r_i}) + V_{\mathrm{H}}(\mathbf{r_i})] \phi_i(\mathbf{r}) = E_i^{\mathrm{H}} \phi_i(\mathbf{r}), \tag{2.9}$$

where

$$V_{\mathrm{H}}(\mathbf{r}) = e^2 \sum_j \int d\mathbf{r}' \frac{\mid \phi_j(\mathbf{r}') \mid^2}{\mid \mathbf{r} - \mathbf{r}' \mid} \tag{2.10}$$

is the Hartree (or Coulomb) potential. The Hartree approximation for the total energy is then

$$E^{\mathrm{H}} = \sum_{i} < \phi_i \mid -\frac{\hbar^2}{2m}\nabla^2_{\mathbf{r}_i} + V_{\mathrm{ext}}(\mathbf{r}_i) \mid \phi_i > + \frac{1}{2}\sum_{i\neq \mathrm{J}} < \phi_i\phi_j \mid \frac{e^2}{\mid r_i - r_j \mid} \mid \phi_j\phi_i > . \tag{2.11}$$

Eq. 2.9 is single particle equations which can be solved self-consistently. However, the Hartree approximation does not satisfy the antisymmetry under particle interchange, imposed by the Pauli exclusion principle. This problem is improved in the Hartree-Fock approximation.

2.3.1.2 Hartree-Fock Theory

The Hartree-Fock energy E^{HF} differs from the Hartree energy by an extra additional electron exchange energy term (i.e., the electron wave function has the proper symmetry under the interchange of two electrons and this leads to exchange terms in the energy).

$$E^{\mathrm{HF}} = E^{\mathrm{H}} + E^{\mathrm{ex}} \tag{2.12}$$

It means that the corresponding Hartree-Fock equations for the single particle wave functions differ from the Hartree equations by an exchange potential.

$$[-\frac{\hbar^2}{2m}\sum_{i}\nabla^2_{\mathbf{r}_i} + V_{\mathrm{ext}}(\mathbf{r_i}) + V_{\mathrm{H}}(\mathbf{r_i}) + V_{\mathrm{ex}}(\mathbf{r_i})]\phi_i(\mathbf{r}) = E_i^{\mathrm{HF}}\phi_i(\mathbf{r}) \tag{2.13}$$

where,

$$V_{\mathrm{ex}}\phi_i(\mathbf{r}) = -e^2\sum_{j}\phi_j(\mathbf{r})\int\frac{\phi_j^*(\mathbf{r}')\phi_i(\mathbf{r}')}{\mid \mathbf{r} - \mathbf{r}' \mid}d\mathbf{r}', \tag{2.14}$$

gives the effect of a non-local exchange potential. The Hartree-Fock calculations have been carried out for the ground state energy of atoms, but for solids these calculations are very complicated. The electronic states and total ground state energy of insulators and semiconductors are found to be unsatisfactory. This is because this scheme neglects screening of the exchange interaction, generally known as correlation effect [2].

2.3.2 Density functional Approaches

2.3.2.1 Thomas-Fermi Theory

Thomas-Fermi theory marks the change in approach from Hartree and Hartree-Fock theory, as it was the first method to propose using the electronic charge density as its fundamental variable instead of the wavefunction. It is thus the earliest form of density functional theory. Although the charge density is that of a non-uniform electron gas, the number of electrons in a given element, $d\mathbf{r}$, can be expressed as $n(\mathbf{r})d\mathbf{r}$, where $n(\mathbf{r})$ is the charge density for a uniform electron gas at that point. It is then possible to express the energy as a function of $n(\mathbf{r})$. This approach is extremely simple, and is qualitatively correct for atoms. However it does not give a good binding energy for molecules, and the proof is not rigorous. To overcome these problems it is necessary to move on to the work of Hohenberg, Kohn and Sham [9, 10].

2.3.2.2 Density Functional Theory

In this approach the ground state electron density of a system is considered to be its fundamental variable (rather than the much more complicated many-body electron wavefunction), i.e., that for a given non-degenerate non-polarised ground state wavefunction, there is a unique electron density. All other ground state properties of the system are then expressible in principle as functionals of the ground state electron density instead of the one-electron wavefunctions as in the Hartree-Fock theory. The formulation by Hohenberg and Kohn of density functional theory (DFT) showed that the true ground state energy, E, of the electronic system may be written

$$E_{\mathrm{el}}[V_{\mathrm{ext}}, n(\mathbf{r})] = F[n(\mathbf{r})] + \int V_{\mathrm{ext}} n(\mathbf{r}) d^3r, \tag{2.15}$$

where $F[n(\mathbf{r})]$ is a universal functional and $V_{\mathrm{ext}}(\mathbf{r})$ is the external potential experienced by electrons. It was also shown that the density which minimises E in Eq. 2.15 is the true ground state density. However, it has an unknown functional defined as

$$F[n(\mathbf{r})] = T_o[n(\mathbf{r})] + E_{\mathrm{H}}[n(\mathbf{r})] + E_{\mathrm{xc}}[n(\mathbf{r})], \tag{2.16}$$

where the first two quantities on the right hand side represent the non-interacting kinetic energy of the electrons and the electron-electron interaction in the Hartree approximation with density $n(\mathbf{r})$. The third term, $E_{\mathrm{xc}}[n(\mathbf{r})]$, is considered as a universal functional of $n(\mathbf{r})$ to represent all corrections to the independent particle picture, i.e, to the kinetic energy and the non-classical many-body effects of exchange and correlation (xc), but remains unknown. From Eq. 2.15 and 2.16, the ground state energy of a many-electron system in a given potential $V_{\mathrm{ext}}(\mathbf{r})$ can be expressed

$$E_{\mathrm{el}}[V_{\mathrm{ext}}, \rho(\mathbf{r})] = T_o[n(\mathbf{r})] + E_{\mathrm{H}}[\rho(\mathbf{r})] + \int V_{\mathrm{ext}}\rho(\mathbf{r})d^3r + E_{\mathrm{xc}}[\rho(\mathbf{r})], \tag{2.17}$$

where $\rho(\mathbf{r})$ is the ground state charge density which should minimise $E_{\mathrm{el}}[V_{\mathrm{ext}}, \rho(\mathbf{r})]$. The minimal property of the functional $E_{\mathrm{el}}[V_{\mathrm{ext}}, \rho]$ has to be subjected to be condition that the number of electrons is kept constant

$$\int n(\mathbf{r})d^3r = N \tag{2.18}$$

Thus we use the method of Lagrange multipliers and require that the functional

$$E_{\mathrm{el}}[V_{\mathrm{ext}}, n] - \mu N \tag{2.19}$$

has a minimum, with μ as the Lagrange parameter. The Kohn-Sham theory [9, 10] requires that for the ground state

$$\frac{\delta\{E_{\mathrm{el}}[V_{\mathrm{ext}}, \rho] - \mu N\}}{\delta\rho(\mathbf{r})} = 0 \tag{2.20}$$

Using Eq. 2.17 it can be evaluated

$$\frac{\delta T_o[\rho]}{\delta\rho(\mathbf{r})} + V_{\mathrm{KS}}[\rho] = \mu \tag{2.21}$$

where

$$V_{\mathrm{KS}}[\rho] = V_{\mathrm{ext}}(\mathbf{r}) + V_{\mathrm{H}}[\rho] + V_{\mathrm{xc}}[\rho] \tag{2.22}$$

is an effective Kohn-Sham potential with

$$V_{\mathrm{H}}[\rho] = e^2 \int \frac{\rho(\mathbf{r}')}{\mid \mathbf{r} - \mathbf{r}' \mid} d\mathbf{r}' \tag{2.23}$$

as the Hartree potential and

$$V_{\mathrm{xc}}[\rho] = \frac{\delta E_{xc}[\rho]}{\delta \rho(\mathbf{r})} \tag{2.24}$$

as the exchange-correlation potential. From Eq. 2.19 one can also write

$$\mu = \frac{\partial E_{\mathrm{el}}}{\partial N} \tag{2.25}$$

where μ is actually the chemical potential. Solving Eq. 2.20 is equivalent to solving the following set of single-particle Schrödinger equations for the variational wave-functions of fictitious non-interacting electrons

$$\left(-\frac{\hbar^2}{2m} \nabla^2 + V_{\mathrm{KS}}[n(\mathbf{r})] \right) \phi_j(\mathbf{r}) = \epsilon_j \phi_i(\mathbf{r}) \tag{2.26}$$

where $\phi_i(\mathbf{r})$ and ϵ_j are wave-function of a non-interacting single particle and eigen-values, respectively. $\rho(\mathbf{r})$ is defined as

$$\rho(\mathbf{r}) = \sum_j^{\mathrm{occ}} \mid \phi_j(\mathbf{r}) \mid^2 \tag{2.27}$$

which requires that the solution be obtained self-consistently. In addition, when this self-consistency is reached, $T_o[\rho(\mathbf{r})]$ can be evaulated as

$$T_o \; [\rho(\mathbf{r})] = \sum_j < \phi_j \mid \epsilon_j - V_{\mathrm{KS}} \; [\rho(\mathbf{r})] \mid \phi_j > \tag{2.28}$$

However, in Eq. 2.17, the functional $E_{\mathrm{xc}}[n(\mathbf{r})]$ is still unknown. The exchange-correlation energy includes the exchange energy as well as correlation energy. The electrons will tend to dynamically repel other electrons from their regions of space through Coulombic repulsion, creating a correlation hole, and this is incorporated in the E_{xc}. The exchange correlation energy is hard to express in terms of the charge density. We use the local density approximation to express E_{xc}.

2.3.2.3 Local Density Approximation

The local density approximation (LDA) approximates E_{xc} as

$$E_{\mathrm{xc}}[\rho] \simeq \int \epsilon_{\mathrm{xc}}[\rho(\mathbf{r})]\rho(\mathbf{r})d^3r \tag{2.29}$$

where $\epsilon_{\mathrm{xc}}[\rho(\mathbf{r})]$ is the exchange-correlation energy per unit volume of a homogeneous electron gas density $\rho(\mathbf{r})$. The exchange-correlation potential is given by the following expression:

$$\begin{aligned} \mu_{\mathrm{xc}}^{LDA}(\mathbf{r}) &= \frac{\partial E_{\mathrm{xc}}[\rho(\mathbf{r})]}{\partial \rho} \\ &\simeq \frac{d}{d\rho(\mathbf{r})}\left(\rho(\mathbf{r})\epsilon_{\mathrm{xc}}[\rho(\mathbf{r})]\right) \\ &= \epsilon_{\mathrm{xc}}[\rho(\mathbf{r})] + \rho(\mathbf{r})\epsilon'_{\mathrm{xc}}[\rho(\mathbf{r})]. \end{aligned} \tag{2.30}$$

There are many prescriptions available in the literature for ϵ_{xc}. The Ceperley-Alder [11] approximation is considered to be the most accurate one and its parametrisation by Perdew and Zunger [12] makes it straight forward to use. The ϵ_{xc} is written in two parts:

$$\epsilon_{\mathrm{xc}} = \epsilon_{\mathrm{x}} + \epsilon_{\mathrm{c}} \tag{2.31}$$

with

$$\epsilon_x = -\frac{0.4582}{r_s} \tag{2.32}$$

in Hartrees and

$$\epsilon_c = \begin{cases} -0.1423/(1 + 1.0529\sqrt{r_s} + 0.3334r_s) & \text{for } r_s \geq 1, \\ -0.0480 + 0.0311\ln r_s - 0.0116r_s + 0.0020r_s\ln r_s & \text{for } r_s < 1, \end{cases} \tag{2.33}$$

in Hartrees. The parameter r_s is related to the density through the relation $\rho^{-1}=\frac{4\pi}{3}\mathrm{r}_s^3$. The exchange-correlation potential is obtained as

$$V_{\mathrm{xc}} = \epsilon_{\mathrm{xc}} - \frac{r_s}{3}\frac{d\epsilon_{\mathrm{xc}}}{dr_s} \tag{2.34}$$

2.4 Electron-Ion interaction

In Eq. 2.6 the term V_{ext} describes the potential between valence electrons and ion cores. Two alternative representations in numerical computation of the eigensolutions of Eq. 2.6 have become important; the real space representation and momentum space representation. Despite their differences each method faces similar practical diffuculties associated with the singularity that the electron-ion interaction possesses at each atomic site, due to the Coulomb potential. It has a singulartiy at each ionic site where the electron-ion potential tends to minus infinity. There are two common approaches used to treat V_{ext}: all-electron and pseudopotential approaches.

2.4.1 All-electron methods

All-electron methods may be classified in two groups, Linearized Muffin-Tin Orbitals (LMTO) and Full potential linearized augmented plane waves (FLAPW). In both methods, the electron-ion interaction is considered as a coulomb potential. However, in these methods the wave-functions are taken in differently. The self-consistent LMTO method has succesfully been applied to the study of the electronic and ground-state properties of metals and semiconductors. Skriver [13] has described the LMTO method in great depth. In the LMTO method, empty spheres are introduced at interstitial sites, and the wavefunction is the written as a sum of atomic orbitals both on site and in the empty sphere region. Some works in the past, for example Lambrect and Anderson [14] have shown that in the LMTO method a minimal basis set is sufficient for the calculation of one-electron energies and ground-state properties. However, it is difficult to know where to put the empty spheres which may lead to difficulties in the calculation of the forces using this method (due to a incomplete basis set). The FLAPW method is very well described by Wimmer *et al.* [15]. Actually this method is generalized by moving shape approximation to the potential inside the atomic sphere. Inside the spheres atomic orbitals are used as many spherical harmonics. On the other hand, outside the spheres many plane-waves are used. Therefore, the matching at the boundary of spheres must be done very carefully. Wei *et al.* [16] using this method, calculated energy bands, equilibrium lattice constant, bulk modulus, and cohesive energy of Tungsten. They found excellent agreement with related experimental results. However, as in the case of the LMTO, this method also suffers from rather inaccurate force calculations.

2.4.2 Pseudopotential method

An atom may be considered in three parts; nucleus, core electrons and valence electrons. The core electrons are those in the filled orbitals, e.g. the $1s^2$, $2s^2$, and $2p^6$ electrons in the core of Si. These core electrons are mostly localized around the nucleus, so they can be lumped together with the nucleus to form the so-called ion core. The pseudopotential is non-singular because it includes the screening of the nucleus by the tightly bound core electrons. In the pseudopotential approach the valence electrons are explicitly considered while it is assumed that ion cores do not play any role in determining electronic properties of moleculed or solids. This means that both ionic core states and the strong potentials responsible for binding them can be dropped out of consideration in electronic structure. Assume that the real wavefunction ψ has a smooth part ϕ plus a core part which can be expanded in core states, ϕ_c:

$$\psi = \phi + \sum_c b_c \phi_c. \tag{2.35}$$

b_c is determined from the condition that ψ and ϕ_c are orthogonal to each other.

$$\langle \phi_c \mid \psi \rangle = 0 = \langle \phi_c \mid \phi \rangle + b_c. \tag{2.36}$$

Using the values of b_c from Eq. 2.36, Schrödinger's equation can be written as

$$H\phi + \sum_c (\epsilon - E_c) \mid \phi_c \rangle \langle \phi_c \mid \phi = \epsilon \phi \tag{2.37}$$

where E_c is a core-state eigenvalue. This equation can be expressed as

$$(H + V_R)\phi = \epsilon \phi \tag{2.38}$$

or

$$(T + V_{\text{ps}})\phi = \epsilon\phi, \tag{2.39}$$

where V_R, is defined by Eq. 2.37, is repulsive potential operator. Phillips and Kleinman[17] showed that the operator

$$V_{ps} = V_A + V_R \tag{2.40}$$

is a weak and smooth potential operator called a pseudopotential. The potential cancellation between the repulsive potential V_R and the attractive core potential V_A is known as the Phillips cancellation theorem. Eq. 2.39 can be solved for eigenvalues using smooth wavefunctions via a plane-wave basis set and weak potentials. While the eigenvalues from Eq. 2.39 are the same as from Eq. 2.1, the wavefunction ψ is not the same as ϕ. Eq. 2.39 is the pseudopotential transformation of the Schrödinger like Kohn-Sham Equations. The latter is used in the construction of the norm-conserving (i.e., the total charge within the core radius is the same for the pseudowavefunction as for the true wavefunction), an *ab initio* non-local pseudopotential [18, 19, 20, 21].

2.5 Translation of electronic Kohn-Sham equations into momentum space

In order for Eq. 2.39 to be translated into momentum space, it can be written as

$$(T + V_{\text{ps}})\phi_{\mathbf{k},n}(\mathbf{r}) = \epsilon_{\mathbf{k},n}\phi_{\mathbf{k},n}(\mathbf{r}), \tag{2.41}$$

where $\mathbf{r}$ is the electronic position, $\mathbf{k}$ is the electron's wavevector in the first Brillounin zone and n is energy band index. For a crystalline solid, $V_{\text{ps}}(\mathbf{r})$ may be expanded using a Fourier expansion

$$V_{\text{ps}}(\mathbf{r}) = \sum_{\mathbf{G}} V(\mathbf{G})e^{(i\mathbf{G}\cdot\mathbf{r})}, \tag{2.42}$$

where $\mathbf{G}$ is a reciprocal lattice vector and one has assumed that V_{ps} is a local potential (i.e. V_{ps}=$V_{\text{ps}}(\mathbf{r})$). And, $V(\mathbf{G})$ is called the Fourier component of V_{ps}.

To solve the Kohn-Sham equations with pseudopotentials, the standard approach is to expand the electron wavefunctions. Mainly, the wavefunction can be expressed in three different ways.

a) Express ϕ as a linear combination of plane waves

b) Express ϕ as a linear combination of some plane waves and some atomic orbitals.

c) Express ϕ as a linear combination of atomic orbitals(LCAO or tight binding method)

We use a plane wave basis set in our calculations. Test of convergence in the basis expansion can be done by simply increasing the number of plane waves used. For systems with higly localized electrons such as the transition metals and large-gap insulators, a plane wave basis set would not be suitable. Other more judicious choices of basis functions have to be used. One approach is to use a mixed-basis set [22]. The electron wavefunction is expanded in a combined set of plane waves and Bloch sums of atom-centered Gaussian orbitals. The mixed basis set is most suitable for efficient description of systems with both highly localised (atomic-like) electrons and delocalised (plane wave-like) electrons. Another approach is to use a linear combination of atomic-like orbitals (LCAO) basis [23]. This is probably the most efficient basis for calculating the total energy of complex systems.

In terms of plane waves for an electron with wave vector $\mathbf{k}$ in band n,

$$\phi_{\mathbf{k},n}(\mathbf{r}) = \frac{1}{\sqrt{N_o\Omega}} \sum_{\mathbf{G}} A_{\mathbf{k},n}(\mathbf{k}+\mathbf{G}) e^{i(\mathbf{k}+\mathbf{G})\cdot\mathbf{r}} \tag{2.43}$$

where $N_o\Omega$ is the volume of the crystal and $\mathbf{G}$ is a reciprocal vector. The electronic wavevector, $\mathbf{k}$, lies within the first Brillouin zone. The size of the basis set (i.e. the number of plane waves) is considered by imposing an upper cut-off to the kinetic energy $\frac{\tilde{}^2}{2m}(\mathbf{k}+\mathbf{G})^{\mathbf{2}} \leq \mathrm{E_{cut}}$. $A_{\mathbf{k},n}(\mathbf{k}+\mathbf{G})$ is a Fourier space representation of $\phi_{\mathbf{k},n}(\mathbf{r})$. Substituting Eq. 2.42 and Eq. 2.43 into Eq. 2.41 one can get

$$\sum_{\mathbf{G}} A_{\mathbf{k},n}(\mathbf{k}+\mathbf{G}) \left\{ \frac{\hbar^2(\mathbf{k}+\mathbf{G})^2}{2m} + \sum_{\mathbf{G'}} V(\mathbf{G'}) e^{i\mathbf{G'}.\mathbf{r}} - \epsilon_{\mathbf{k},n} \right\} e^{i(\mathbf{k}+\mathbf{G})\cdot\mathbf{r}} = 0. \tag{2.44}$$

After some mathematical manipulation it may be written as

$$\sum_{\mathbf{G}} A_{\mathbf{k}}(\mathbf{k}+\mathbf{G}) \left[\left\{ \frac{\hbar^2(\mathbf{k}+\mathbf{G})^2}{2m} - \epsilon_{\mathbf{k},n} \right\} \delta_{\mathbf{G},\mathbf{G}'} + V_{\mathrm{ps}}(\mathbf{G}'-\mathbf{G}) \right] = 0. \tag{2.45}$$

Eq. 2.45 is the momentum space representation of the Schrödinger Eq. 2.39 or Eq. 2.41. Non-trivial solutions of equation Eq. 2.45 are obtained by solving the determinantal equation

$$\left| \left(\frac{\hbar^2(\mathbf{k}+\mathbf{G})^2}{2m} - \epsilon_{\mathbf{k},n} \right) \delta_{\mathbf{G},\mathbf{G}'} + V_{\mathrm{ps}}(\mathbf{G}'-\mathbf{G}) \right| = 0. \tag{2.46}$$

A Fourier component of the screened pseudopotential, $V_{\mathrm{ps}}(\mathbf{G}'-\mathbf{G})$ can be expressed as

$$V_{\mathrm{ps}}(\mathbf{G}'-\mathbf{G}) = W_{\mathrm{ps}}(\mathbf{G}'-\mathbf{G}) + V_{\mathrm{H}}(\mathbf{G}'-\mathbf{G}) + V_{\mathrm{xc}}(\mathbf{G}'-\mathbf{G}) \tag{2.47}$$

where W_{ps} is the ionic pseudopotential. Consider that the crystal potential, $\mathrm{V}_{\mathrm{ps}}(\mathbf{r})$ can be constructed as a sum of non-overlapping atomic pseudopotentials.

$$\begin{aligned} V_{\mathrm{ps}}(\mathbf{r}) &= \sum_{j=\mathrm{all\ atoms}} v_j^{\mathrm{atomic}}(\mathbf{r}) \\ &= \sum_p \sum_b v_b^{\mathrm{at}}(\mathbf{r}-\mathbf{p}-\tau_b) \end{aligned} \tag{2.48}$$

where $\mathbf{p}$ is a general lattice point or vector, τ is a basis atom vector or position of the bth ion in the primitive unit cell and $\mathbf{r}$ the electron position. Next assume that $v^{\mathrm{at}}(\mathbf{r}-\mathbf{p}-\tau_b) = v^{\mathrm{at}}(\mid \mathbf{r}-\mathbf{p}-\tau_b \mid)$. Then,

$$\begin{aligned} V_{\mathrm{ps}}(\mathbf{r}) &= \sum_p \sum_b v_b(|\mathbf{r}-\mathbf{p}-\tau_{\mathbf{b}}|) \\ &= \sum_{\mathbf{G}} V(\mathbf{G}) e^{i\mathbf{G}\cdot\mathbf{r}} \end{aligned} \tag{2.49}$$

Multiply by $e^{-i\mathbf{G}'\cdot\mathbf{r}}$ and integrate over all space to get

$$\sum_{\mathbf{G}} \int V(\mathbf{G}) e^{i(\mathbf{G}-\mathbf{G}')\cdot\mathbf{r}} d\mathbf{r} = N_o \Omega V(\mathbf{G}) \tag{2.50}$$

Let $\mathbf{r}'$=$\mathbf{r}-\mathbf{p}-\tau_{\mathbf{b}}$ and $d\mathbf{r}'$=$d\mathbf{r}$ then after some mathematical derivation one can get

$$\begin{aligned} V(\mathbf{G}) &= \frac{1}{N_o\Omega}\sum_p\sum_b\int d\mathbf{r}v_b^{\mathrm{at}}(\mid \mathbf{r}-\mathbf{p}-\tau_b\mid)e^{-i\mathbf{G}\cdot\mathbf{r}} \\ &= \frac{1}{N_o\Omega}\sum_p\sum_b\int d\mathbf{r}'v_b^{\mathrm{at}}(\mid \mathbf{r}'\mid)e^{-i\mathbf{G}\cdot(\mathbf{r}'+\mathbf{b}+\tau_b)} \\ &= \frac{1}{N_oM\Omega_{at}}\sum_p\sum_b e^{-i\mathbf{G}\cdot(\mathbf{b}+\tau_b)}\int d\mathbf{r}v_b^{\mathrm{at}}(\mid \mathbf{r}\mid)e^{-i\mathbf{G}\cdot(\mathbf{r})} \end{aligned} \tag{2.51}$$

where N_o is the number of unit cells, Ω is the unit cell volume and M is the number of atoms in a unit cell. Now we can write

$$\begin{aligned} V(\mathbf{G}) &= \left[\frac{1}{M}\sum_{\mathbf{b}}e^{-i\mathbf{G}\cdot\tau_b}v_b^{\mathrm{at}}(|\mathbf{G}|)\right] \\ &= S(\mathbf{G})v(|\mathbf{G}|) \end{aligned} \tag{2.52}$$

where S($\mathbf{G}$) and v($\mathbf{G}$) are a structure factor and local atomic form factor or atomic pseudopotential, respectively.

2.5.1 Structure factor

The $S(\mathbf{G})$ depends (i) on $\mathbf{G}$ and (ii) on atomic positions in the unit cell. For example, let there be two kinds of atom α and β in the crystal and let their positions inside the primitive cell be denoted by $\tau_{\alpha b}$ and $\tau_{\beta b}$. The structure factor can be written

$$S_\alpha(\mathbf{G}) = \frac{1}{M_\alpha}\sum_{\mathbf{b}}e^{-i\mathbf{G}\cdot\tau_{\alpha b}}. \tag{2.53}$$

The structure factor of atom β is defined similarly.

2.5.2 Non-local atomic form-factor

$v_b^{\mathrm{at}}(\mathbf{G})$ depends on $|\mathbf{G}|$ (i.e. on the magnitude of $\mathbf{G}$) and does not depend on where the atom is. It shows the strength of the atomic pseudopotential. In general v_b^{at} is non-local, with a Fourier component as

$$
\begin{aligned}
v(\mathbf{k}+\mathbf{G},\mathbf{k}+\mathbf{G}^{'}) &= v_b(\mathbf{q},\mathbf{q}^{'}) \\
&= \frac{1}{\Omega_{\text{at}}}\int d\mathbf{r}e^{-i\mathbf{q}^{'}\cdot\mathbf{r}}\widehat{v}_b(\mathbf{r})e^{i\mathbf{q}\cdot\mathbf{r}}
\end{aligned} \tag{2.54}
$$

where $\widehat{v}_b(\mathbf{r})$ is an angular momentum dependent operator.

$$
v_b(\mathbf{q},\mathbf{q}^{'}) = \int d\mathbf{r}e^{-i\mathbf{q}^{'}\cdot\mathbf{r}}\left[\sum_l v_{b,l}(\mathbf{r})\widehat{P}_l\right]e^{i\mathbf{q}\cdot\mathbf{r}} \tag{2.55}
$$

where $\widehat{P}_l$ is the projection operator for angular momentum l. In other words, we can write

$$
\begin{aligned}
\widehat{v}_b(\mathbf{r}) &= \sum_l v_{b,l}(\mathbf{r})\widehat{P}_l \\
&= \sum_l \widehat{P}_l v_{b,l}(|\mathbf{r}|)\widehat{P}_l
\end{aligned} \tag{2.56}
$$

a sum of operators with different angular momentum compenents. Then

$$
v_b(\mathbf{q},\mathbf{q}^{'}) = \frac{1}{\Omega}\int d^3re^{-i\mathbf{q}^{'}\cdot\mathbf{r}}\left[\sum_l \widehat{P}_l v_{b,l}(|\mathbf{r}|)\widehat{P}_l\right]e^{i\mathbf{q}\cdot\mathbf{r}} \tag{2.57}
$$

Now expand the plane wave $e^{i\mathbf{q}\cdot\mathbf{r}}$ into spherical harmonics

$$
e^{i\mathbf{q}\cdot\mathbf{r}} = 4\pi\sum_{l_1m_1}(i)^{l_1}j_{l_1}Y_{l_1m_1}(\widehat{\mathbf{r}})Y^{\star}_{l_1m_1}(\widehat{\mathbf{q}}) \tag{2.58}
$$

where j is the spherical Bessel function and $\sum_m Y_{lm}(\widehat{\mathbf{q}}^{'})Y^{\star}_{lm}(\widehat{\mathbf{q}}) = \frac{2l+1}{2m}P_l(\widehat{\mathbf{q}}\cdot\widehat{\mathbf{q}}^{'})$. Then,

$$
v_b(\mathbf{q},\mathbf{q}^{'}) = \frac{4\pi}{\Omega}\sum_l(2l+1)v_{b,l}(|\mathbf{q}|,|\mathbf{q}|^{'})P_l(\widehat{\mathbf{q}}\cdot\widehat{\mathbf{q}}^{'}) \tag{2.59}
$$

$P_l(\widehat{\mathbf{q}}\cdot\widehat{\mathbf{q}}^{'})$ is a Legendre polynomial and

$$
\begin{aligned}
v_{b,l}(|\mathbf{q}|,\left|\mathbf{q}^{'}\right|) &\equiv v_{b,l}(\mathbf{q},\mathbf{q}^{'}) \\
&= \int_0^{\infty} drdr^2v_{b,l}(r)j_l(qr)j_l(q^{'}r).
\end{aligned} \tag{2.60}
$$

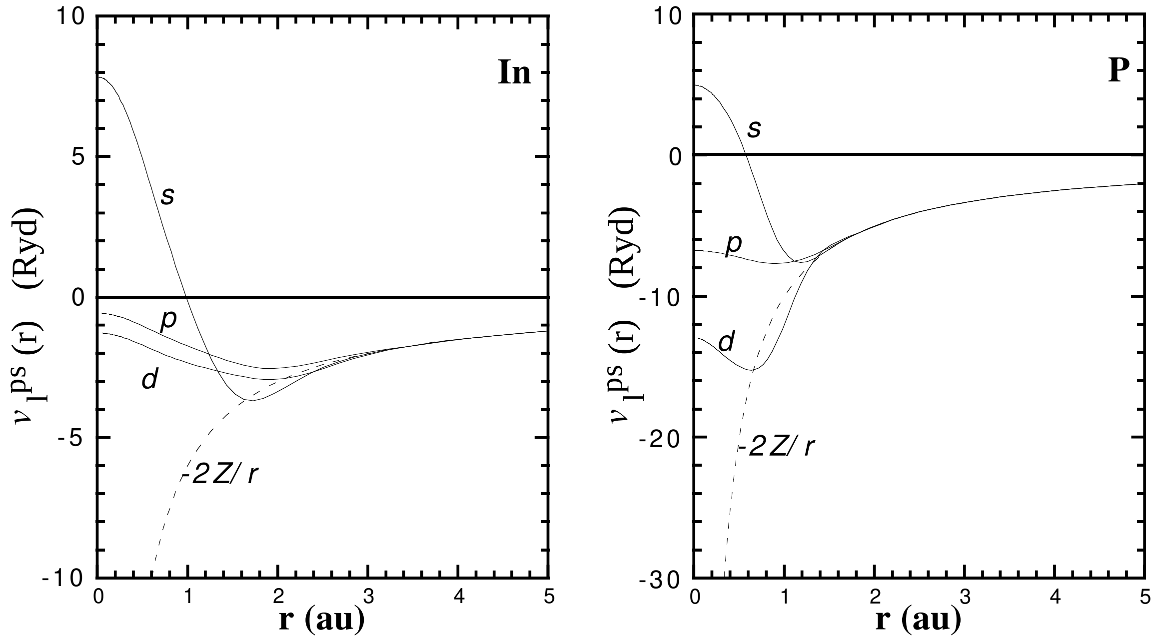

Figure 2.1: Nonlocal ionic pseudopotential for In and P generated using Bachelet *et al.* The potentials for angular momentum l=0, l=1, and 2 are shown. The dash line represents the Coulomb (All-electron) potential.

Therefore,

$$\begin{aligned} v_b(\mathbf{q},\mathbf{q}') &= \frac{4\pi}{\Omega}\sum_l (2l+1)P_l(\widehat{\mathbf{q}}\cdot\widehat{\mathbf{q}}') \\ &\times \int_0^\infty dr dr^2 v_{b,l}^{\mathrm{at}} j_l(|\mathbf{k}+\mathbf{G}|\,\mathbf{r}) j_l(\left|\mathbf{k}+\mathbf{G}'\right|\mathbf{r}) \end{aligned} \tag{2.61}$$

v^{atom} is generally weaker than v^{ion} due to screening effect. In our work we use $v_{b,l}^{\mathrm{ion}}(r)$ in the form published by Bachelet *et al.*, who calculated norm-conserving ionic pseudopotentials from atomic calculations for all the elements, including relativistic effects, and fitted their results with a relatively small set of analytic functions, the parameters of which were tabulated [20].

Fig. 2.1 shows the ion-core pseudopotential (l=0,1,2 for Indium and Phosphorus), generated using the form given in Bachelet *et al.* The dashed curve corresponds to the all-electron Coulomb potential.

2.6 Energy derivative with respect to ionic position

The first derivative of the total energy can be obtained in a straithforward manner, due to the result described below. The first derivative components give the forces on the ions,

$$F_i = -\frac{\partial E}{\partial x_i} \tag{2.62}$$

where x_i refers to a single ionic degree of freedom.

The total energy E may be written as

$$E =< \Psi \mid \hat{H}_{\mathrm{KS}} \mid \Psi > \tag{2.63}$$

where $\hat{H}_{\mathrm{KS}}$ is the approximate form of the Kohn-Sham Hamiltonian described in the previous section and Ψ is the normalised wavefunction of the fictitious set of non-interacting electrons introduced in the Kohn-Sham formulation.

Thus,

$$\begin{aligned} F_i &= -\frac{\partial}{\partial x_i} < \Psi \mid \hat{H}_{\mathrm{KS}} \mid \Psi > \\ &= - < \frac{\partial \Psi}{\partial x_i} \mid \hat{H}_{\mathrm{KS}} \mid \Psi > - < \Psi \mid \frac{\partial \hat{H}_{\mathrm{KS}}}{\partial x_i} \mid \Psi > - < \Psi \mid \hat{H}_{\mathrm{KS}} \mid \frac{\partial \Psi}{\partial x_i} > \end{aligned} \tag{2.64}$$

However, $\hat{H}_{\mathrm{KS}}$ is a Hamiltonian operator and, when the electrons are in their ground state, Ψ is an eigenfunction of this operator:

$$\hat{H}_{\mathrm{KS}} \Psi = E \Psi. \tag{2.65}$$

Hence we can simplify Eq. 2.64 to

$$F_i = -\left[E < \frac{\partial \Psi}{\partial x_i} \mid \Psi > + E < \Psi \mid \frac{\partial \Psi}{\partial x_i} > + < \Psi \mid \frac{\partial \hat{H}_{\mathrm{KS}}}{\partial x_i} \mid \Psi > \right]. \tag{2.66}$$

The first two terms of this can be written as

$$E \frac{\partial}{\partial x_i} < \Psi \mid \Psi > \tag{2.67}$$

and as $< \Psi \mid \Psi >$ is just the normalisation of the wavefunction this will be constant, with a derivative equal to zero. We therefore arrive at the result that the first derivative of the energy is just the expectation value of the derivative of the Hamiltonian,

$$F_i = - < \Psi \mid \frac{\partial \hat{H}_{\text{KS}}}{\partial x_i} \mid \Psi > \tag{2.68}$$

a result known as the Hellmann-Feynman theorem[24].

Finally, once the ground state Kohn-Sham wavefunction is known the forces may be evaluated. There is no need to calculate the derivative of the wavefunction with respect to the ionic position in order to obtain these first derivatives. However, it is important to note that this result relies upon the wavefunction being the true eigenstate of the Kohn-Sham Hamiltonian.

2.7 Brillouin zone summation

The sum over $\mathbf{k}$ in Eq. 2.46 demands eigenvectors at all $\mathbf{k}$-points considered within the Brillouin Zone (BZ). The computational load in most cases can be reduced by using a 'special points' schemes [2, 3]. In practice, symmetry arguments are used to sample $\mathbf{k}$-points withing the irreducible segment of BZ.

For a system with translational symmetry Bloch's theorem applies, which introduces a symmetry label $\mathbf{k}$ for the wavefunctions. The density in then given by integrating over all values of $\mathbf{k}$ in the first BZ,

$$n(\mathbf{r}) = \frac{1}{\Omega_{BZ}} \int_{1\text{BZ}} n(\mathbf{k}) d(\mathbf{k}) \tag{2.69}$$

where $n(\mathbf{k}) = \sum_{i=1}^{N} |\phi_{i,\mathbf{k}}|^2$

The problem of calculating wavefunctions for an infinite number of electrons has become that of calculating for a finite number of electrons at an infinite number of $\mathbf{k}$-points. However, we would expect properties to vary smoothly across the BZ, so the integral can be approximated by sampling at a finite of points, $\mathbf{k}_j$, with appropriated weights, w_j,

$$n = \sum_j w_j n(\mathbf{k_j}). \tag{2.70}$$

Various schemes have been suggested for efficient choices of these points, e.g., those of Baldereschi [25], Monkhorst and Pack [26], and Chadi and Cohen [27]. A good description of special **k**-points for crystals of different symmetries and their use in the calculation of electronic structure and physical properties of solids is presented by Evarestov and Smirnov [28].

2.8 Plane Wave LDA Code

We investigate of the microscopic properties of semiconductors in both bulk and surface conditions through the use of a sophisticated LDA computer code, known as EKSETER (standing for Evaluation of the Kohn-Sham Equation for Total Energy and Relaxation). This code, originated by Dr. GP Srivastava, has undergone over fifteen years of development and is continually being refined to extend its accuracy and range of applicability. Essentially the code implements the hugely successful density functional theory (DFT) of Hohenberg and Kohn (1964) and Kohn and Sham (1965) as explained previously. The following sections explain briefly the computational process.

In order that a method may correctly model the redistribution of charge from one atom to another, it is essential to perform electronic structure calculations self consistently. Self-consistency simply means that the charge density generated by an external potential is the same as the charge density that generated that potential, to within some tolerance.

Our method uses ionic pseudopotentials and a model for the crystal structure as the starting point of the calculation. After the wave functions have been obtained the contribution of the valence electrons to the potential is calculated. It is then used to evaluate the total one-electron potential, which is compared with the starting potential. Self-consistency is achieved when the calculated one-electron potential agrees with the sarting potential.

Our computational procedure is as follows:

(i) Take (or expand) $\phi_j(\mathbf{r})$ in plane waves.

(ii) Make a rough guess for $\mathrm{V_{KS}} \Rightarrow$ [call it $\mathrm{V_{KS}^{(in)}}$].

(iii) Solve Eq. 2.26 for $\phi_j(\mathbf{r})$ and ϵ_j.

(iv) Calculate density using $\rho(\mathbf{r}) = \phi_{\mathbf{j}}^{*}\phi_{\mathbf{j}}$.

(v) Then construct $V_{\mathrm{KS}}[\rho] = V_{\mathrm{ps}}^{\mathrm{ion}}(\mathbf{r}) + V_H[\rho] + V_{\mathrm{xc}}[\rho] \Rightarrow$ [call it $V_{\mathrm{KS}}^{(\mathrm{out})}$]. $V_{\mathrm{KS}}^{\mathrm{out}}$ is usually very different from $V_{\mathrm{KS}}^{(\mathrm{in})}$.

(vi) Mix $V_{\mathrm{KS}}^{\mathrm{in}}$ and $V_{\mathrm{KS}}^{\mathrm{out}}$ to generate a new V_{KS} which is;

$$V_{\mathrm{KS}}^{(\mathrm{new})} = \alpha V_{\mathrm{KS}}^{(\mathrm{in})} + (1-\alpha) V_{\mathrm{KS}}^{(\mathrm{out})}, \quad 0 \leq \alpha \leq 1 \tag{2.71}$$

for the first two iterations. After the 2$^{\mathrm{nd}}$ iteration, use the Jacobian update method [29] to accelerate the process (until $V_{\mathrm{KS}}^{(\mathrm{out})} \simeq V_{\mathrm{KS}}^{(\mathrm{out})}$).

(vii) Repeat the process: this is the self-consistent field theory.

We now discuss methods for finding eigenvalues and eigenvectors. Eq. 2.45 is a complex hermitain matrix of size N×N. It can be solved as an eigenvalue problem. There are many iterative techniques available to solve it, (i) Houselholder method solves the N×N problem in a straigth forward manner. However, if the dimension of the matrix is large enough (i.e., 2000), (ii) Conjugate gradients minimisation method or (iii) Residual minimisation by direct inversion in interactive subspace technique [4, 29] is used. The last two methods start with a small part of the matrix, then begin an iterative procedure to find the solutions for full dimensions of matrix. Having solved for $\phi_j(\mathbf{r})$ and ϵ_j, $n(\mathbf{r})$ can be constructed from $\phi_j(\mathbf{r})$.

After the solutions of the Kohn-Sham equation are obtained for a given ionic configuration self-consistently, it is possible to calculate the forces on the ions using the Hellmann-Feynman theorem. Using these forces as a guide the code then moves the atoms to a second *test* configuration and solves the Kohn-Sham equation once again [4]. At this point we know the total energy of both configurations and all the forces in both configurations. This information allows the code to minimise the total energy by finding the third configuration somewhere between the first and second. Subsequently the code refines the ionic configuration by making successive adjustments in a similar manner. At each step the *test* configuration is found using both the Hellmann-Feynman forces and the constraint that each relaxation must be conjugate to all previous relaxations in the configuration space.

2.9 Surface Brillouin Zone

The reciprocal lattice is generated by an equation like

$$\mathbf{G_m} = \sum_{\mathbf{j=1,2,3}} \mathbf{m_j b_j} \tag{2.72}$$

where the m_j's are positive, negative or zero integers and $\mathbf{b}_j$ are the primitive translation vectors of the reciprocal lattice. The volumes of the unit cells of the direct and reciprocal lattices are given as

$$\Omega = \mathbf{a_1} \cdot (\mathbf{a_2} \times \mathbf{a_3}), \qquad \Omega^{'} = \mathbf{b_1} \cdot (\mathbf{b_2} \times \mathbf{b_3}). \tag{2.73}$$

where $\mathbf{a_1}$, $\mathbf{a_2}$ and $\mathbf{a_3}$ were given in Eq. 1.2. The primitive translation vectors of the reciprocal lattice are defined in terms of the primitive translation vectors of the direct lattice,

$$\begin{aligned} \mathbf{b_1} &= \frac{2\pi}{\Omega}(\mathbf{a_2} \times \mathbf{a_3}) \\ \mathbf{b_2} &= \frac{2\pi}{\Omega}(\mathbf{a_3} \times \mathbf{a_1}) \\ \mathbf{b_3} &= \frac{2\pi}{\Omega}(\mathbf{a_1} \times \mathbf{a_2}). \end{aligned} \tag{2.74}$$

From these equations the primitive translation vectors of the reciprocal lattice of the fcc direct space lattice are found

$$\begin{aligned} \mathbf{b_1} &= \frac{2\pi}{a}(-1, 1, 1) \\ \mathbf{b_2} &= \frac{2\pi}{a}(1, -1, 1) \\ \mathbf{b_3} &= \frac{2\pi}{a}(1, 1, -1). \end{aligned} \tag{2.75}$$

Thus, the reciprocal lattice is body-centered. The first Brillouin zone is shown in Fig. 2.2. However, only $\frac{1}{48}$ of this zone is unique, the remaining being symmetrically

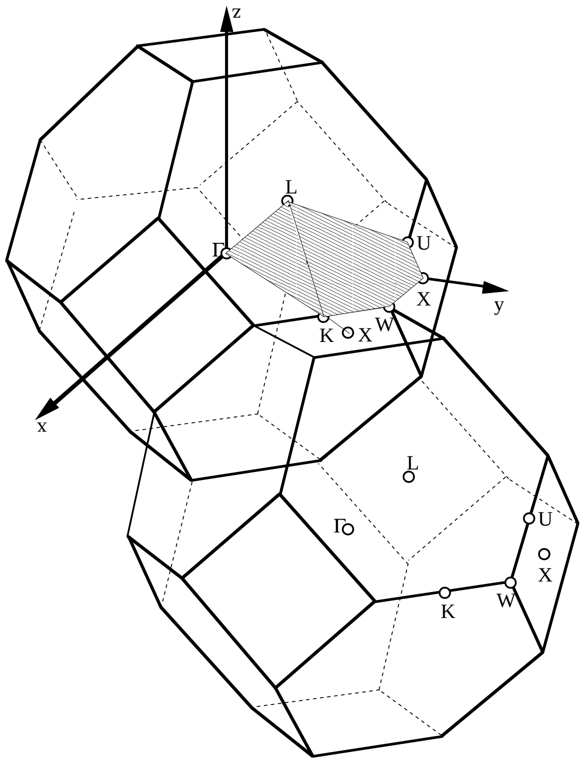

Figure 2.2: The first Brillouin zone of a face-centred cubic lattice.

equivalent to the points in this segment [3]. The unique segment (irreducible part of the Brillouin zone) is shown in Fig. 2.2 by the dashed area. The main symmetry directions are

$$\begin{aligned}\Delta &= \Gamma(0,0,0) - X(0, \frac{2\pi}{a}, 0)\\ \Lambda &= \Gamma(0,0,0) - L(\frac{\pi}{a}, \frac{\pi}{a}, \frac{\pi}{a})\\ \Sigma &= \Gamma(0,0,0) - K(\frac{3\pi}{2a}, \frac{3\pi}{2a}, 0).\end{aligned} \tag{2.76}$$

2.9.1 Surface Brillouin Zone for the (110) surfaces

We describe the surface Brillouin zone by identifying an artificial periodicity in the direction perpendicular to the surface. For unreconstructed III-V(110) surfaces, three translation vectors,

$$\begin{aligned}
\mathbf{a_1} &= \frac{a}{2}(-1,1,0) \\
\mathbf{a_2} &= \frac{a}{2}(0,0,2) \\
\mathbf{a_3} &= c(1,1,0),
\end{aligned} \tag{2.77}$$

are chosen. $\mathbf{a_1}$, $\mathbf{a_2}$ are the primitive translation vectors in the surface plane, and the vector perpendicular to the surface $\mathbf{a}_3$ is constructed with arbitrarily chosen value of the lattice contant c. The primitive translation vectors of the reciprocal lattice are given as

$$\begin{aligned}
\mathbf{b_1} &= \frac{2\pi}{\Omega}(\mathbf{a_2} \times \mathbf{a_3}) = \frac{2\pi}{|a_1|}\widehat{\mathbf{a}}_1 \\
\mathbf{b_2} &= \frac{2\pi}{\Omega}(\mathbf{a_3} \times \mathbf{a_1}) = \frac{2\pi}{|a_2|}\widehat{\mathbf{a}}_2 \\
\mathbf{b_3} &= \frac{2\pi}{\Omega}(\mathbf{a_1} \times \mathbf{a_2}) = \frac{2\pi}{|a_3|}\widehat{\mathbf{a}}_3
\end{aligned} \tag{2.78}$$

where $\Omega = |\mathbf{a_1}.(\mathbf{a_2} \times \mathbf{a_3})|$. A surface reciprocal lattice vector may be defined by setting $\mathbf{b}_3$ to zero and expressing

$$\begin{aligned}
\mathbf{G} &= m_1\mathbf{b_1} + m_2\mathbf{b_2} \\
&= \{m_1, m_2\},
\end{aligned} \tag{2.79}$$

where m_1 and m_2 are integers. The primitive unit cell of the reciprocal lattice of the surface is the area defined by $\mathbf{b}_1$ and $\mathbf{b}_2$. The irreducible part of the surface Brillouin zone is shown in Fig. 2.3(a), where

$$\begin{aligned}
\bar{\Gamma} &= \{0,0\} \\
\bar{X} &= \left\{\frac{1}{2},0\right\} \\
\bar{X}' &= \left\{0,\frac{1}{2}\right\} \\
\bar{M} &= \left\{\frac{1}{2},\frac{1}{2}\right\}.
\end{aligned} \tag{2.80}$$

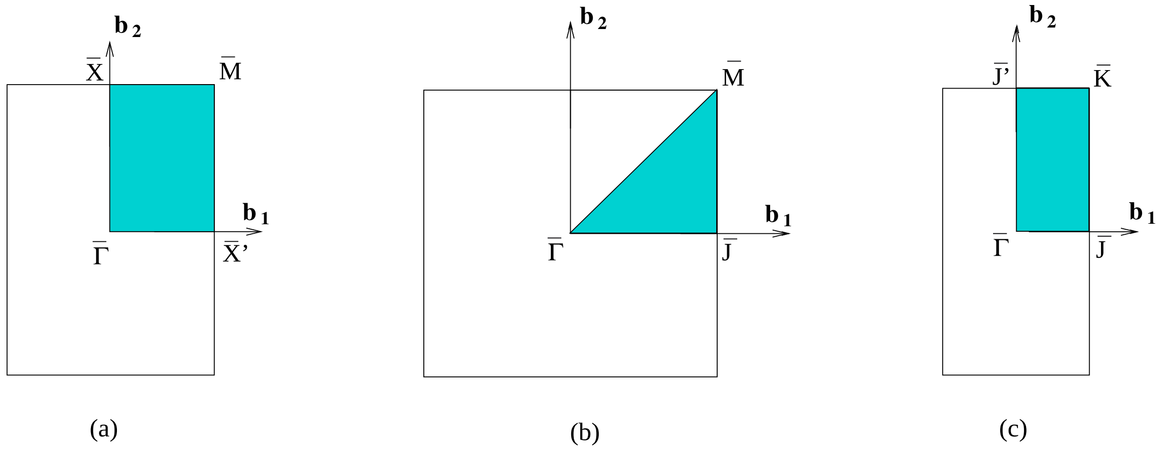

Figure 2.3: Surface Brillouin zones for the primitive (1×1) unit cell for the (a) (110), (b) (001) surfaces and (c) for the (2×1) unit cell of the (001) surface.

2.9.2 Surface Brillouin Zone for the (001) surfaces

The real-space lattice vectors for the (1×1) pattern are

$$\mathbf{a_1} = \frac{a}{2}(-1, 1, 0)$$

and

$$\mathbf{a_2} = \frac{a}{2}(1, 1, 0),$$

where a is the bulk cubic-lattice constant. The corresponding primitive reciprocal lattice vectors are

$$\mathbf{b_1} = \frac{2\pi}{a}(-1, 1, 0)$$

and

$$\mathbf{b_2} = \frac{2\pi}{a}(1, 1, 0).$$

In the (2×1) pattern the real-space lattice vectors are

$$\mathbf{a_1} = a(-1, 1, 0)$$

and

$$\mathbf{a_2} = \frac{a}{2}(1, 1, 0),$$

and their corresponding primitive reciprocal lattice vectors are

$$\mathbf{b_1} = \frac{2\pi}{a}(-1, 1, 0)$$

and

$$\mathbf{b_2} = \frac{2\pi}{a}(0.5, 0.5, 0).$$

The surface Brillouin zone is the Wigner-Seitz area obtained from perpendicularly bisecting the primitive reciprocal lattice vectors $\mathbf{b_1}$ and $\mathbf{b_2}$ from a chosen surface reciprocal lattice point. Fig. 2.3(a) shows the surface Brillouin zone for the unreconstructed (110) surface and Fig. 2.3(b) shows surface Brillouin zone for the (1×1) (001) surface. Fig. 2.3(c) shows the surface Brillouin zone for the (2×1) reconstructed (001) surface.

2.10 Summary

In this chapter, I have tried to give a relatively detailed description of the formalism and computational procedures I use in this thesis.

Bibliography

[1] J. T. Devreese and P. V. Camp, *Electronic Structure, Dynamics, and Quantum Structural Properties of Condensed Matter*, Plenum Press, New York, 1985.

[2] G. P. Srivastava and D. Weaire, Adv. Phys. **36**, 463 (1987).

[3] G. P. Srivastava, *The Physics of Phonons*, Adam Hilger, Bristol, 1990.

[4] A. Umerski and G. P. Srivastava, Phys. Rev. B **51**, 2334 (1995).

[5] W. G. Schmidt, F. Bechstedt and G. P. Srivastava, Surf. Sci. Rep. **25**, 141 (1996).

[6] G. P. Srivastava, Rep. Prog. Phys. **60**, 561 (1997).

[7] N. W. Ashcroft snd N. D. Mermin, *Solid State Physics*, Int. Ed., USA, 1976.

[8] G. Burns, *Solid State Physics*, International Edition, Acedemic Press, 1990.

[9] P. Hohenberg and W. Kohn, Phys. Rev. B **136**, 864 (1964).

[10] W. Kohn and L. J. Sham, Phys. Rev. A **140**, 1133 (1965).

[11] D. M. Ceperley and B. I. Alder, Phys. Rev. Lett. **45**, 566 (1980).

[12] J. P. Perdew and A. Zunger, Phys. Rev. B **23**, 5048 (1981).

[13] H. L. Skriver, *The LMTO Method-Miffin-Tin Orbitals and Electronic Structure*, Springer-Verlag, Berlin, 1984.

[14] W. R. L. Lambercht and O. K. Anderson, Phys. Rev. B **34**, 2439 (1986).

[15] E. Wimmer, H. Krakouer, M. Weinert, and A. J. Freeman, Phys. Rev. B **24**, 864 (1981).

[16] S. H. Wei, H. Krakauer and M. Weinert, Phys. Rev. B **32**, 7792 (1985).

[17] J. C. Phillips and L. Leinman, Phys. Rev. **116**, 287 (1959).

[18] D. R. Hamann, M. Schlüter and C. Chaing, Phys. Rev. Lett. **43**, 1494 (1979).

[19] G. Kerker, J. Phys. C **13**, L189 (1980).

[20] G. B. Bachelet, D. R. Hamann and M. Schlüter, Phys. Rev. B **26**, 4199 (1982).

[21] G. B. Bachelet, H. S. Greenside, G. A. Baraft, and M. Schlüter, Phys. Rev. B **24**, 4745 (1981).

[22] S. G. Louie, K. M. Ho, and M. L. Cohen, Phys. Rev. B **19**, 1774 (1979).

[23] J. R. Chelikowsky and S. G. Louie, Phys. Rev. B **29**, 3470 (1984).

[24] H. Hellmann, *Einführung in die Quantenchemie* (Deuticke, Leipzig 1937); R. P. Feynman Phys. Rev. **56**, 340 (1939).

[25] A. Baldereschi, Phys. Rev. B **7**, 4816 (1973).

[26] H. J. Monkhorst and J. D. Pack, Phys. Rev. B **13**, 5189 (1976).

[27] D. J. Chadi and M. L. Cohen, Phys. Rev. B **8**, 5747 (1973).

[28] R. A. Evarestov and V. P. Smirnov, Phys. Status Solidi b **119**, 9 (1983).

[29] G. P. Srivastava, J. Phys. A: Math. Gen. **17**, L317-L321 (1984).

Chapter 3

Experimental Techniques

3.1 Introduction

Since the 1980's several experimental techniques have been developed for surface studies. Experimental techniques for obtaining structural information can be divided in two main sections: (i) reconstruction pattern using Low Energy Electron Diffraction (LEED), Reflection High Energy Electron Diffraction (RHEED), Scanning Tunneling Microscope (STM) and (ii) atomic information using LEED, STM, X-ray Standing Wave (XSW) analysis, surface-extended absorption fine structure (SEXAFS), photoelectron diffraction (Ph D) and ion scattering. Surface electronic states can be mapped by photoemission spectroscopy (PS) and its derivatives: Ultraviolet PS (UPS), X-ray PS (XPS). The STM technique can also be used to investigate surface electron states. The dispersion of energy bands can be obtained using angle-resolved ultraviolet photoelectron spectroscopy (ARUPS) and the density of states can be measured using angle-integrated photoemission spectrum. The surface chemical compositions can be obtained by using Auger Electron Spectroscopy (AES) [1].

In this chapter the main experimental techniques referenced in later chapters are outlined. It is not possible within the remit of this thesis to examine the technicalities of each method and all experimental techniques in great detail, and we will therefore discuss the basics of a few experimental techniques along with their basic concepts.

3.2 Structural Measurements

The size and shape of a surface unit cell can be provided by using the LEED, RHEED, and STM patterns and intensities. If a crystal is cut along a certain plane, then the atoms near the surface may be disturbed from their equilibrium positions in the bulk. This leads to changes in the relative positions of the surface and near surface atoms (surface reconstruction). Such changes may be explored with these experimental techniques which are outlined below.

3.2.1 Low Energy Electron Diffraction (LEED)

Low energy electron diffraction (LEED) is one of the most powerful methods for the determination of surface structure [2, 3, 4, 5]. In the LEED technique, the electrons have a wavelength comparable with the internuclear spacings in crystals, i.e., the LEED electrons have very low penetration power. If one wants to resolve to interatomic spacings of about 1 Å, one needs the electron to have a kinetic energy of 150 eV ($\lambda = \frac{h}{mv} = \frac{h}{(2mE)^{1/2}}$). The electrons are coherently scattered by the lattice to produce a certain Bragg diffraction pattern (see Sec. 3.2.4). From the shape of the diffraction pattern, the 2-dimensional periodic structure of the crystal can be determined.

The LEED experimental setup is shown in Fig. 3.1 [2, 4]. The electron gun produces an electron beam which is accelerated by using an anode (or beam) voltage, V. The anode has a hole in it, allowing electrons to escape. The electrons enter from the grids. There is a retarding potential between the two hemispherical grids which allows the electrons pass to the grids. A fluorescent screen is held at a large positive potential so that the electrons accelerate and excite the screen which fluorescent upon impact. Then image of the diffraction spot pattern is recorded using the video camera. The technique is also sensitive enough to measure diffuse LEED intensity (i.e., using I(V) curves) distributions due to disordered surfaces. Such dynamical LEED studies have been applied to determine the structure of the systems: S/III-V(001) (1×1) [6] at low temperature and a (2×1) [7] as well as a (2×2) [8] reconstruction after annealing, Se/InP(110) (1×1) [9], H_2S/III-V(110)(1×1) [10, 11, 12, 13], the clean Si(001) surface c(4×2) at low temperature exhibits and (2×1) at high temperature [14], S on Si(001) [15].

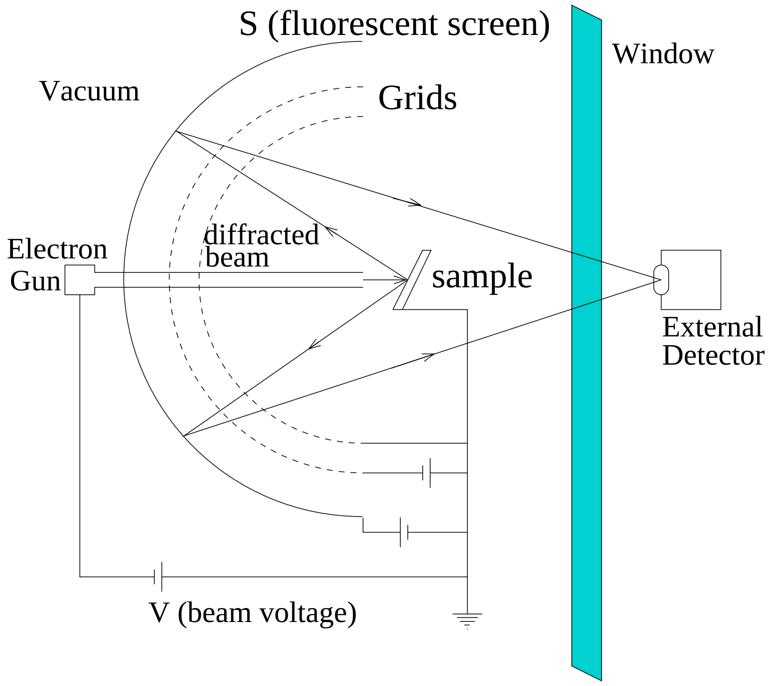

Figure 3.1: Schematic drawing of a LEED apparatus.

3.2.2 Reflection High Energy Electron Diffraction (RHEED)

Reflection high-energy electron diffraction (RHEED) is another important tool in surface science [2, 3, 4, 5]. It is highly surface-sensitive and is compatible with a wide range of other instruments and processes. It instantly provides structural information about a crystal surface. The RHEED technique has a number of similarities with LEED. In both methods the sample is struck by a collimated beam of electrons and a diffraction pattern observed on a fluorescent screen. In RHEED, however, the electrons have a much higher energy (3-100keV).

A high energy beam is directed at the sample surface at a grazing angle. The electrons are diffracted by the crystal structure of the sample and then impinged on a phosphor screen mounted opposite to the electron gun (compare with LEED). The resulting pattern is a series of streaks, rather than the spots associated with LEED experiments. The distance between the streaks indicates the surface lattice unit cell size. The grazing incidence angle ensures surface specificity despite the high energy of the incident electrons. If a surface is atomically flat, then sharp RHEED patterns are seen. If the surface has a rougher surface, the RHEED pattern is more diffuse. This behaviour can lead to RHEED oscillations as a material is evaporated onto a surface. RHEED is therefore of particular use with Molecular Beam Epitaxy (MBE). MBE is a method of laying down layers of materials with atomic thicknesses on to substrates. This is done by creating a molecular beam of a material which impinges on to the substrate in ultra-vacuum condition.

3.2.3 Scanning Tunneling Microscope (STM)

The scanning tunnelling microscope (STM) [16] is a well-developed tool for surface analysis. It is very powerful for surface studies because it can directly probe surface geometries, structures and electronic properties.

When an extremely sharp probe needle is very near the surface with an external field, the electrons from the sample surface will conduct through the probe needle by tunnelling between the probe needle and the sample surface. The size of this tunnel current is very sensitive to the tip sample separation. A small bias voltage between the tip and the sample induces a small current to flow even though the two conductors are separated. The current that flows arises from the overlap of the electron orbitals at the end of the tip and on the surface, and because of this, the electrons can tunnel across the vacuum barrier between the two. The current is proportional to this overlap of this electron orbitals. Because of the exponential dependence of the radial component of the wavefunction of electrons on atoms, the current drops exponentially as the tip withdraws from the surface. This extreme sensitivity to separation is exploited by subsequently scanning the tip across the surface, and using the current as a feedback signal. The tip-surface separation is controlled to be constant by keeping the tunnelling current at a constant value. The voltage necessary to keep the tip at a constant separation is used to produce a computer image of the surface. Under the best of conditions, the vertical noise floor can approach about a few times smaller than an atom. The lateral resolution depends upon the shape of the tip but it can often achieve 1 or 2 Å. More detailed uses of this techniques can be gained from Welland [17].

3.2.4 X-ray Standing Wave (XSW)

When an X-ray Bragg reflection is established in a crystal the incident and scattered waves maintain their phase coherence up to a long distance ($\sim$ 1000 Å) [18] and interfere to produce an X-ray standing wavefield in the crystal which has a periodicity in intensity equal to the periodicity of the associated scatterer planes of the crystal. It allows direct determination of the positions of adsorbed atoms relative to a selected subset of substrate planes. If one considers two waves incident at an angle θ on two parallel planes with separation $d_{12,\perp}$, as shown in Fig. 3.2, the wave reflected from the lower plane travels $2d_{12,\perp}\sin\theta$ further than the wave reflected from the upper plane. The reflected waves interfere constructively to produce a maximum in intensity if this distance is a multiple of the wavelength, so $2d_{12,\perp}\sin\theta=n\lambda$ for a scattering peak.

A multiple scattering formulation of the X-ray scattering under these conditions shows that the range in X-ray incidence angle or wavelength - over which the nominal total reflectivity of the Bragg condition is maintained is finite, and the standing wave thus exists throughout this range. However, a position of the nodal planes of the standing wave relative to the scatterer planes (i.e. the phase of the standing wave) shifts in a systematic and predictable fashion within this range by one half of the scatterer plane spacing. This can be used to locate specific atomic species within the solid by monitoring the X-ray absorption of these species as a function of scattering condition within the total reflectivity range. If the absorber lies on the nodal planes of the standing wave no adsorption is detected, whereas if they lie on the antinodes, enhanced absorption is found. In this way XSW can be used to locate specific atoms, relative to the bulk scatterer planes, not only within a crystal, but also at the surface of a crystal, because the standing wavefield extends far above the surface.

The intensity of the standing wave at a particular position can be changed by altering the reflection angle, or the photon energy. The intensity of an Auger (see AES) or fluorescence- peak from a molecule attached to the surface is then monitored. The variation of the intensity of the peak can provide information regarding the adsorption site and thus provides information complementary to SEXAFS and

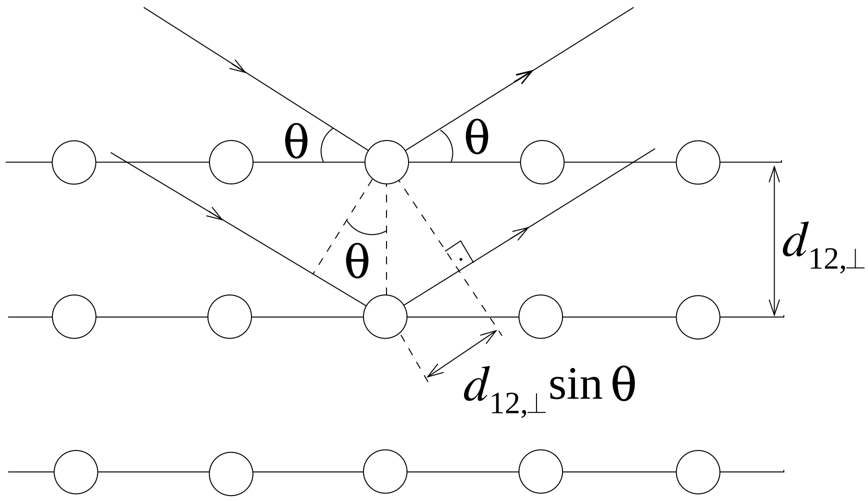

Figure 3.2: Simple presentation of the diffracted beams from a crystal.

XPD. XSW has the advantage of being able to work in non-UHV conditions and to investigate buried interfaces. Changing the photon energy means that a synchrotron radiation source is required. A key limitation of this general XSW method, however, is that under general conditions the angular range of the total reflectivity condition can be very narrow so the experiment is only possible on samples which have a very high degree of crystalline perfection.

3.3 Surface Chemical Compositions

3.3.1 Photoelectron Spectroscopy (PS)

One of the most widely used methods for studying the electronic properties of semiconductor surfaces and bulk semiconductors is Photoelectron Spectroscopy (PS) [19]. There are several different forms of photoelectron spectroscopy. The most common methods are known as ultra-violet photoelectron spectroscopy (UPS) and X-ray photoelectron spectroscopy (XPS). UPS uses ultraviolet light in the 5 to 100 eV range while XPS uses X-ray photons with energies well above 100 eV.

If one considers a single atom with just one x-ray photon incident, the total energy is $h\nu + E_i$, where $h\nu$ is the photon energy and E_i the energy of the atom in its initial state. Following the absorption of the photon and the emission of the

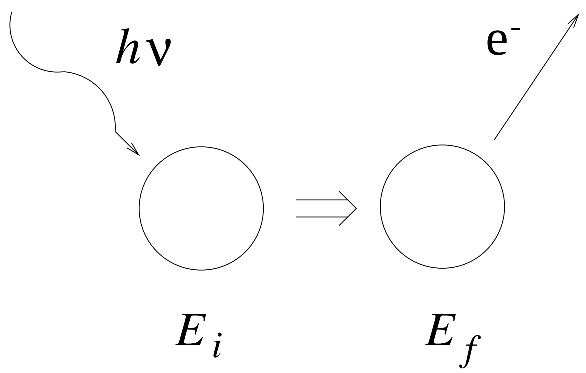

Figure 3.3: Simple presentation of absorption by a single atom of photon and emission of a photo electron.

photoelectron, the total energy is now $K + E_f$, where K is the kinetic energy of the electron and E_f the final state energy of the atom (now an ion). Because total energy is conserved $h\nu + E_i = K + E_f$ or $h\nu - K = E_f - E_i = E_B$.

The difference between the photon energy (i.e. it is given) and the electron energy (i.e. it is measured) is equal to the binding energy of the orbital from which the electron was expelled. The binding energy is determined by the difference between the total energies of the initial-state atom and the final-state ion. It is roughly equal to the Hartree-Fock energy of the electron orbital and so peaks in the photoelectron spectrum can be identified with specific atoms and hence, a surface compositional analysis performed. If XPS uses the highest photon energy, electrons which have the highest binding energies from the core levels can be excited. Then an energy diagram of a XPS experiment can be drawn.

3.3.2 Auger Electron Spectroscopy (AES)

Auger Electron Spectroscopy (AES or Auger) is a surface sensitive analytical technique. A focused beam of electrons is used to excite atoms on a solid surface, generating a core hole. The physical process is shown in Fig. 3.4. The hole can be filled by an outer electron and the extra energy can be released to another electron (an Auger electron) or an x-ray photon. If the target atom is very near the surface, the Auger electrons can escape from the solid. Their energy can then be measured and they can be counted to yield a spectrum of the number of electrons emitted

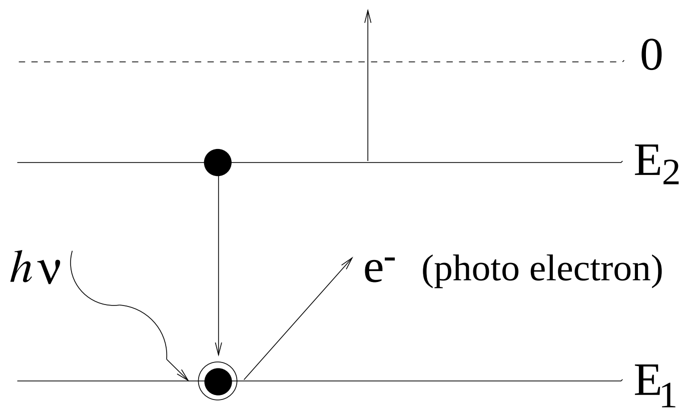

Figure 3.4: Schematic Auger Electron transition. At energy level E_1 the electrons are expelled by either an impinging electron or a photon, leaving a hole. An electron from E_2 may fall into the hole at E_1 and the energy thus released is absorbed by another electron which gets ejected from the solid. The second electron is called the Auger electron.

as a function of energy. Elemental identification is made from the energy positions of the Auger peaks. In some circumstances, it is also possible to derive chemical information from the peak position and the peak shape. The intensity of an Auger peak can be related to the amount of that element present in the analysed volume by applying appropriate sensitivity corrections.

Elemental composition information (and some chemical information) is also obtained from the top two to five atomic layers using AES techniques. An ion etch gun is used to rapidly "depth profile" through layers to provide a continuous plot of composition with depth. For example, the composition and thickness of layers in a complex thin-film structure can be evaluated using this technique.

3.4 Summary

I have briefly discussed a few surface science experimental techniques that involve the use of electrons and photons. These techniques yield very detailed information about geometrical structures and electronic states of semiconductor surfaces. I will give some of these experimental results on clean and adsorbate covered semiconductor surfaces in the forthcoming chapters which have been carried out by experimentists using some of the powerful experimental techniques listed above.

Bibliography

[1] C. B. Duke, *Surface Science: The first thirty years*, Amsterdam; North-Holland, reprinted from Surf. Sci. **299/300**, 1994.

[2] A. Zangwill, *Physics at Surfaces*, Cambridge University Press, 1988.

[3] G. Burns, *Solid State Physics*, International Edition, Acedemic Press, 1990.

[4] M.-F. Li, *Modern Semiconductor Quantum Physics*, World Scientific Publishing, 1994.

[5] P. Y. Yu and M. Cardona, *Fundamentals of Semiconductors*, Springer-Verlag Berlin Heidelberg, 1996.

[6] Y. Tao, A. Yelon, E. Sacher, Z. H. Lu, and M. J. Graham, Appl. Phys. Lett. **60**, 2669 (1992).

[7] H. Oigawa, J. F. Fan, Y. Nannichi, H. Sugahara, and M. Oshima, Jpn. J. Appl. Phys. **30**, L332 (1991).

[8] J.-M Jin, M. W. C. Dharma-wardana, D. J. Lockwood, G. C. Aers, Z. H. Lu, and L. J. Lewis, Phys. Rev. Lett. **75**, 878 (1995).

[9] T. Schröter, A. Chassé, I. Eckardt, K. Tiedge, N. Wagner, D.R.T. Zahn, C.Nowak, A. Hempelmann, and W. Richter, Surf. Sci. **307-309**, 650 (1994).

[10] E. Dudzik, R. Whittle, C. Müller, I. T. McGovern, C. Nowak, A. Märkl, A. Hempelmann, D. R. T. Zahn, A. Cafolla, W. Braun, Surf. Sci. **307**, 223 (1994).

[11] E. Dudzik, C. Müller, I. T. McGovern, D. R. Lloyd, A. Patchett, D. R. T. Zahn, T. Johal, and R. McGrath, Surf. Sci. **344**, 1 (1995).

[12] E. Dudzik, A. Leslie, E. O'Toole, I. T. McGovern, A. Patchett, D. R. T. Zahn, J. Ludecke, D. P. Woodruff and B. C. C. Cowie, J. Phys.: Condens. Matter **8**, 15 (1996).

[13] E. Dudzik, A. Leslie, E. O'Toole, I. T. McGovern, A. Patchett, and D. R. T. Zahn, Appl. Sur. Sci. **104/105**, 101 (1996).

[14] B. W. Holland, C. B. Duke, and A. Paton, Surf. Sci. **140**, L269 (1984).

[15] A. Papageorgopoulos, A. Corner. M. Kamaratos, and C. A. Papageorgopoulos, Phys. Rev. B **55**, 4435 (1997).

[16] G. Binning, H. Rohrer, C. Berber and E. Weibel, Phys. Rev. Lett. **49** 57 (1982).

[17] M. Welland, Physics World **7**, 32 (1994).

[18] P. L. Cowan, J. A. Golovchenko, and M. F. Robbins, Phys. Rev.Lett. **44**, 1680 (1980).

[19] R. H. Williams, G. P. Srivastava and I. T. McGovern, Rep. Prog. Phys. **43**, 1357 (1980).

Chapter 4

S-covered InP(110) surface

4.1 Introduction

The sulphur treatment of III-V(001) has been achieved by a variety of methods, leading to a (1×1) low-energy electron diffraction (LEED) pattern at room temperature [1] and a (2×1) [2] as well as a (2×2) [3] reconstruction after annealing. Whereas the (1×1) structure is metallic [4, 5], the (2×2) reconstruction is found to be semiconducting.

The effect of sulphur treatment of the nonpolar III-V(110) surface should be considered differently, due to the presence of both cations and anions on the surface layer. The stoichiometry of the cleavage III-V(110) surface is well known and easily reproducible, and its atomic structure is very well understood [6]. Room temperature in-situ adsorption of S on InP(110) has been found to result in a less than perfect overlayer [7]. Annealing to around 270°C indicates a high degree of order and a single adsorption site, with the S atoms at a vertical height of 1.95 $\pm$ 0.02 Å from the surface [7]. While a (1×1) LEED pattern has been observed for Se adsorption [8], core level photoemission data [8] indicate an ordered Se reacted layer. For example, by observing chemical shifts in spectra, Schröter *et al* [8] have concluded that an exchange reaction between the adsorbate and the substrate anion may take place at elevated annealing temperatures. In particular, by examining the binding energy difference between Ga 3d and Se 3d components, Schröter *et al* [8] have suggested the existance of Ga_2Se_3-like bonds, consistent with the electron counting rule and suggesting the formation of an ordered layer. Due to the reactive nature of these adsorbates, the understanding of the actual interface formation, atomic geometry and electronic properties of (S,Se)/III-V(110) systems has not been conclusive. For S/InP(110), Johal *et al.* [7] considered a number of different geometries, including epitaxially continued layer structure (ECLS), interchain bridging structure, modified epitaxial on-top structure exit (EOTS) with bonding only to In and the so-called 'defect' model (see Sect. 4.3 for a discussion of these structures). From an analysis of their work they suggest that the defect model is the most likely geometry, with the In-S-In bond angle close to the bulk tetrahedral bond angle.

The aim of this chapter is to study S-depositied on InP(110) surfaces with *ab initio* pseudopotential method. We theoretically investigate the atomic geometry, electronic states, and chemical bonding for the clean InP(110) and S covered InP(110) surfaces. For the clean InP(110) surface, we use a reconstruction which has been determined by the x-ray standing wave (XSW) technique through detection of surface-sensetive Auger electrons [9]. For the S-deposited InP(110) surface, both ordered non-reacted and reacted geometrical models are considered. It is found that for a half-monolayer non-reacted coverage the S atom resides in the interchain bridge position, while for a full-monolayer non-reacted coverage the epitaxially continued layer structure results in a good semiconducting nature. For reacted surface structures, it is found that the model involving exchange between S and P atoms results in good agreement for the interlayer distance with the XSW analysis by Johal *et al.* [7], but leads to a small band gap between the occupied and unoccupied surface states.

4.2 The clean (110) surface

4.2.1 Projected Bulk Band Structure

In order to provide a basis for discussion of the surface results obtained by the method described in the Theory chapter, it is necessary to compare the results with a projected bulk band structure calculated by comparable methods. The projected bulk band structures presented in Fig. 4.1 are the results of EKSETER code calculations performed at the same energy cutoffs for plane wave basis and using the same pseudopotential as the supercell calculations with which they are to be compared. In principle it is possible to obtain a projected bulk band structure by performing a straightforward bulk calculation and then mapping points within the standard zincblende Brillouin zone (see Fig. 4.1). The surface Brillouin zone is the Wigner-Seitz area obtained from perpendicular bisection of the primitive reciprocal lattice vectors ($\mathbf{b_1}$ and $\mathbf{b_2}$) from a chosen surface reciprocal lattice point. The irreducible segment of the surface Brillouin zone and high symmetry points are shown in Fig. 2.3(a).

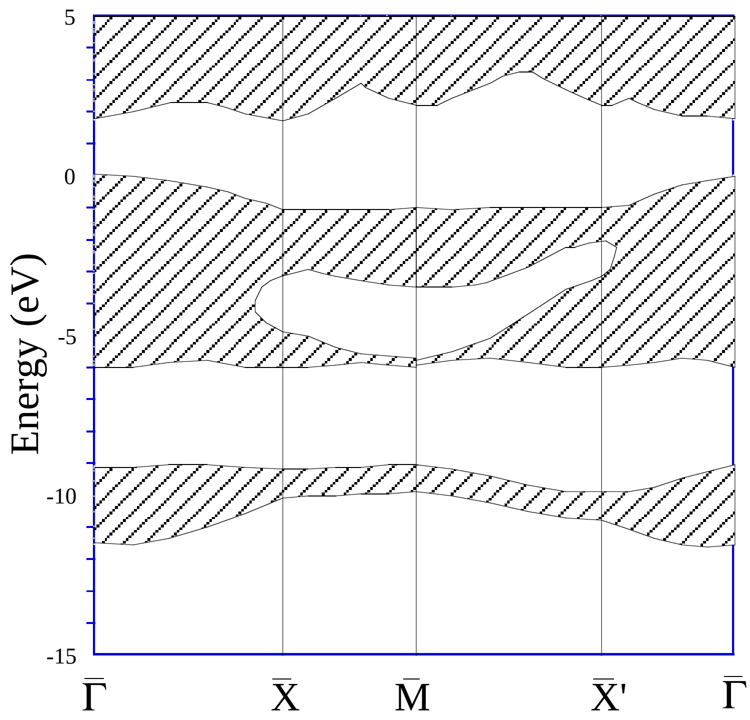

Figure 4.1: Projected bulk spectrum is shown by hatched regions.

4.2.2 The III-V(110) surface

The cleaved (110) surface of zinc-blende materials retains its primitive (1×1) periodicity. Fig. 4.2 shows the surface primitive cell on a zinc-blende-structure crystal terminated on the (110) surface with a (1×1) lattice pattern. There are two atoms (one cation and one anion) in every layer of the (110) unit cell. The real-space lattice vectors and the surface Brillouin zone for the (110) surface in the (1×1) pattern were given in chapter 2.

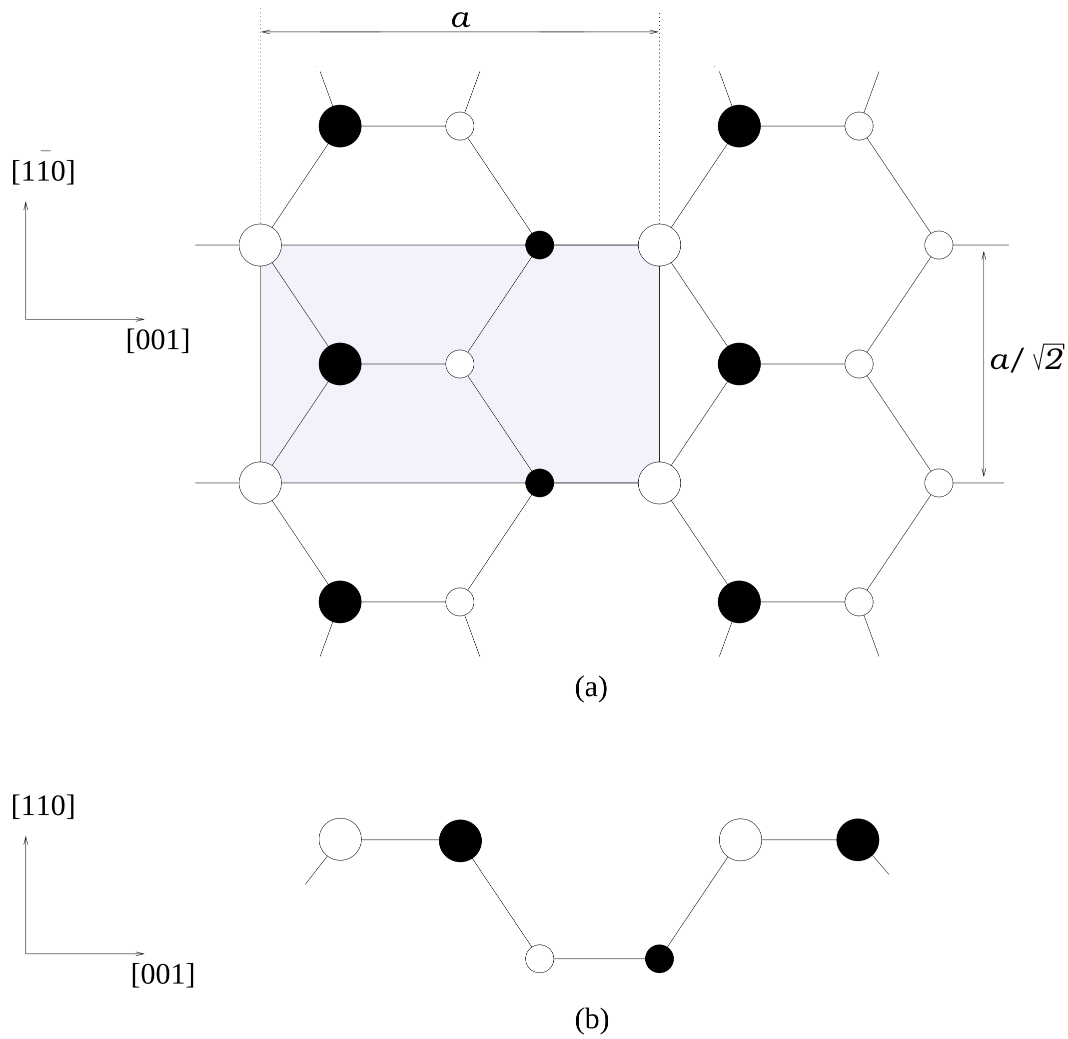

Figure 4.2: Schematic (a) top and (b) side views of the surface geometry of the III-V(110) surface.

The relaxation of III-V(110) surfaces is characterized by an inward relaxation of the group-III surface atoms, while the group-V first-layer atoms are shifted above the surface. The driving mechanism of this atomic rearrangement is the desire for a p-bonding configuration of anion surface atoms with their group-III neighbours. Similarly, the first layer cations prefer to be situated in a more sp^2-like bonding configuration with their group-V neighbours [10]. This leads to a nearly bond-length conserving rotation of the surface chains by a tilt angle ω of about 27^o-32^o

depending on the particular compound as shown in Fig. 4.3. The vertical buckling of the top layer, $\Delta_{1,\perp}$, ranges from 0.61 Å to 0.75 Å [11, 12]. Both ω and $\Delta_{1,\perp}$ are the main characteristic parameters for the III-V(110) semiconductors and they depend linearly on each other.

It is important to appreciate error margin in calculated and experimetally determined surface parameters. The structural parameters calculated in this thesis, for clean and covered surfaces, have an error margin of 0.05 Å. The error margin in structural determination using various experimental techniques can be upto 0.15 Å.

4.2.3 Atomic geometry, electronic states and chemical bondings for the clean InP(110) surface

Our calculated equilibrium lattice constant for bulk InP is 5.67 Å. This value was used in performing the surface calculations even though it is 3.4% smaller than experimental value [13]. This difference generally results for the LDA calculations. For geometry optimization plane waves were considered up to the kinetic energy cut-off of 8 Ry and up to 12 Ry for band calculations. Self-consistent solutions to the Kohn-Sham equations were obtained by employing a set of four special **k**-points. The cut-off was found to be adequate for structural studies. For geometry optimization, we have calculated the vertical buckling distance $\Delta_{1,\perp}$ for 8 Ry and 12 Ry. The results are consistent within 1%. The calculated structural parameters for this system is presented Tab. 4.1 together with available relevant theoretical and experimental data. The calculated eqilibrium geometry is close to the previously proposed values [12, 14, 15]. As shown in Fig. 4.3, and mentioned earlier, the surface P (In) atoms have relaxed outwards (inwards).

Figure 4.4 shows the calculated surface electronic states for the clean InP(110) surface system. Also shown are the experimentally derived data from photoemission studies on InP(110) [16]. A total of six occupied electronic states have been identified and one unoccupied electronic state, as shown in Fig. 4.4. The states, S_1 (s-like), S_4 (p_x-like), S_5 and S_6 (p_z-like) are derived from the anion (P) atoms and the other states, S_2(s-like), S_3(s-like) and S_7 (sp_z-like), are derived from the cation

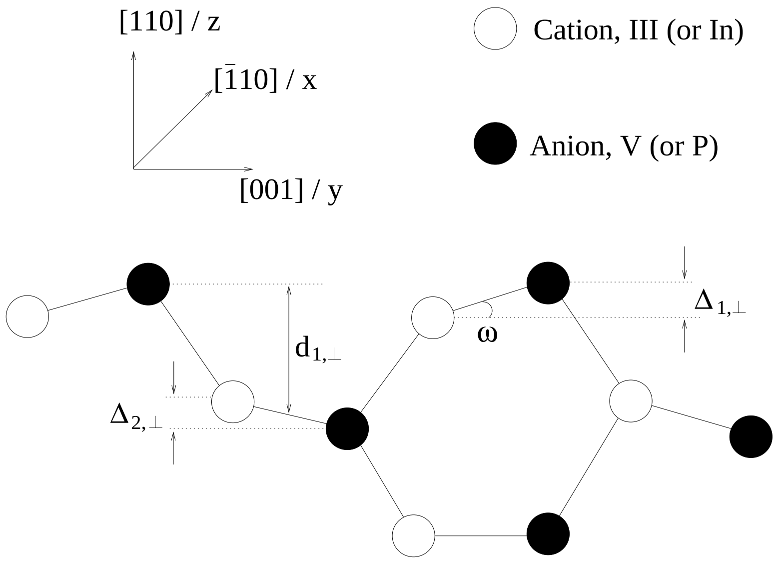

Figure 4.3: Schematic side view of the relaxed surface geometry of the InP(110) surface. The relaxation parameters refer to Tab. 4.1.

	Present	Alves *et al.*[12]	Duke *et al.*[14]	Fritsch *et al.*[15]
$d_{12,\perp}$	1.435	1.511	1.549	1.548
$\Delta_{1,\perp}$	0.670	0.600	0.730	0.636
$\Delta_{2,\perp}$	0.117	0.079	0.140	0.106
ω	30.1	27.1	29.9	27.5

Table 4.1: Structural parameters of the InP(110) surface. These parameters are indicated in Fig. 4.3. Distances are in Å and angles in degrees.

(In) atoms (directions define in Fig. 4.3). The orbital characters of these states have been discussed in many previous works [12, 17]. The unoccupied surface energy level, S_7, is found to lie at an energy 1.5 eV above the bulk valence band edge at $\bar{X}$.

4.3 The S-deposited InP(110) surfaces

The geometry of the S/InP(110)-(1 × 1) interface was modelled by considering the following structures: For a full-monolayer coverage with non-reacted interface, we considered the epitaxially continued layer structure (ECLS) in which the adatoms

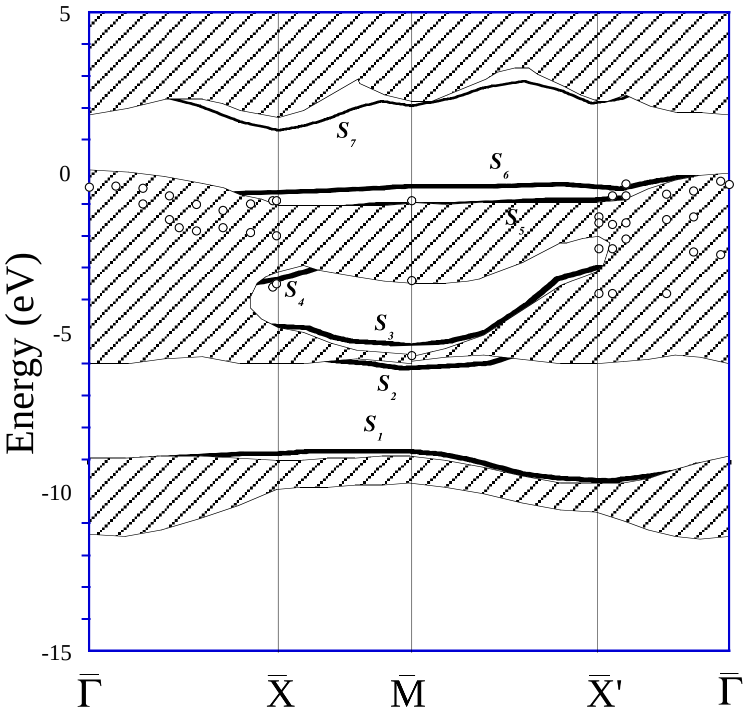

Figure 4.4: Electronic band structure of the clean InP(110) surface. Projected bulk spectrum is shown by hatched regions. Occupied and unoccupied surface states are shown by thick and thin curves, respectively. The angle-resolved photoemission results are indicated by open circles [16].

position are located closely to sites that the next substrate layer would have otherwise occupied (see Fig. 4.5(a)), the epitaxial on top structure (EOTS) which the adatoms position lie more or less vertically above the top layer substrate atoms (see Fig. 4.5(b), and a S-S dimer attached to surface P atoms as suggested by Schmidt *et al.* [18] (see Fig. 4.5(c)). For a half-monolayer coverage, the interchain bridging geometry (see Fig. 4.5(d)), the modified epitaxial on top structure with bonding of S only to In or P (see Fig. 4.5(e)), and the epitaxially continued layer structure with bonding of S only to In or P (or the so-called 'defect' model) [7] were considered (see Fig. 4.5(f)). For reacted interface, a model involving S diffusion, an exchange model, and a model containing S substitution and S adatom were considered as shown in Fig. 4.6.

For geometry optimization, plane waves were considered up to the kinetic energy cut-off of 8 Ry. Self-consistent solutions to the Kohn-Sham equations were obtained by employing a set of four special **k**-points. The cut-off was found to be adequate

	$d_{12,\perp}$	$\Delta_{1,\perp}$	$\Delta_{1,y}$	$\Delta_{2,\perp}$	$\Delta_{2,y}$	ω_1	ω_2
ECLS	1.73	0.55	1.42	0.09	1.38	21.17	-3.73
Bridging	0.95	–	–	0.005	1.79	–	0.16
Exchange	1.98	0.68	1.20	0.37	1.28	29.54	-16.12
Diffuse	2.21	0.70	1.56	0.19	1.44	-24.17	-7.52
XSW.[7]	1.95 ±0.02 Å	–	–	–	–	–	–

Table 4.2: Structural parameters of the ECLS, the interchain bridging, exchange-reacted and diffuse-reacted for S-deposited to the InP(110) surface. These parameters are indicated in Figs. 4.7 and 4.14. Distances are in Å and angles in degrees.

for structural studies: increasing the cut-off to 12 Ry resulted in a change of less than 1% for the average vertical distance between S atoms and the InP(110) surface for one of the structural models considered in the next section. However, a cut-off of 12 Ry was used to obtain well converged band structure results. The results for atomic geometries and band structures are described below and compared with existing experimental results. The calculated equilibrium atomic geometries for four energetically favourable structures are given Tab. 4.2.

4.3.1 Non-reacted surface structures

4.3.1.1 Full monolayer coverage

For 1 ML coverage, three different geometrical models for the non-reacted interface were considered: the ECLS, EOTS, and S-S dimer at the P site as shown in Figs. 4.5(a) to (c). From total energy calculations, it was found that the ECLS is the favoured geometry. Compared to the ECLS geometry, the EOTS and S-S dimer geometries lie at 0.26 eV and 0.78 eV per S atom, respectively. We thus investigated the ECLS geometry in more detail.

The relaxed ECLS geometry is shown in Fig. 4.7. It is found that the S overlayer is characterised by a vertical buckling of 0.55 Å and a tilt of 21.2°. The d(In-S) and d(P-S) bond lengths are 2.37 Å and 2.39 Å, respectively. The d(In-S) bond length is 4.4% smaller than the sum of corresponding covalent radii [19], but the d(P-S) bond length is 11.7% larger than the sum of corresponding covalent

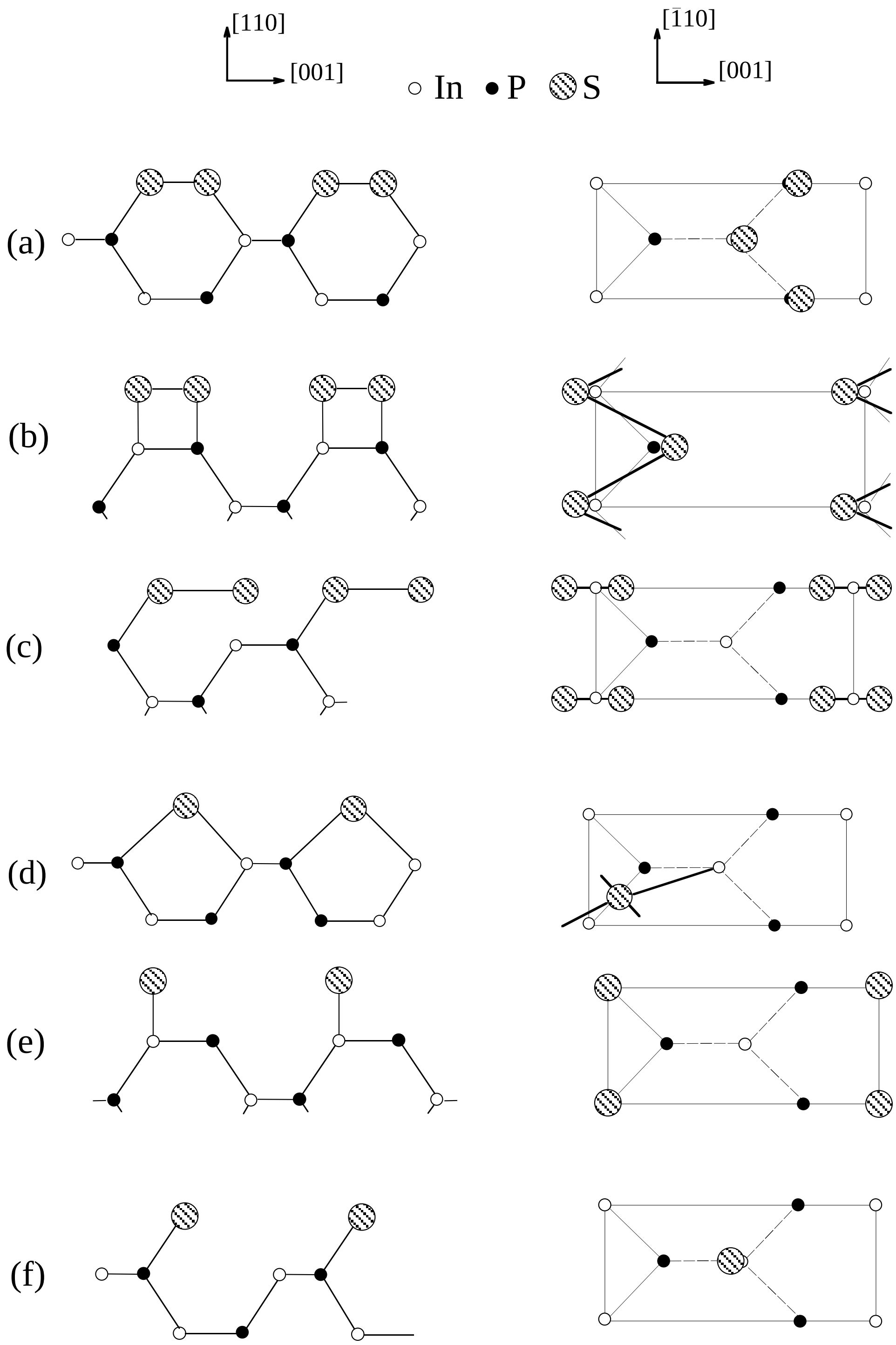

Figure 4.5: Schematic side views and top views of surface geometries for non-reacted S overlayers on InP(110). (a), (b) and (c) show the ECLS, EOTS, and S-dimer at the P-site, respectively for 1 ML coverage. (d), (e) and (f) show the interchain bridging structure, modified epitaxial on-top structure with bonding only to In, and epitaxially continued layer structure with bonding only to In (the so-called 'defect' model), respectively for 1/2 ML coverage.

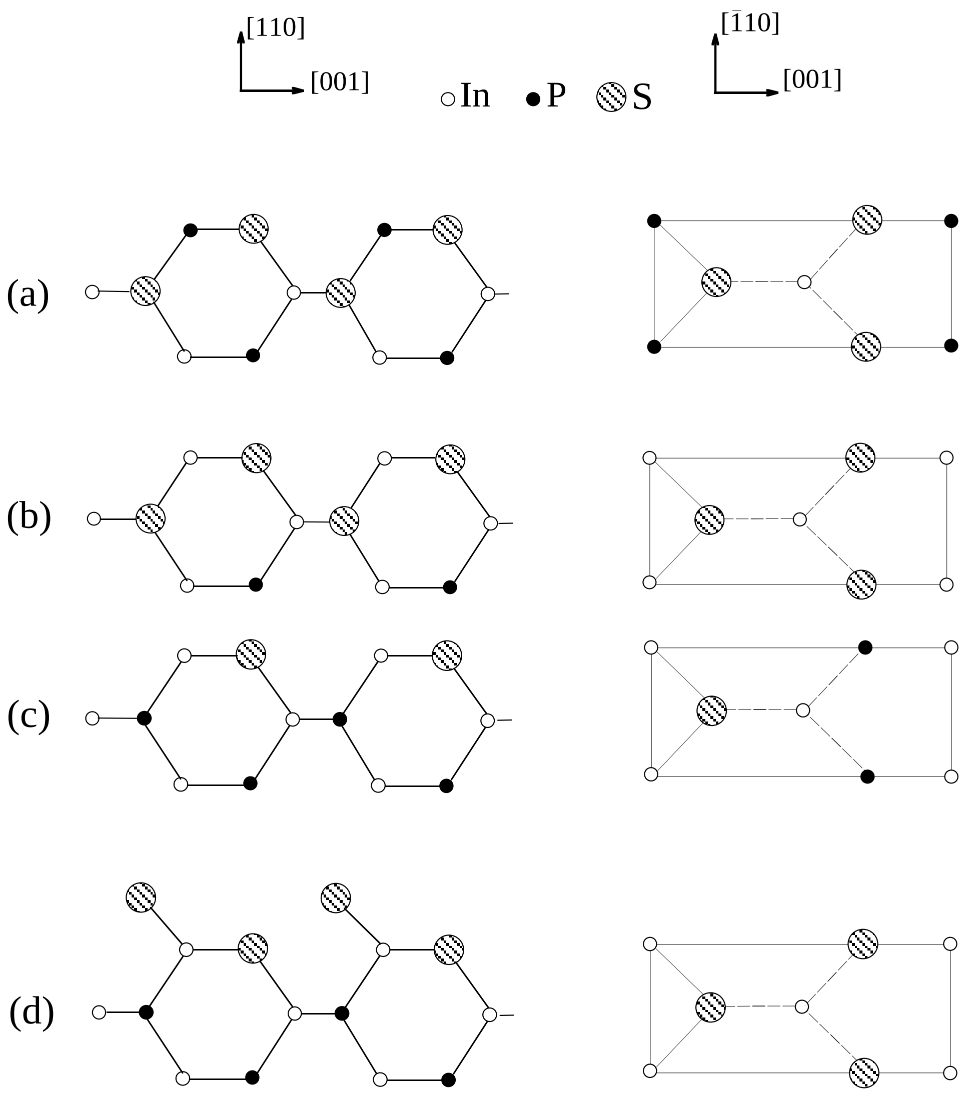

Figure 4.6: Schematic side views and top views of surface geometries for reacted S overlayers on InP(110): (a) and (b) are the exchange-reacted and the diffused-reacted, (c) and (d) are the substitution and substitution-adatom model, respectively.

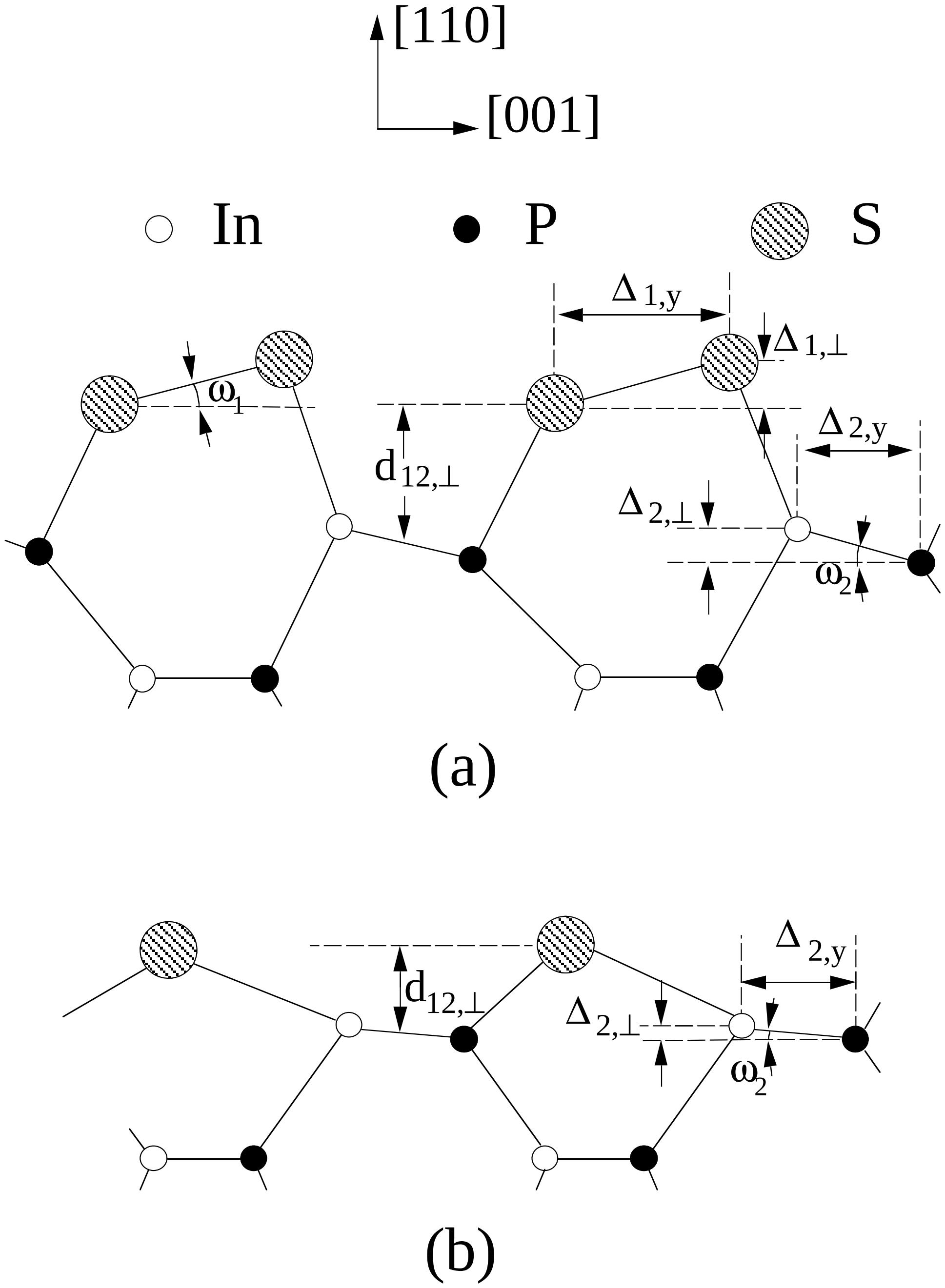

Figure 4.7: Schematic detailed side view of relaxed atomic geometries for the InP(110)/S for (a) the ECLS, (b) the interchain bridging.

radii [19]. The expanded bond length d(P-S) is also reflected in the P-S bond being weaker than the In-S bond, as seen in the total charge density displayed in Figs. 4.9(a) and (b). However, while the In-S bond is more ionic, the P-S bond is more covalent. The calculated value of 2.46 Å for the bond length d(S-S) is approximately 18% larger than twice the tetrahedral radius for S [19]. The one-dimensional charge density plot in Fig. 4.10 clearly indicates that the S-S bonding is covalent. The double humped feature of this covalent bonding is consistent with the expanded bond length d(S-S). The slight difference in the heights of the two peaks in Fig. 4.10 indicates bonding inequivalence of the two S atoms in the ECLS geometry. The calculated average interplanar distance $d_{12,\perp}$ between the S overlayer and the surface InP layer is 1.73 Å which is considerably shorter than the value 1.95 ± 0.02 Å reported by Johal *et al.* [7] from their x-ray standing wave (XSW) analysis. This large discrepancy of approximately 11% between theory and experiment is not due to the theoretical underestimation of 3.4% for the bulk lattice constant of InP. We think that the work by Johal *et al.* is incomplete and inconclusive, and that further experimental work is needed for comparison with our theoretical predictions.

It is interesting to compare the adsorption on III-V(110) of group -V elements, such as Sb and Bi, with the adsorption of the group -VI element such as S within the ECLS model. First, theoretical studies similar to the present one have revealed (see [20, 17]), in agreement with experiments, that for group-V overlayer the adsorbate-adsorbate bond length d(V-V) is within 3% of twice the corresponding tetrahedral radius, and the bonding between the overlayer atoms is largely covalent [20]. For the adsorption of S, on the other hand, the adsorbate-adsorbate bond length is much larger than twice the tetrahedral radius, and the bond has a very ionic character of the bond. Secondly, while the vertical distance between group -V overlayer and the substrate is in very good agreement with values obtained from LEED and XSW analyses [17, 20], the calculated value of this distance for the S overlayer is much shorter than the result analysed by XSW [7]. For the ECLS geometry, a total of seven occupied states and the lowest unoccupied electronic state has been identified, as shown in Fig. 4.8. While some of these are localized at the interface for all values of **k** on the surface Brillouin zone, others are localized at the interface only around the zone edges $\bar{X}$, $\bar{M}$ and $\bar{X}'$.

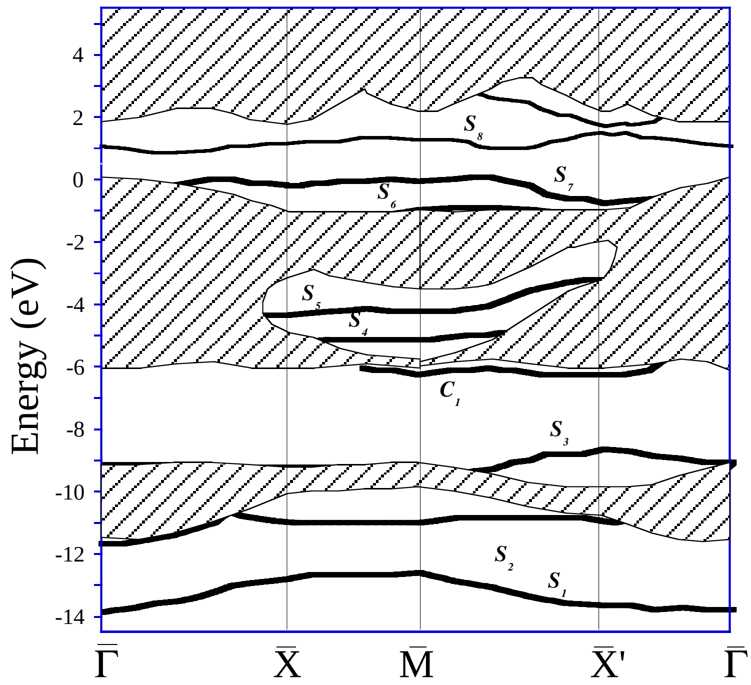

Figure 4.8: Electronic band structure of the InP(110)-S interface: for the 1 ML ECLS geometry. Projected bulk spectrum is shown by hatched regions. Occupied and unoccupied surface states are shown by thick and thin curves, respectively.

The occupied states S_1 and S_2 lie below the bulk valence band, and S_3 lies in the ionic gap. The states S_1 and S_3 are due to the bonding and antibonding between the s-orbitals from surface P and the lower lying overlayer S, respectively. The state S_2 is due to the s-orbital of the upper lying S atoms. The state C_1 skirts the upper edge of the ionic gap and is localized on the surface In atoms. A similar state is observed on the clean InP(110) surface (previous section), localized on the In atoms in the sub-surface layer [20]. In the present case the top InP layer acts as the second layer of the covered system. The state S_4 is a combination of surface P dangling bond orbital and the p_y-orbital of the lower lying S. The state S_5 is mainly due to the p_y-orbital of the upper lying S atoms. S_6 is largely contributed by the dangling bond orbital of the lower lying S atoms. The highest occupied state, S_7, is made of the dangling bond (sp^3) orbital of the surface P atoms and an sp_z-like orbital of the lower lying S atoms. The lowest unoccupied state, S_8, is due to the dangling bond orbital of the upper lying S atoms. The orbital natures of the states S_7 and S_8 are shown in Figs. 4.11(a) and (b), respectively. There is a minimum band gap

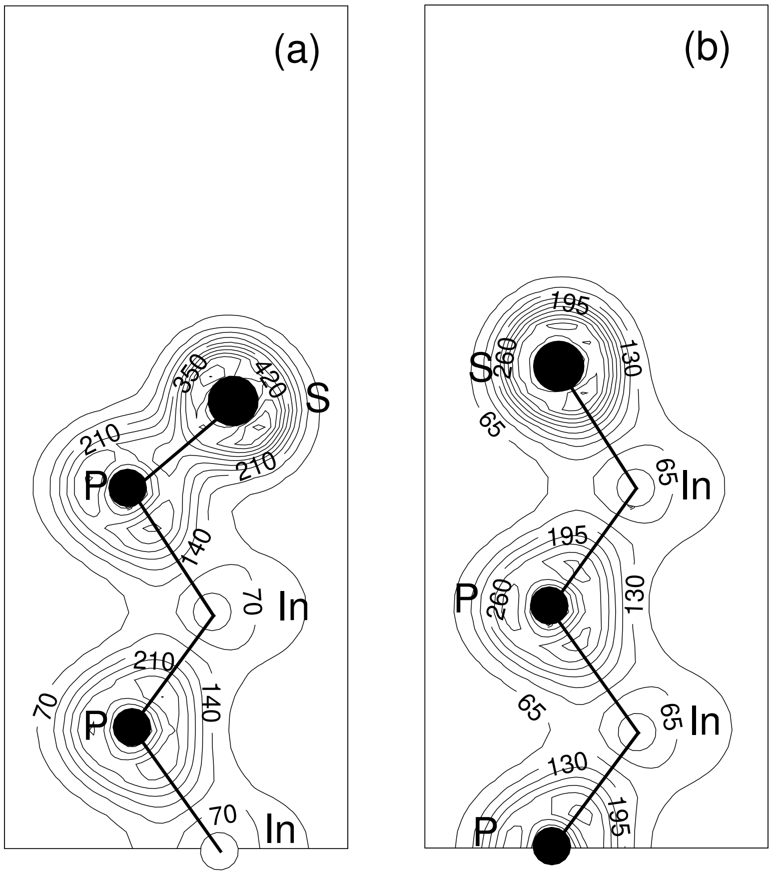

Figure 4.9: Electronic total charge density plots for the ECLS in (a) a vertical plane containing the P-S bond, (b) in a vertical plane containing the In-S bond. The charge density values are normalised to 80 electrons per unit cell volume of 631.26 Å^3.

(the local-density approximation result at the theoretical lattice constant) of about 1 eV between the S_7 and S_8 states along the $\bar{\Gamma}$-$\bar{X}$ direction.

4.3.1.2 Half monolayer coverage

Five geometries for the non-reacted 1/2 ML coverage were considered: interchain bridge, modified EOTS with S bonded to In, modified EOTS with S bonded to P, modified ECLS with S bonded to In (the 'defect' model considered in the work of Johal *et al.*), and modified ECLS with S bonded to P. It is found that the interchain bridging geometry (the relaxed geometry is shown in Fig. 4.7(b)) has the lowest total energy. For the relaxed interchain bridging geometry, the d(In-S) and d(P-S) bond lengths are 2.67 Å and 2.21 Å, respectively, which are bigger than the

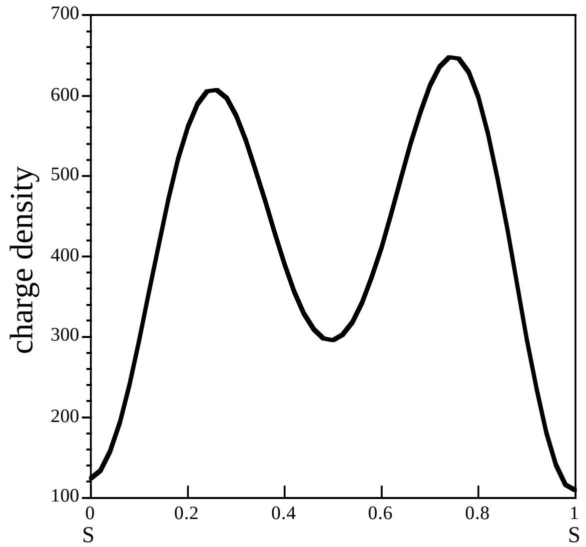

Figure 4.10: Electronic total charge density plots for the ECLS in along the line joining the two S atoms. The charge density values are normalised to 80 electrons per unit cell volume of 631.26 Å^3.

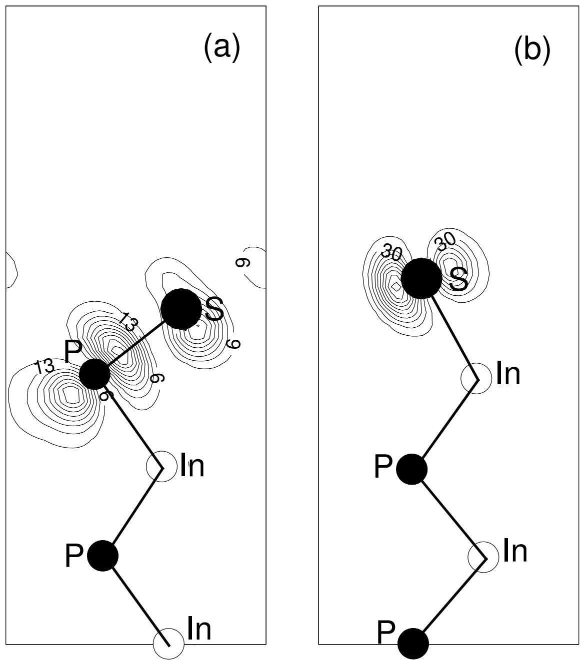

Figure 4.11: Electronic charge density plots for the highest occupied (a) and lowest unoccupied (b) states at the InP(110)-S (1 ML ECLS) interface at $\bar{M}$. The contour values are normalised to 2 electrons per unit cell volume of 631.26 Å^3.

sum of the corresponding covalent radii [19], thus characterizing the partially ionic characters of the In-S and P-S bonds. For this coverage of S, the substrate InP layer is de-relaxed: there is only a small vertical buckling of 0.04 Å between the In and P atoms. The S atoms are at a vertical distance of 0.95 Å from the surface. This calculated value does not agree with the value of 1.95 ± 0.02 Å measured in the work of Johal *et al.* It is interesting to note that, compared to the ECLS geometry, for 1/2 ML coverage the P-S bond length is reduced and the In-S bond length is increased. The general trend in our geometrical results for 1/2 ML coverage of S on InP(110) is very similar to that obtained by Schmidt *et al.* [18] for Se/GaAs(110).

The surface band structure for the interchain bridging geometry is given in Fig. 4.12. A total of seven occupied surface states has been identified. This geometry leads to a semi-metallic band structure. Fig. 4.13 shows the total charge density along the S-P and S-In bonds. Whereas the In-S bond shows a characteristic III-V bond charge distribution, the S-P bond shows a double humped covalent structure with peaks at around 30% of distance from both S and P atoms, with the higher peak lying towards S due to its larger electronegativity.

The other four geometries lie at much higher total energies than the interchain bridging geometry. However, the two modified EOTS geometries are characterized by much larger vertical distance between S and the surface layer: 2.4 Å with S bonded to In and 2.1 Å with S bonded to P. The two modified ECLS geometries are characterized by relatively smaller vertical separation between S and the surface: 1.7 Å with S bonded to In and 1.3 Å with S bonded to P. Thus while the calculated vertical distance of 1.7 Å for the 'defect' model is in reasonable agreement with the work of Johal *et al.*, it is discarded on energy grounds.

4.3.2 Reacted surface structures

Johal *et al.* [7] have observed a (1×1) LEED pattern for the S/InP(110) system for both room temperature in-situ adsorption as well as after annealing to 270°C. These authors have also reported that the coherent fraction of the adsorbate atoms for the S/InP(110) system at room temperature is low in comparison to a highly ordered S overlayer, indicating multiple sites for S adsorption. Annealing of the sample

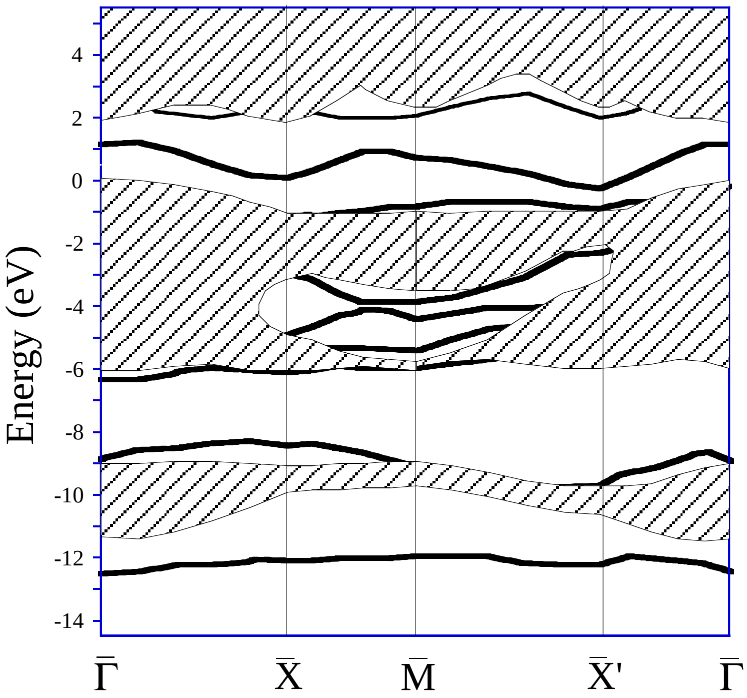

Figure 4.12: Electronic band structure of the InP(110)-S interface: for the 1/2 ML interchain bridging geometry. Projected bulk spectrum is shown by hatched regions. Occupied and unoccupied surface states are shown by thick and thin curves, respectively.

was found to result in an increase in the coherent fraction with no change in the coherent position (i.e. they are two parameters which totally define the structural dependence of the measured absorption profile [21]). Therefore, annealing may cause an exchange reaction to occur between S atoms and P atoms in the first atomic layers. In addition, core level photoemission studies [8] for Se/InP(110) were interpreted to indicate the existence of at least two distinct bonding sites for Se upon annealing. The authors thus advocated an ordered Se reacted layer. Since Se and S adsorbates are similar, both being group -VI elements, a few ordered reacted structural models for S/InP(110) has been considered. A discussion of atomic geometry, bonding and electronic structure for these models is given below.

4.3.2.1 Exchange Model

Starting with the ECLS geometry, a model in which one S atom is exchanged with one P atom on the S/InP(110) surface has been considered. The relaxed geometry

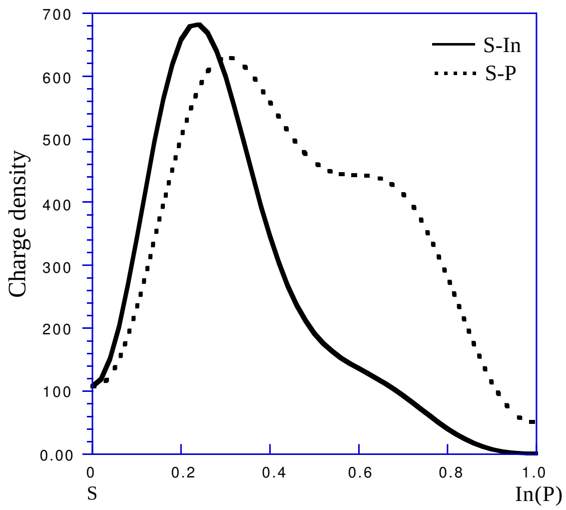

Figure 4.13: Total charge density along the S-In and S-P bonds for the 1/2 ML interchain bridging geometry, with normalisation of 76 electrons per unit cell volume of 631.26 Å^3.

is shown in Fig. 4.14(a). Our calculations indicate that compared to the ECLS geometry, there is an enegy gain of nearly 0.7 eV per S $\leftrightarrow$ P exchange between the top two layers. There are now two P-S and two In-S bonds. The bond length between P and S (top layer) is 2.43 Å and between P and S (second layer) is 2.84 Å. On the top layer there is now a chain formed by P and S atoms, and the chain angle P-S-P is 110.8°, close to the tetrahedral value. This can be contrasted with the chain angle for a monolayer of group-V overlayer (such as Sb) on III-V(110), which is approximately 90° [22]. The angle P-S(second layer)-In is about 97°. The bond length between In and S (top layer) is 2.33 Å and between In and S (second layer) is 2.40 Å. Thus, whereas the average In-S bond length remains the same as for the ECLS (non-reacted) model, the average P-S bond length is much larger than its value for the ECLS model. There is a vertical buckling of 0.68 Å between the top layer atoms P and S, and of 0.37 Å between the second layer atoms In and S. The average vertical distance between the top layer and the second layer is 1.98 Å, a value very close to the experimental result of 1.95 $\pm$ 0.02 Å obtained by Johal *et al.*

Figs. 4.16(a) and (b) show the total charge density plots for the exchange reacted model. The bonding between the second-layer In and the top-layer S remains covalent-ionic (Fig. 4.16(b)) as in the ECLS geometry. Figs. 4.16(a) and 4.17 show

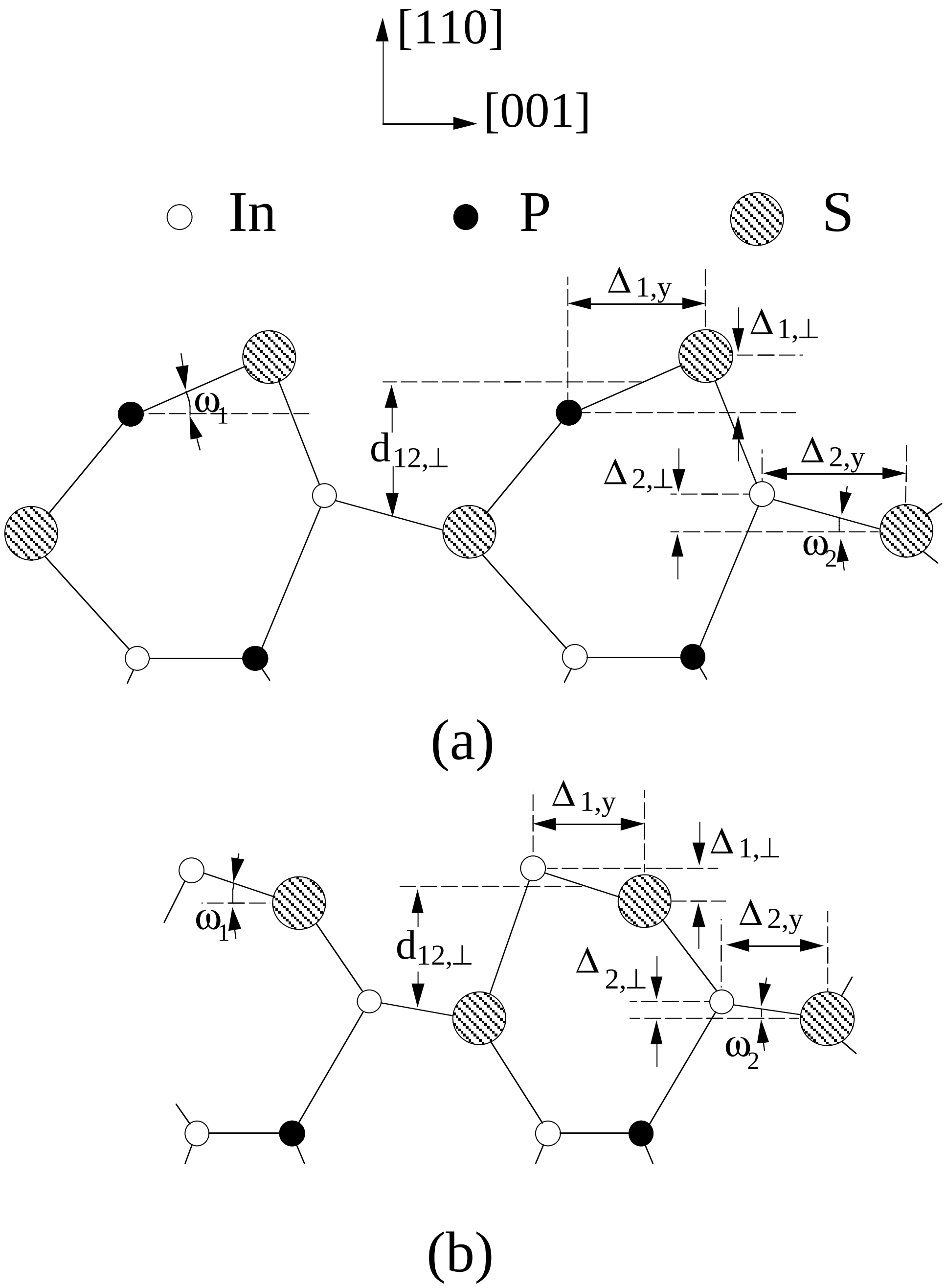

Figure 4.14: Schematic detailed side view of relaxed atomic geometries for the InP(110)/S for (a) exchange-reacted and (b) diffuse-reacted models.

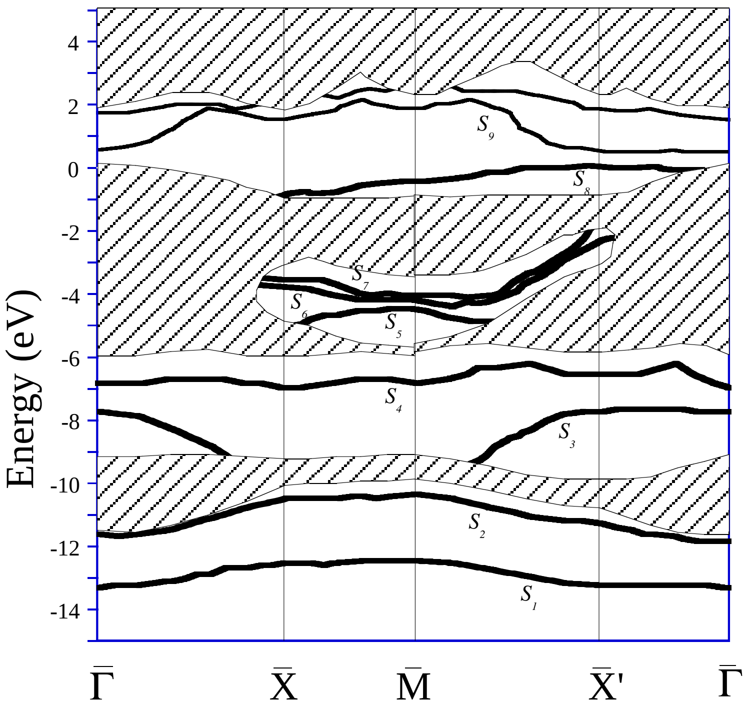

Figure 4.15: Electronic band structure of the InP(110)-S interface: for the exchanged-reacted geometry. Projected bulk spectrum is shown by hatched regions. Occupied and unoccupied surface states are shown by thick and thin curves, respectively.

P(top layer)-S(second layer) and P(top layer)-S(top layer) bondings, respectively. Clearly, the bonding between P and S shows a double humped covalent feature, which is significantly different from the more covalent P-S bonding for the ECLS model. The asymmetry of the heights of the two peaks in Fig. 4.17 can be considered to arise from the difference in the electronegativities of P and S.

A total of eight occupied and the lowest two unoccupied electron states (shown in Fig. 4.15) has been identified. The occupied states S_1 and S_2 lie below the bulk valence band, and S_3 and S_4 lie in the ionic gap. The state S_1 is mainly due to the s-orbital of the top lying S atoms but the state S_2 is due to the s-orbital of the lower lying S atoms. In the ionic gap S_3 is mainly due to the s-orbital of the exchanged P atoms (i.e. in the top layer) with a small contribution from the back bonds of the exchanges (or lower lying) S atoms. It is interesting to note that this state is also mainly localized on the P atom for the ECLS geometry. The state S_4 is mainly a p_y-orbital of the S atom of the top layer. The states S_5,S_6, and S_7 lie in

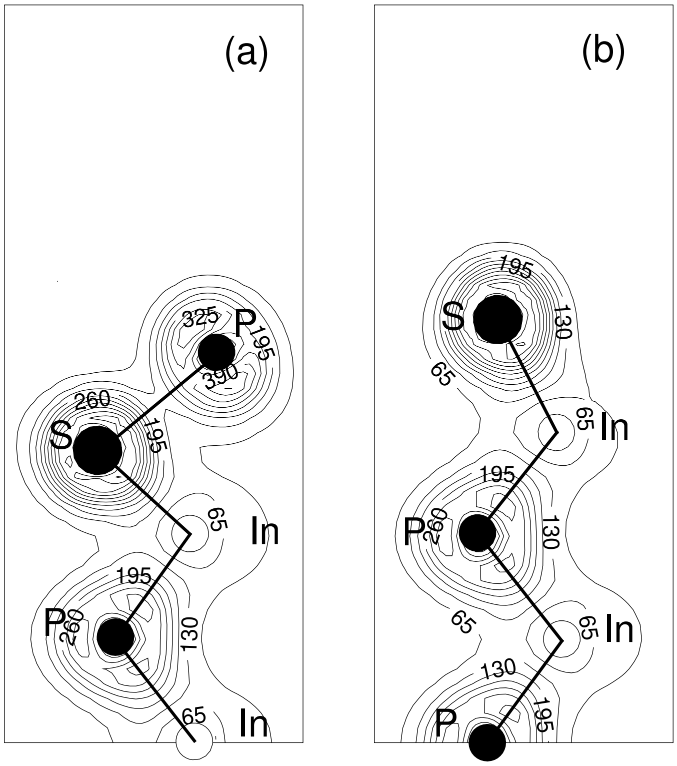

Figure 4.16: Electronic total charge density plots for the exchange-reacted in (a) a vertical plane containing the P-S bond, (b) in a vertical plane containing the In-S bond. The charge density are normalised to 76 electrons per unit cell volume of 631.26 Å^3.

the stomach gap. The state S_7 is a combination of a p_y-orbital of the lower lying S atoms and a p_z-orbital of the top lying S atoms. The highest lying occupied state, S_8, is due to a p-like orbital along the dangling bond direction of the exchanged P atoms in the top layer. The lowest unoccupied state, S_9, is mainly due to a back bond from the exchanged P atoms, with a small contribution from the exchanges S atom and the structure is characterized by a small LDA band gap of 0.4 eV at $\bar{X}'$.

4.3.2.2 Diffuse-reacted and other models

In the diffuse-reacted structure, the P atoms in the top two layers are desorbed and substituted by S atoms. The relaxed geometry for this model is shown Fig. 4.14(b). After total energy minimisation, the vertical buckling of the top layer, consisting of In and S atoms in a chain form, is 0.70 Å. For this chain, the In-S-In bond

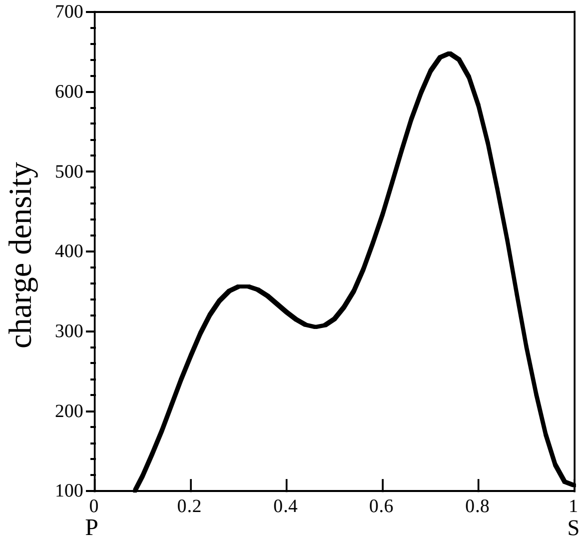

Figure 4.17: Electronic total charge density plots for the exchange-reacted in along the line joining the P and S atoms in the top layer. The charge density are normalised to 76 electrons per unit cell volume of 631.26 Å^3.

angle is 119.1°, somewhat larger than the tetrahedral bond angle. The vertical distance, $d_{12,\perp}$, between the top two layers is 2.21 Å, which is considerably larger than the XSW value [7]. In this model the relaxation of the top two layers is similar: In atoms have relaxed outwards and S atoms inwards, with the magnitude of the tilt angle of the top layer being much bigger than that for the second layer. This relaxation pattern is similar to that obtained for the diffused Se overlayer on InP(110) [23] and GaAs(110) [18]. In the bulk fundamental band gap, two surface states has been identified both being occupied. The state S_6 lies slightly above the bulk valence band continuum along $\bar{X}$-$\bar{M}$-$\bar{X}'$. The highest occupied surface state, S_7, lies slightly above the bulk valence band maximum and shows a modest level of dispersion, as seen in Fig. 4.18. It is mainly contributed by the sp_z-orbital of the In atoms, with a small contribution from the sp_z-orbital of the second-layer S atoms. On the clean InP(110) the In sp_z-orbital is known to be empty, but for the diffuse-reacted model this orbital is full due to the availability of electrons. A similar pattern for the atomic geometry and electronic states for the diffused model was found in the work by Srivastava and Umerski [23] for Se/InP(110) and by Schmidt *et al.* [18] for Se/GaAs(110).

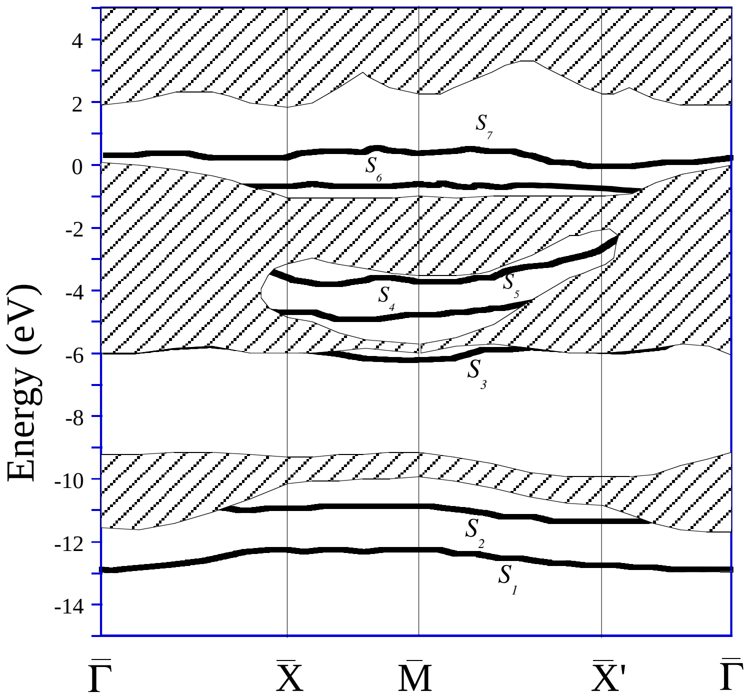

Figure 4.18: Electronic band structure of the InP(110)-S interface: for the diffuse-reacted geometry. Projected bulk spectrum is shown by hatched regions. Occupied and unoccupied surface states are shown by thick and thin curves, respectively.

Two other adsorption geometries were studied: substitutional and substitutional-adatom, as shown in Figs. 4.6(c) and (d). The substitutional model was suggested by Tulke *et al.* and Chassé *et al.* [24, 25] from their LEED and photoemission studies on an annealed As/InP(110) system. The substitutional-adatom model incorporates substitution of S for P and bonding of another S with In along the dangling bond direction. After energy minimisation, these two models were found to show metallic band structure features, suggesting that passivation in this system would not be achieved with these overlayer configurations.

4.4 Summary

In this chapter the clean and S covered InP(110) surfaces were studied. The calculated equilibrium geometries agree well with the results obtained from other theoretical and experimental results. The band strutures are also in agreement with the angle-resolved photemission results. We have mainly performed calculations for the atomic geometry and electronic structure of S adsorbed InP(110) using various proposed models. For non-reacted structural models with half-monolayer coverage the interchain bridge geometry was found to be the most energetically favourable. The In-S and P-S bond lengths are 2.67 Å and 2.21 Å, respectively, and are characterized by partially ionic character. The vertical distance between the overlayer and the substrate is approximately 1 Å, which is much smaller than that the XSW analysis by Johal *et al.* would suggest. The resulting band structure is semi-metallic. For non-reacted structural models with full-monolayer coverage, the ECLS was the lowest energy configuration. For this geometry the S-S bonding shows a double humped covalent feature, with an expanded bond length of 2.46 Å. The vertical distance between the overlayer and the substrate is 1.73 Å, which is considerably shorter than the XSW value. The LDA band structure shows a band gap of approximately 1 eV. The exchange-reacted model is more favourable than the ECLS model on energy grounds, and leads to a vertical distance between the top two layers of 1.98 Å, which is in excellent agreement with the XSW result of 1.95 $\pm$ 0.02 Å. However, it is found that the calculated band gap for this geometry is only 0.4 eV. While the diffused-reacted model is characterized by a much larger interplanar distance than the XSW value, other reacted models result in a semi-metallic band structure.

Bibliography

[1] Y. Tao, A. Yelon, E. Sacher, Z. H. Lu, and M. J. Graham, Appl. Phys. Lett. **60**, 2669 (1992).

[2] H. Oigawa, J. F. Fan, Y. Nannichi, H. Sugahara, and M. Oshima, Jpn. J. Appl. Phys. **30**, L332 (1991).

[3] J.-M Jin, M. W. C. Dharma-wardana, D. J. Lockwood, G. C. Aers, Z. H. Lu, and L. J. Lewis, Phys. Rev. Lett. **75**, 878 (1995).

[4] T. Ohno, and K. Shiraishi, Phys. Rev. B **42**, 11194 (1990).

[5] A. C. Ferraz and G. P. Srivastava, Surf. Sci. **377**, 121 (1997).

[6] A. Kahn, Surf. Sci. **299-300**, 469 (1994).

[7] T. K. Johal, P. Finetti, V. R. Dhanak, A. W. Robinson, A. Patchett, D. R. T. Zahn, and R. McGrath, Appl. Surf. Sci. **104**, 257 (1996).

[8] T. Schröter, A. Chassé, I. Eckardt, K. Tiedge, N. Wagner, D.R.T. Zahn, C.Nowak, A. Hempelmann, and W. Richter, Surf. Sci. **307-309**, 650 (1994).

[9] J. C. Woicik, T. Kendelewicz, K. E. Miyano, P. L. Cowan, C. E. Bouldin, B. A. Karlin, P. Pianetta and W. E. Spicer, Phys. Rev. Lett. **68**, 341 (1992).

[10] J. R. Chelikowsky and M. L. Cohen, Solid State Commum. **29**, 267 (1979).

[11] G. P. Srivastava, Rep. Prog. Phys. **60**, 561 (1997).

[12] J. L. A. Alves, J. Hebenstreit, and M. Scheffler, Phys. Rev. B **44**, 6188 (1991).

[13] *Physics of Group IV and III-V Compounds*, Landolt-Börnstein, New Series, Group III, Vol. 17a (Springer, Berlin 1982).

[14] C. B. Duke, A. Paton, C. Mailhiot, and A. Kahn, J. Vac. Sci. Technol. B **3**, 1087 (1985).

[15] J. Fritsch, P. Pavone, and U. Schröder Phys. Rev. B **52**, 11326 (1995).

[16] L. Sorba, V. Hinkel, H. U. Middelmann, and K. Horn, Phys. Rev. B **36**, 8075 (1987).

[17] A. Umerski and G. P. Srivastava, Phys. Rev. B **51**, 2334 (1995).

[18] W. G. Schmidt and F. Bechstedt, Surf. Sci. **331-333**, 557 (1995).

[19] G. Burns, *Solid State Physics*, International Edition, Acedemic Press, 1990.

[20] G. P. Srivastava and R. P. Martin, J. Phys. CM **4**, 2009 (1992).

[21] D. P. Woodruff, Prog. in Surf. Sci. **57**, 1 (1998).

[22] C. Mailhiot, C. B. Duke and D. J. Chadi, Phys. Rev. B **31**, 2213 (1985).

[23] G. P. Srivastava and A. Umerski, Surf. Sci. **331-333**, 590 (1995).

[24] A. Tulke and H. Lüth, Surf. Sci. **211-212**, 1001 (1989).

[25] T. Chassé, G. Neuhold, and K. Horn, Surf. Sci. **331-333**, 511 (1995).

Chapter 5

Adsorption of H_2S on InP(110), GaAs(110) and GaP(110)

5.1 Introduction

The adsorption of H_2S on III-V(110) has been studied extensively using the LEED, AES and UPS. A GaAs surface exposed to air shows poor electronic properties, due to a high density of surface states pinning the Fermi level in the middle of the band gap. Recently it has been shown [1, 2, 3, 4, 5] that the electronic properties of the (100), (110) and (111) surfaces of GaAs improve significantly upon sulphide treatment. In general three different types of sulphur sources have been used: treatment with a solution of $Na_2S{\cdot}9H_2O$ [6] or $(NH_4)_2S_x$ [4, 5, 7], treatment with H_2S gas [1, 2, 3, 8, 9, 10, 11], and using S from a solid state source in ultra high vacuum conditions [12].

In early studies using LEED, AES and angle-resolved UPS, Williams and co-workers [8, 13] reported that exposure to H_2S resulted in an ordered overlayer on InP(110). They proposed that for low exposures the room temperature adsorption of H_2S on InP(110) was mostly molecular, and found that the molecule easily desorbed upon heating the sample. From the AES and UPS studies, Kuhr *et al.* [1] and Ranke *et al.* [2, 3] concluded that at 150 K, H_2S is adsorbed on GaAs(110) either as a molecule or as partially dissociative species like $(SH)^-$ and H^+ on the anion surface atoms, leaving the surface cations essentially unaffected. (Their work also concludes that at 720 K, atomic sulphur is adsorbed which begins to penetrate into the lattice for higher exposures.) However, from the core-level photoemission results Ranke *et al.* [2, 3] could not conclude what is the correct form of H_2S adsorption - molecular or dissociative.

Recently the adsorption of H_2S on III-V(110) has been studied in detail by Dudzik *et al.* [9, 10, 11, 14] using the core level x-ray photoelectron spectroscopy (SXPS), normal-incidence x-ray standing wave (NIXSW), valence band angle-resolved UPS (ARUPS) and LEED. They have reported that the adsorption of H_2S occurs at room temperature on InP(110) and GaP(110) but only at low temperatures (200 K or below) on GaAs(110). From studies of all the spectral changes and temperature effects they have firmly proposed a *dissociative adsorption model* for H_2S on the three surfaces, consistent with a (1×1) LEED pattern. According to their model, the H_2S molecule dissociates into the $(SH)^-$ radical and the H^+ ion, with H^+ bonded to P and $(SH)^-$ located in the anion site of the continued-layer structure, bonded to the surface cation. The dissociative molecular model is supported by the observation that the reactivities of different III-V semiconductors scale with the proton affinity of the anion dangling bond [11].

In this chapter *ab initio* theoretical investigations of the atomic geometry, electronic states, and bonding of H_2S on III-V(110) using the dissociative molecular geometry proposed by Dudzik *et al.* have been investigated. From the total energy calculations it is proposed a slight modification to the orientation of the $(SH)^-$ radical over the model proposed by Dudzik *et al.*

5.2 The H_2S-deposition models on the III-V(110) surfaces

The calculated equilibrium lattice constants for bulk InP, GaAs and GaP are 5.67, 5.50, and 5.35 Å, respectively. These values are in agreement with other theoretical studies [15] using the pseudopotential method, and were used in performing the surface calculations. The unit cell included an atomic slab with seven layers of III-V substrates and then H_2S molecules on each side of the slab, and a vacuum region equivalent of six substrate atomic layers. The resulting atomic geometries and band structures will be described and compared with the existing experimental results in the following sections.

The H_2S/III-V(110) interface was modelled by considering two different dissociative molecular geometries within the continued-layer structure. In both geometries the proton H^+ is bonded to the surface anion (i.e. P or As) along the dangling bond direction and the $(SH)^-$ complex is bonded to the surface cation (i.e. In or Ga). In Model I, while the S atom lies along the cation dangling bond direction, the H^- ion is located in the direction suggested by Dudzik *et al.* [11], as shown in Fig. 5.1(a). Our energy minimization procedure, starting with this geometry, suggested that the H^- ion would move in the direction opposite to that suggested by Dudzik *et al.* This led us to consider Model II, with the H^- ion located along the dangling bond direction of the S atom in the continued-layer structure, as shown in Fig. 5.1(b). As possible geometries, it was considered a number of different orientations of H^- bonded to S. As the orientation is changed from that for Model II towards Model I, the total energy of the system increases. Model I is unstable and lies at an energy 1.2 eV higher than Model II for H_2S/InP(110). Similar findings were made for the other two surfaces. Model II was subsequently used in all the cases studied here.

It is well known that the relaxation pattern of clean III-V(110) surfaces is characterized by an outward (inward) movement of surface anion (cation), with a tilt in the surface layer in the range $27^\circ - 32^\circ$ [15, 16], as seen and mentioned in the previous chapter. The calculations (for Model II) reveal that upon H_2S adsorption all the three surfaces are derelaxed, acquiring a very small counter relaxation: the surface cation (anion) has moved outward (inward) by a small amount. Fig. 5.2 shows schematic relaxed top and side views of Model II and indicates the key structural parameters. The calculated relaxed atomic geometrical parameters are listed in Tab. 5.1. We will be discussing the three surfaces individually.

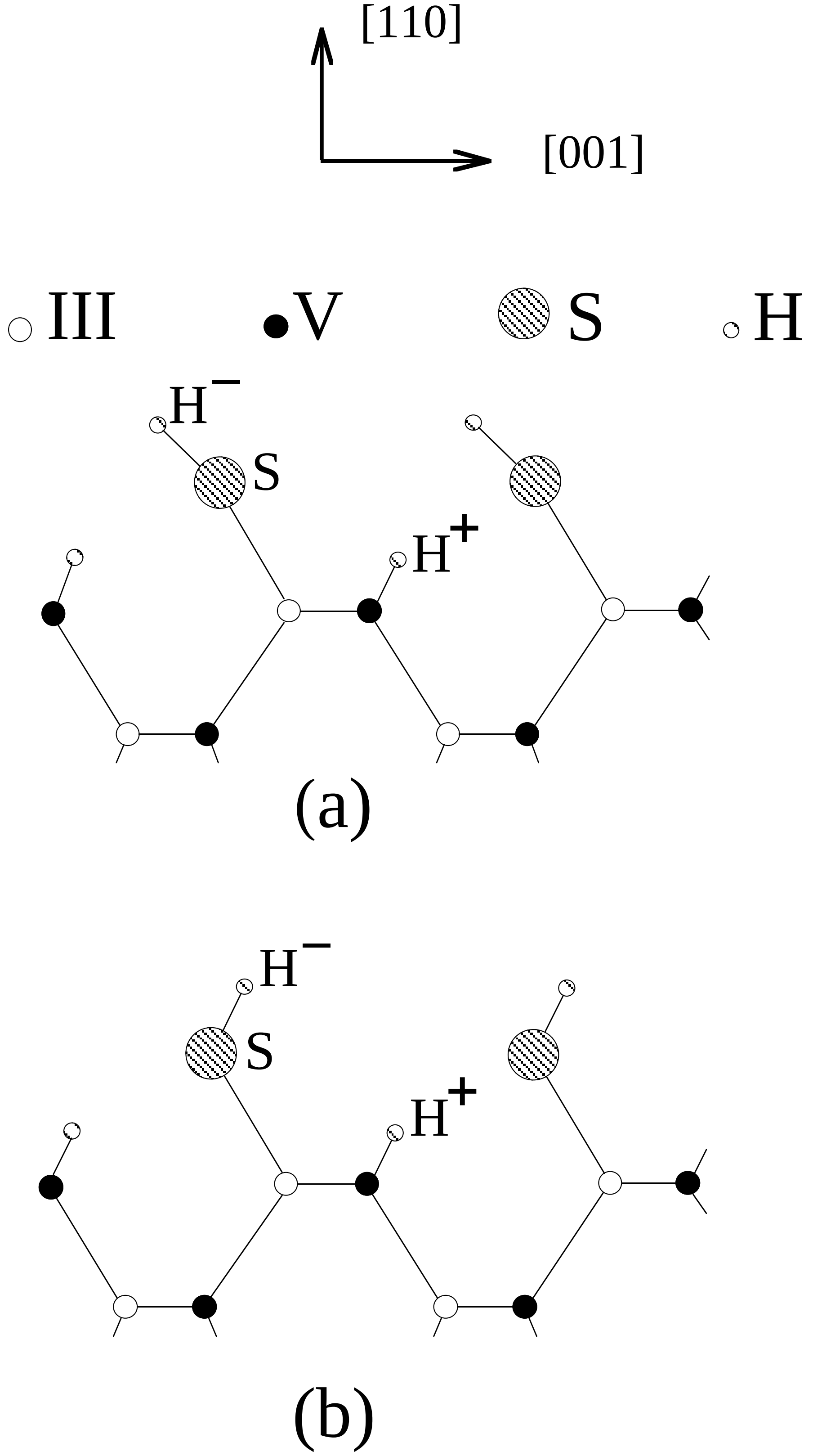

Figure 5.1: Schematic side view for the H_2S adsorption on III-V(110), (a) Model I as proposed by Dudzik *et al.* [11] and (b) Model II as proposed by us.

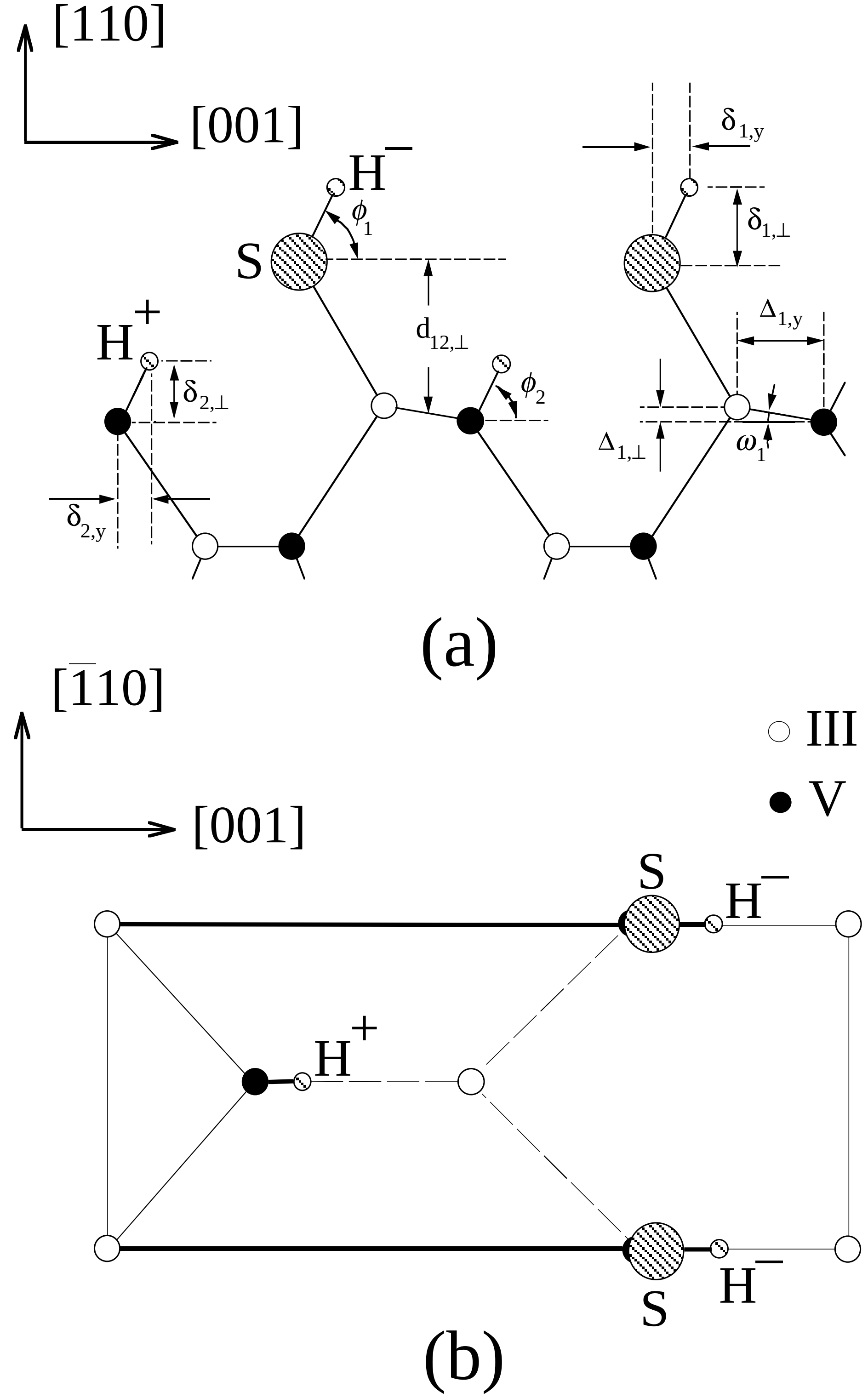

Figure 5.2: Schematic relaxed atomic geometry for Model II of H_2S adsorption on III-V(110) with the key parameters, (a) side view and (b) top view.

	$d_{12,\perp}$	$\delta_{1,\perp}$	$\delta_{1,y}$	$\delta_{2,\perp}$	$\delta_{2,y}$	$\Delta_{1,\perp}$	$\Delta_{1,y}$	ϕ_1(deg)	ϕ_2(deg)	ω_1(deg)
InP	1.87	1.33	0.36	1.00	1.80	0.19	1.54	74.85	29.05	-7.03
GaAs	1.67	1.28	0.55	1.14	2.03	0.15	1.37	66.75	29.32	-6.37
GaP	1.65	1.29	0.57	1.10	2.05	0.12	1.31	66.20	28.22	-5.23

Table 5.1: Structural parameters (in Å) of Model II (see Fig. 5.2) for the H_2S-adsorption on InP(110), GaAs(110) and GaP(110) surfaces.

5.3 H_2S-deposition onto InP(110)

5.3.1 Atomic Geometry

Using the same pseudopotential method as in this work, it was found earlier that on InP(110) the top layer tilts by 27.1° and the second layer tilts by -3.1° (the negative sign indicates tilt in the opposite direction). Upon H_2S adsorption, the tilt of the top InP(110) layer is changed to -7° and its vertical buckling ($\Delta_{1,\perp}$) is reduced to 0.19 Å. These values are only a little different from those for the second layer on the clean InP(110) surface. Thus the adsorption of H_2S has practically derelaxed the InP(110) surface. The perpendicular distance ($\delta_{2,\perp}$) between P and H^+ is about 1.00 Å, and the d(P-H^+) bond length is the same as the sum of the corresponding covalent radii, 1.40 Å [17]. The perpendicular distance ($\delta_{1,\perp}$) between S and H^- is 1.33 Å, and the bond length value of 1.38 Å for d(S-H^-) is 3% bigger than the sum of the corresponding covalent radii. The calculated perpendicular average distance $d_{12,\perp}$ between the sulphur atom and the topmost InP layer is 1.87 Å. This result is in good agreement with the value of 1.97 Å determined from the XSW measurement by Dudzik *et al.* [11]: the difference is at least partly due to the theoretical lattice constant being 3.5% smaller than the experimental value. It is also interesting to note that the calculated value of $d_{12,\perp}$ for H_2S/InP(110) is very close to the corresponding value for the S/InP(110) system calculated in a recent theoretical study [18] (1.98 Å) and determined from XSW measurements (1.95 Å) [12]. The calculated bond length d(In-S) is 2.61 Å, approximately 5% larger than the sum of the covalent radii of In and S [17].

From the NIXSW studies Dudzik *et al.* [11] have determined the offsets of the S atom from the ideal continued-layer phosphorus site. They find that these shifts are 0.02 ± 0.08 Å, -0.04 ± 0.05 Å and -0.10 ± 0.06 in the [$\bar{1}$10], [001] and [110] directions, respectively. The calculated offsets are somewhat different from these values. It is found that the sulphur atom shifts by -0.37 Å in the [001] direction and by 0.02 Å in the [110] direction from the ideal continued-layer structure phosphorus site. There is no shift in the [$\bar{1}$10] due to the symmetry present on the (1×1) surface. The calculated shift along [001] agrees in sign but is bigger than the NIXSW value. Neither the sign nor the magnitude of the calculated shift in the surface normal direction [110] agrees with the NIXSW determination.

The ARUPS data obtained by Dudzik *et al.* [14] indicate up to six surface related bands in the binding energy range 0 eV to 7 eV. Three of these, labelled α, β, and γ, have been identified as adsorbate related. While not making a clear identification, Dudzik *et al.*'s work seems to indicate that the feature labelled β is a SH-line, following the investigation of H_2S/Si(100) by Schröder-Gergen and Ranke [19]. A fourth band, labelled X_3, is considered to originate from adsorption enhanced bulk density of states. However, the authors are uncertain about the orbital nature of these states.

5.3.2 Electronic states and Chemical bondings

A total of five occupied electronic states have been identified, as shown in Fig. 5.3. Also shown are the ARUPS data obtained by Dudzik *et al.* [14]. The experimental spectra have been rigidly shifted upwards by 0.5 eV to show maximum level of correspondence with theory. The electronic total charge density plots in vertical planes containing the P-H^+ and S-H^- bonds are shown in Figs. 5.4(a) and (b), respectively. The orbital features of the individual states at the $\bar{M}$ point are shown in Figs. 5.5- 5.7. As seen in Fig. 5.4(a) the In-P bonding at the interface is partly covalent and partly ionic, similar to that in bulk InP. The In-S bonding is also partly covalent and partly ionic, but is stronger than the In-P bonding. The P-H^+ and S-H^- bondings show some covalency and pronounced ionic character.

The occupied state S_1 lies below the bulk valence band continuum. This state shows covalent bonding between the *s*-orbital of the H^- ion and the *s*-orbital of the surface S atom, as shown in Fig. 5.5(a). In the binding energy range 2 eV to

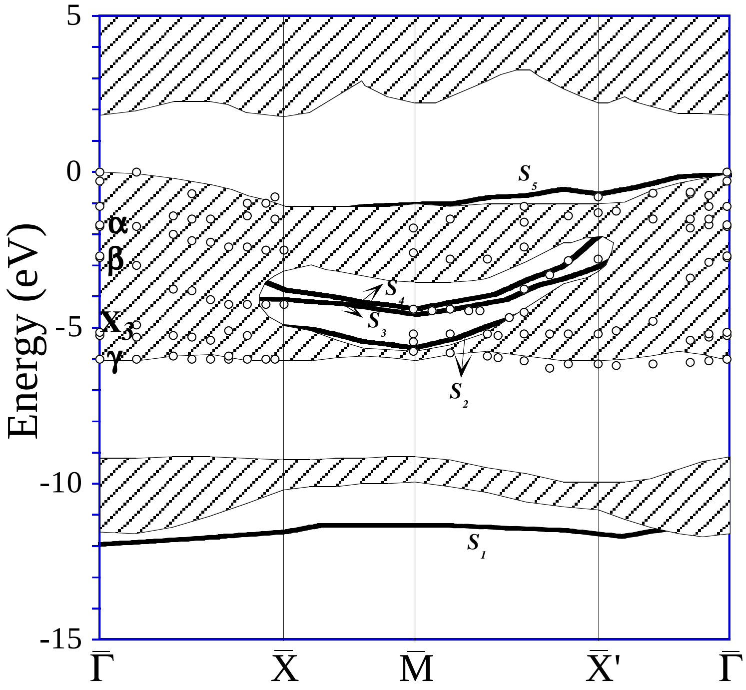

Figure 5.3: Electronic band structure of the InP(110)-H_2S interface. The projected bulk spectrum is shown by hatched regions. The calculated electronic states are shown by thick curves and the experimental results of Dudzik *et al.* [14] are indicated by open symbols. The experimental data has been rigidly shifted upwards by 0.5 eV as discussed in the text.

6 eV it is obtained three states, labelled S_2, S_3 and S_4, which are clearly seen in the stomach gap region. While the ARUPS data [14] indicates the band γ almost resonant with bulk at the upper end of the ionic gap, this calculations do not give any surface states in that region. From Fig. 5.5(b) it is noted that the state S_2 is resonant with bulk and has a pronounced contribution from the second-layer In atoms, as found on the clean InP(110) surface, but also has some contribution from the surface PH^+ and $(SH)^-$ complexes. Therefore, this state is a surface state modified by the dissociative adsorption of H_2S. This state can be compared to the band labelled X_3 in the ARUPS studies by Dudzik *et al.* [14]. In the middle of the stomach gap two closely lying bands has been identified, labelled S_3 and S_4. The energy location and dispersion of the experimentally measured band β matches with both these bands, in particular the S_3 band. However, we do not agree with the description of the orbital nature of the experimental band β forwarded by Dudzik

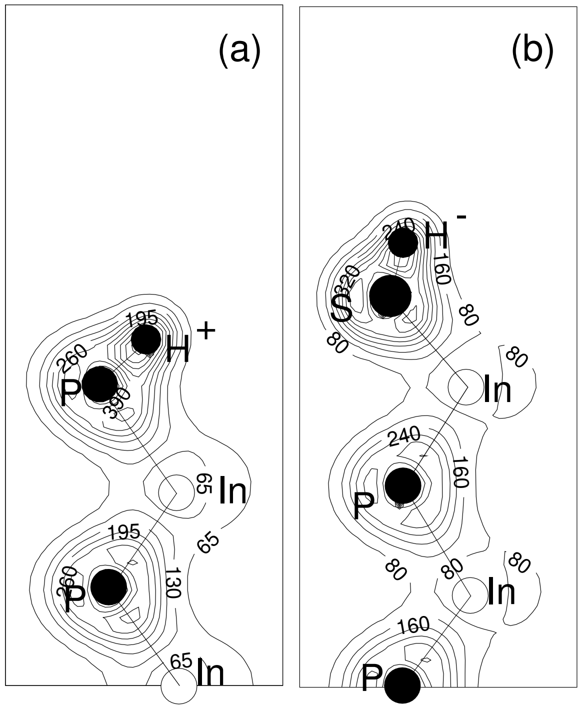

Figure 5.4: Electronic total charge density plots of the InP(110)-H_2S interface in (a) a vertical plane containing the P-H^+ bond, and (b) a vertical plane containing the S-H^- bond. The contour values are normalised to 72 electrons per unit cell volume of 631.26 Å^3.

et al. It is found that the state S_3 is made of the back bond orbital of the surface S atoms and *s*-orbital of the hydrogen ion in the vertical plane containing the S-H^- bond, as shown in Fig. 5.6(c). The state S_4 is a P-H^+ bonding state, made of the dangling bond of the P atom and the *s*-orbital of H^+, as shown in Fig. 5.6(d). The experimentally measured band α can be matched with our state S_4 around the $\bar{X}$' point. The highest occupied state lies very close to the edge of the bulk region in the fundamental gap, labelled S_5, due to the *p*-orbital of the S atoms, shown in Fig. 5.7(e). It is interesting to note that this adsorbate state lies roughly at the same energy position as the P derived dangling bond state on the clean InP(110) surface. This is not surprising, as in the dissociative model the $(SH)^-$ complex plays the role of anion on the clean surface. In the experimental ARUPS data there are features which can be matched with our S_5 state along $\bar{\Gamma}$-$\bar{X}$'-$\bar{M}$. We do not find any unoccupied electronic states in the fundamental band gap, which therefore remains free of surface states.

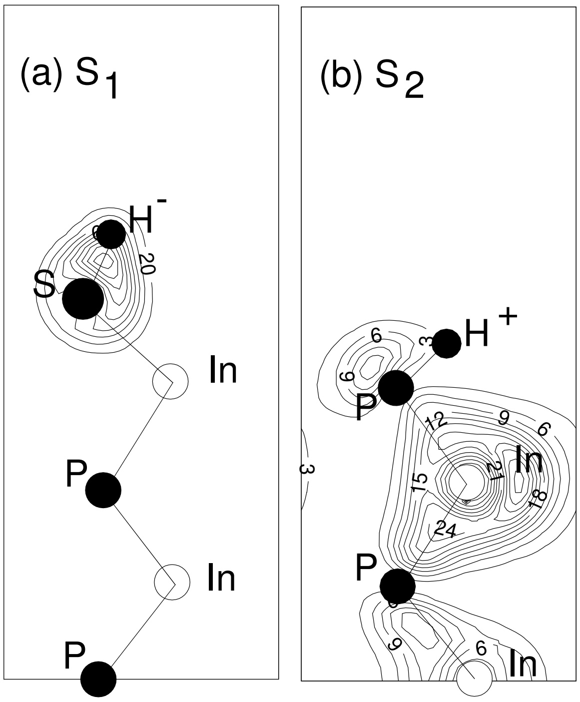

Figure 5.5: Electronic charge density plots for individual surface states for the relaxed geometry of the InP(110)-H_2S interface: (a) S_1 and (b) S_2 at $\bar{M}$ in a horizontal plane. The contour values are normalised to 2 electrons per unit cell volume of 631.26 Å^3.

Our analysis of the states, therefore, indicates that within the dissociative model adsorption of H_2S on InP(110) leads to S p-like (S_5), $(SH)^-$-like (S_1 and S_3) and PH^+-like (S_4) states, and the PH^+ and $(SH)^-$ complexes modify the surface state S_2 on the clean surface originating from the second-layer cation.

5.4 H_2S-deposition onto GaAs(110)

5.4.1 Atomic Geometry

For the adsorption of H_2S onto GaAs(110), the structural and electronic results should be considered in the same way as the adsorption on the InP(110) surface. On the clean GaAs(110) surface, the top layer Ga (As) atoms move inwards (upwards), with a tilt (ω_1) of the topmost layer of 30.2°, with a vertical buckling $\Delta_{1,\perp}$ of 0.66 Å [20]. The second atomic layer shows a tilt of -3.9° [20]. Upon H_2S-adsorption, the tilt angle (ω_1) of the topmost GaAs(110) layer is changed to -6.4°, with a

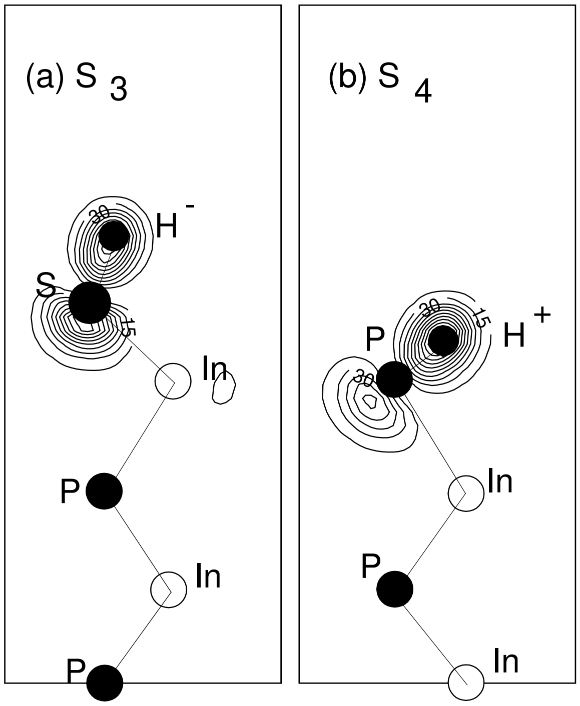

Figure 5.6: Electronic charge density plots for individual surface states for the relaxed geometry of the InP(110)-H_2S interface: (a) S_3 at $\bar{M}$ (b) S_4 at $\bar{M}$ in a horizontal plane. The contour values are normalised to 2 electrons per unit cell volume of 631.26 Å^3.

vertical buckling $\Delta_{1,\perp}$ of 0.15 Å. Thus the surface has acquired a small counter relaxation. The d(Ga-As) bond length is 2.40 Å on the clean surface, and only slightly changes to 2.37 Å upon H_2S-adsorption. The d(Ga-S) bond length is 2.20 Å, about 2% smaller than the sum of the corresponding covalent radii. It is found that the perpendicular distance between As and H^+ ($\delta_{2,\perp}$) is about 1.14 Å, and the d(As-H^+) bond length is 1.54 Å, while the perpendicular distance between the S atom and the H^- ion ($\delta_{1,\perp}$) is 1.28 Å and the d(S-H^-) bond length is 1.40 Å. The calculated distances d(As-H^+) and d(S-H^-) are about 4% bigger than the sum of the corresponding covalent radii. Our calculated perpendicular average distance ($d_{1,\perp}$) between the sulphur atom and the topmost layer of the GaAs surface is 1.67 Å. This value is smaller than the value of 1.87 Å for InP.

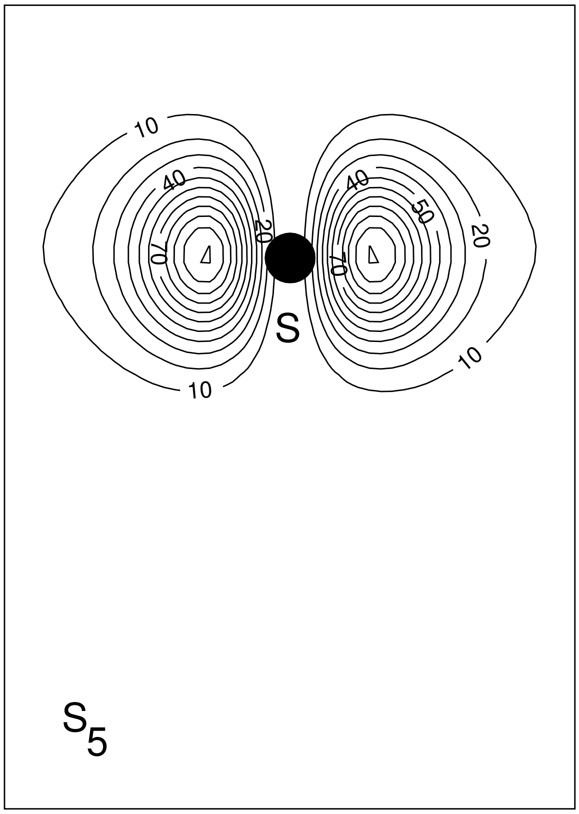

Figure 5.7: Electronic charge density plots for individual surface states for the relaxed geometry of the InP(110)-H_2S interface: S_5 at $\bar{M}$ in a vertical plane. The contour values are normalised to 2 electrons per unit cell volume of 631.26 Å^3.

5.4.2 Electronic states and Chemical bondings

A total of five occupied electronic states has been identified, labelled S_1 to S_5, as in the case of InP, and shown in Fig. 5.8. The electronic total charge density plots show the same bonding characteristics as for the H_2S/InP(110) system. In addition, it is interesting to say that the Ga-S bonding is stronger than the Ga-As bonding. The occupied state S_1 lies below the bulk valence band, and is due to the covalent bonding between the s-orbitals from the adsorbate S atom and the H^- ion. The orbitals characters of the states S_2, S_3 and S_4 are shown in Fig. 5.9. As in the case of H_2S/InP(110), the state S_2 is primarily localized on Ga atoms at the second GaAs layer but also has some contribution from the AsH^+ and $(SH)^-$ complexes. It is a resonant state, with its energy close to the lower edge of the stomach gap.

The experimental study by Dudzik *et al.* [10] indicates that in the binding

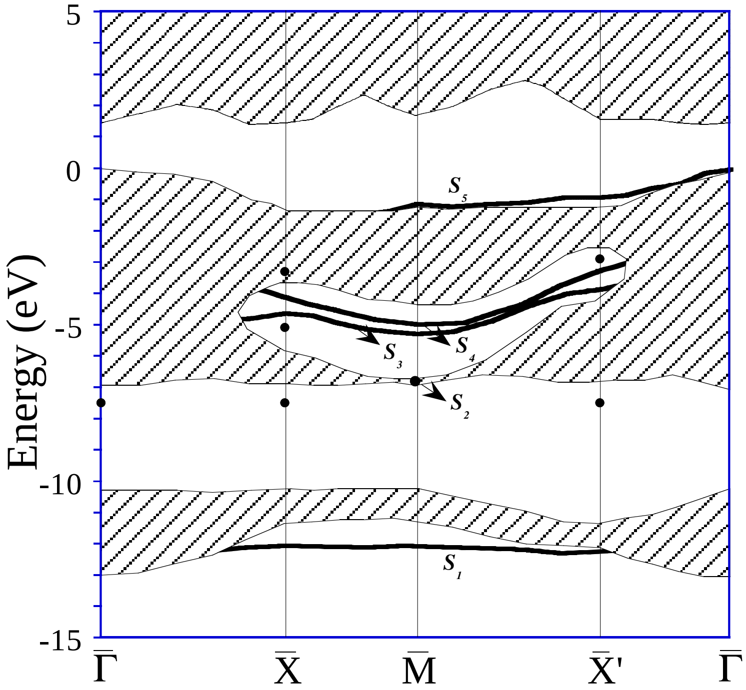

Figure 5.8: Electronic band structure of the GaAs(110)-H_2S interface. The projected bulk spectrum is shown by hatched regions. The calculated electronic states are shown by thick curves and the experimental results of Dudzik *et al.* [11] are indicated by solid symbols.

energy range 2 to 8 eV there are up to three features which can be associated with the adsorption of H_2S. One of these lies in the ionic band gap at approximately the binding energy of 7.5 eV at $\bar{\Gamma}$, $\bar{X}$ and $\bar{X}$'. We do not find any state in the ionic gap. The two other features observed experimentally at $\bar{X}$ can be compared with our states S_3 and S_4. Similarly, the state observed experimentally at approximately 2.5 eV binding energy at $\bar{X}$' can be compared with our state S_4. It is found that the dispersion as well as the orbital characteristics of the states S_3, S_4 and S_5 for H_2S/GaAs(110) are identical to those for H_2S/InP(110). The highest occupied adsorbate-induced state, S_5, is seen as a rather flat band just above the bulk valence band continuum around the $\bar{X}$' point. We do not find unoccupied states in the fundamental gap. There is a band gap (within the local-density approximation) of about 1.40 eV at $\bar{\Gamma}$, which is very close to the low-temperature experimental value of 1.52 eV [21]. This close agreement between the LDA band gap and the experimental value is due to the smaller theoretical lattice constant used in our

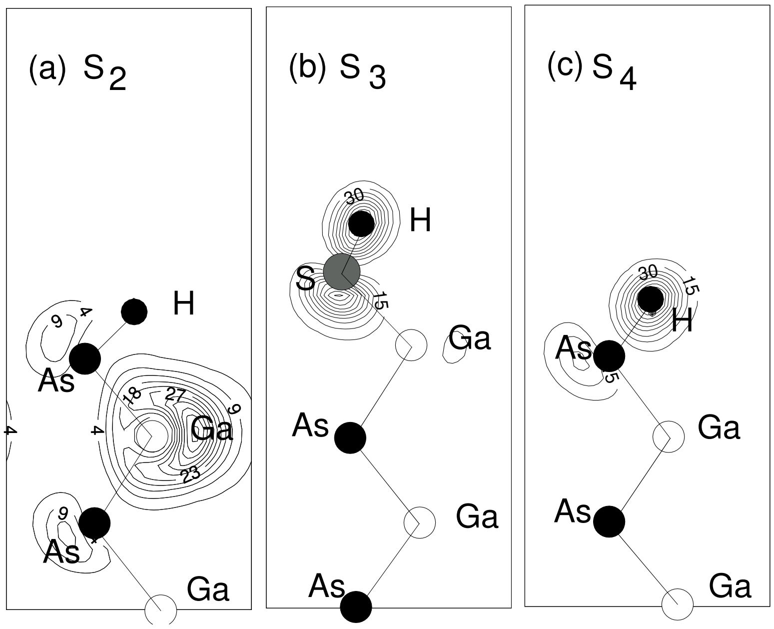

Figure 5.9: Electronic charge density plots for individual surface states for the relaxed geometry of the GaAs(110)-H_2S interface: (a) S_2 (b) S_3, and (c) S_4 at $\bar{M}$ in a horizontal plane. The contour values are normalised to 2 electrons per unit cell volume of 631.26 Å^3.

work.

5.5 H_2S-deposition onto GaP(110)

5.5.1 Atomic Geometry

The adsorption of H_2S onto GaP(110) is similar to that on InP(110), but seems to be somewhat more rapid [10]. Therefore we have used the same starting model (i.e. Model II) as in our InP and GaAs studies in order to calculate the geometrical parameters and electronic structure of the H_2S/GaP(110) surface. The results are similar to those obtained for the H_2S/InP(110) and H_2S/GaAs(110) systems. Again, it can be noted that the Ga-S bonding is stronger than the Ga-P bonding.

The clean GaP(110) surface is characterized [22] by a tilt of the top layer by 27.6° and a vertical buckling of 0.58 Å. The second layer shows a tilt of -3.2°. Upon H_2S adsorption the tilt of the top GaP layer becomes -5.23°. Thus, similar to GaAs and InP the GaP top layer is not only derelaxed but also shows a small amount

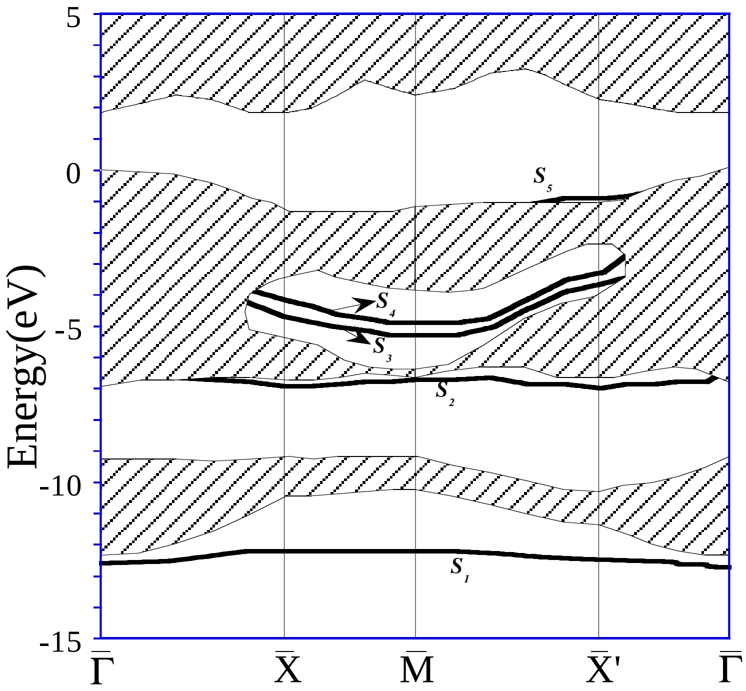

Figure 5.10: Electronic band structure of the GaP(110)-H_2S interface. The projected bulk spectrum is shown by hatched regions and the electronic states are shown by thick curves.

of counter-relaxation. The calculated perpendicular average distance between the sulphur atom and the topmost GaP layer is 1.65 Å. The d(S-H^-) and d(P-H^+) bond lengths are 1.41 Å and 1.49 Å, respectively.

5.5.2 Electronic states and Chemical bondings

For the H_2S/GaP(110) system five surface states have been identified, as shown in Fig. 5.10. Their orbital characteristics are similar to the corresponding states obtained for the other two systems. The state S_1 is clearly split off below the bulk valence band. The state S_2 lies at the upper edge of the ionic gap in GaP. The states S_3 and S_4 lie in the middle of the stomach gap. Once again, their orbital characteristics, shown in Fig. 5.11, are similar to those for the other two systems. Finally, the highest occupied surface state, S_5, is only seen just above the bulk valence band continuum around $\bar{X}$'. We do not find any unoccupied states in the fundamental gap either. There is a band gap (within the local-density approximation) of about 1.8 eV at $\bar{\Gamma}$, which is $\sim$0.50 eV smaller than the experimental value [21].

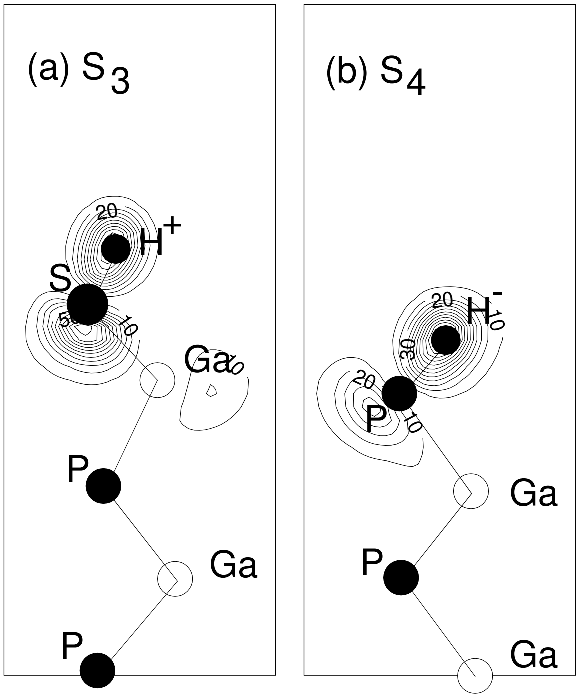

Figure 5.11: Electronic charge density plots for individual surface states for the relaxed geometry of the GaP(110)-H_2S interface: (a) S_3 at $\bar{M}$ (b) S_4 at $\bar{M}$. The contour values are normalised to 2 electrons per unit cell volume of 631.26 Å^3.

5.6 Discussion of results for H_2S adsorption on InP, GaAs and GaP

From the results presented above, one can obtain certain trends in structural and electronic properties of H_2S adsorption on III-V(110) surfaces. The first point to notice is that upon H_2S adsorption the top atomic layer of InP(110) exhibits a bigger counter-relaxation than do the GaAs(110) and GaP(110) surfaces. Secondly, the vertical distance between the S atom and the topmost substrate layer, $d_{12,\perp}$, is much bigger for InP(110) than for GaAs(110) or GaP(110). It is also found that the vertical distance between H^+ and its neighbouring anion, $\delta_{2,\perp}$, is much smaller for InP(110) than for GaAs(110) and GaP(110). However, the vertical distance $\delta_{1,\perp}$ between the H^- ion and the S atom in the $(SH)^-$ complex remains constant within 0.05 Å for all the systems studied here.

The electronic state S_1 derived from the S-H^- bonding is located in the binding energy range 12.0 - 12.5 eV below the bulk valence band maximum for all the three substrates. The mainly cation derived state S_2 lies at $\bar{M}$ at approximately -6.75 eV for Ga substrates (i.e. GaAs and GaP) and at approximately -5.5 eV for In substrate (i.e. InP). The state S_3 (which is a cation-$(SH)^-$ bonding state) lies at $\bar{M}$ at -4.5 eV for InP substrate and at -5.25 eV for GaAs and GaP substrates. This difference in the energy location of the S_3 state can be understood on the basis of its cation-$(SH)^-$ bonding nature. Similarly, it is found that the state S_4 lies at the same energy at $\bar{M}$ for the GaAs and GaP substrates, but is pushed upwards by 0.5 eV for the InP substrate. This energy difference between the In and Ga compounds is much smaller than the difference for the S_3 state. This is not surprising as the S_4 state is anion-H^+ derived. The state S_5 derived from *p*-orbitals of the S atom shows a similar dispersion pattern for the three substrates.

Investigations of the total electronic charge density plots suggest that the In-S bond is stronger than the In-P bond, the Ga-S bond is stronger than the Ga-P and Ga-As bonds, and the In-S bond is slightly stronger than the Ga-S bond. As expected, the S-H^- and anion-H^+ bondings are rather similar for the three substrates.

5.7 Summary

Using an *ab initio* pseudopotential calculation the atomic geometry, electronic states and bonding of H_2S adsorbed onto InP(110), GaAs(110) and GaP(110) semiconductor surfaces were studied. Starting with the dissociative molecular model proposed by Dudzik *et al.*, we arrived at a slightly different bonding configuration of the molecule: the $(SH)^-$ ion is located in the anion site of the continued-layer structure, bonded to the surface cation, and the H^- ion is bonded to the surface S atoms along the dangling bond direction. The adsorption of the molecule generates a small amount of counter-relaxation of the topmost layer of the substrate.

The calculated average distance between the S atom and the topmost substrate layer is 1.87 Å, 1.67 Å and 1.65 Å for the InP, GaAs and GaP substrates, respectively. The calculated result for H_2S/InP is in excellent agreement with the experimental value of 1.90 Å obtained by Dudzik *et al.* [11]. As can be expected, the S-H^- bond length is almost the same for the three substrates: 1.38, 1.40 and 1.41 Å for InP, GaAs and GaP respectively. The S-H^- and the anion-H^+ bonds are partly covalent and partly ionic. The calculated electronic states originating from S-H^- and anion-H^+ bondings are in good agreement with photoemission results obtained by Dudzik *et al.* [14]. For all the three adsorbate systems the bulk band gap is free of surface states. Thus we expect that the adsorption of H_2S on other III-V semiconductors would have the same passivation behaviour.

Bibliography

[1] H. J. Kuhr, W. Ranke and J. Finster, Surf. Sci. **178**, 171 (1986).

[2] W. Ranke, J. Finster and H. J. Kuhr, Surf. Sci. **187**, 112 (1987).

[3] W. Ranke, H. J. Kuhr and J. Finster, Surf. Sci. **192**, 81 (1987).

[4] H. Oigawa, J. F. Fan, Y. Nannichi, K. Ando, K. Saiki, and A. Koma, Jpn. J. Appl. Phys. **28**, L340 (1989).

[5] H. Oigawa, J. F. Fan, Y. Nannichi, H. Sugahara, and M. Oshima, Jpn. J. Appl. Phys. **30**, L322 (1991).

[6] C. J. Sandroff, R. N. Nottenburg, J. C Bischoff, and R. Bhat, Appl. Phys. Lett., **33**, 51 (1987).

[7] Y. Nannichi, J. Fan, H. Oigawa, and A. Koma, Jpn. J. Appl. Phys. **27**, L2367 (1988).

[8] V. Montgomery, R. H. Williams and G. P. Srivastava, J. Phys. C: Solid State Phys. **14**, L191 (1981).

[9] E. Dudzik, R. Whittle, C. Müller, I. T. McGovern, C. Nowak, A. Märkl, A. Hempelmann, D. R. T. Zahn, A. Cafolla, W. Braun, Surf. Sci. **307**, 223 (1994).

[10] E. Dudzik, C. Müller, I. T. McGovern, D. R. Lloyd, A. Patchett, D. R. T. Zahn, T. Johal, and R. McGrath, Surf. Sci. **344**, 1 (1995).

[11] E. Dudzik, A. Leslie, E. O'Toole, I. T. McGovern, A. Patchett, D. R. T. Zahn, J. Ludecke, D. P. Woodruff and B. C. C. Cowie, J. Phys.: Condens. Matter **8**, 15 (1996).

[12] T. K. Johal, P. Finetti, V. R. Dhanak, A. W. Robinson, A. Patchett, D. R. T. Zahn, and R. McGrath, Appl. Surf. Sci. **104**, 257 (1996).

[13] G. J. Hughes, T. P. Humphreys and R. H. Williams, Vacuum **31**, 539 (1981).

[14] E. Dudzik, A. Leslie, E. O'Toole, I. T. McGovern, A. Patchett, and D. R. T. Zahn, Appl. Sur. Sci. **104/105**, 101 (1996).

[15] J. L. A. Alves, J. Hebenstreit, and M. Scheffler, Phys. Rev. B **44**, 6188 (1991).

[16] G. P. Srivastava, Rep. Prog. Phys. **60**, 561 (1997).

[17] G. Burns, *Solid State Physics*, International Edition, Acedemic Press, 1990.

[18] M. Çakmak, and G. P. Srivastava, Phys. Rev. B **56**, 1928 (1997).

[19] E. Schröder-Bergen and W. Arnke, Surf. Sci. **236**, 103 (1990).

[20] A. Umerski and G. P. Srivastava, Phys. Rev. B **51**, 2334 (1995).

[21] *Physics of Group IV and III-V Compounds*, Landolt-Börnstein, New Series, Group III, Vol. 17a (Springer, Berlin 1982).

[22] G. P. Srivastava, J. Phys.: Condens. Matter **5**, 4695 (1993).

Chapter 6

Adsorption of S on Si(001) and Ge(001)

6.1 Introduction

Group-IV semiconductor (001) substrates are of central importance in a variety of areas of current technological and scientific interest. The low temperature clean Si(001) and Ge(001) surface is understood to reconstruct to a c(4×2) phase consisting of alternately asymmetric dimers, while at room temperature the reconstruction becomes (2×1) [1, 2]. Atomic geometries and electronic structures of these surfaces have already been subject to intensive experimental [3, 4, 5, 6, 7] and theoretical efforts [8, 9, 10, 11, 12, 13, 14, 15, 16, 17].

Adsorption of adatoms can change the surface reconstruction in many ways by the formation of new bonds. Many works have been carried out for adsorption of group VI adatoms such as Se and S on the Si(001) surface. On the theoretical side, Kaxiras [18] and Krüger and Pollmann [19] suggest that adsorption of Se and S on Si(001) (2×1) can lead to the restoration of the ideal bulk terminated geometry of the semiconductor surface. On the experimental side, Moriarty *et al.* [20] have reported that room temperature adsorption of sulfur results in the formation of an overlayer with the underlying Si(001) substrate retaining the (2×1) reconstruction. They also found that, after having annealed at 325 °C, the sulfur overlayer desorbs, leaving the appearance of coexisting c(4×4) and (2×1) surface reconstruction.

The c(4×4) structure was proposed to consist of a missing-dimer defect, created by S during the desorption process. In a recent work, using AES, TDS, LEED and work function (WF) measurements, Papageorgopoulos *et al.* [21] have presented a thorough description of the location of S, the S-Si bonding, and desorption of S from the Si(001) surface. From their studies they suggest that the adsorption at room temperature leads to a (2×1) structure for half-monolayer coverage (hemisulfide structure) and the unreconstructed (1×1) structure for full monolayer coverage (monosulfide structure). For S coverage of two monolayers they have suggested the (1×1) structure with S embedded into the Si substrate. When annealing above 400°C, the top S layer desorbs drastically. At about 550°C the second-layer S is removed completely, leading back to the (2×1) reconstruction. Near 650°C the sulfur is completely desorbed from the silicon substrate. Using high-resolution core-level photoelectron spectroscopy and scanning tunnelling microscopy, Göthelid *et al.* [22] studied the adsorption and desorption of S on and off the Ge(001) surface. They observed the (2×1) and (1×1) structures at room temperature, with desorption taking place upon annealing. Similarly, using a number of experimental techniques, Anderson *et al.* [23] showed that at room temperature the S/Ge(001) system takes the (1×1) structure, with S lying in the bridge bonding site. Desorption of S is observed to take place between 460 and 750 K, while retaining the (1×1) structure of the clean surface.

In this chapter a detailed theoretical study of the atomic geometry, electronic structure and bonding for the hemisulfide, monosulfide and disulfide structures proposed by Papageorgopoulos *et al.* has been mainly provided for Si(001). The results are used to remark on the desorption of S from the Si(001) surface observed at elevated temperatures. Using an analysis of surface free energy, in the allowed range of S chemical potential, we find that the monosulfide structure is more stable than the hemisulfide and disulfide structures. The monosulfide case is also used to investigate for the Ge(001) substrate. The geometrical parameters and electronic band structure are compared with the available theoretical and experimental results.

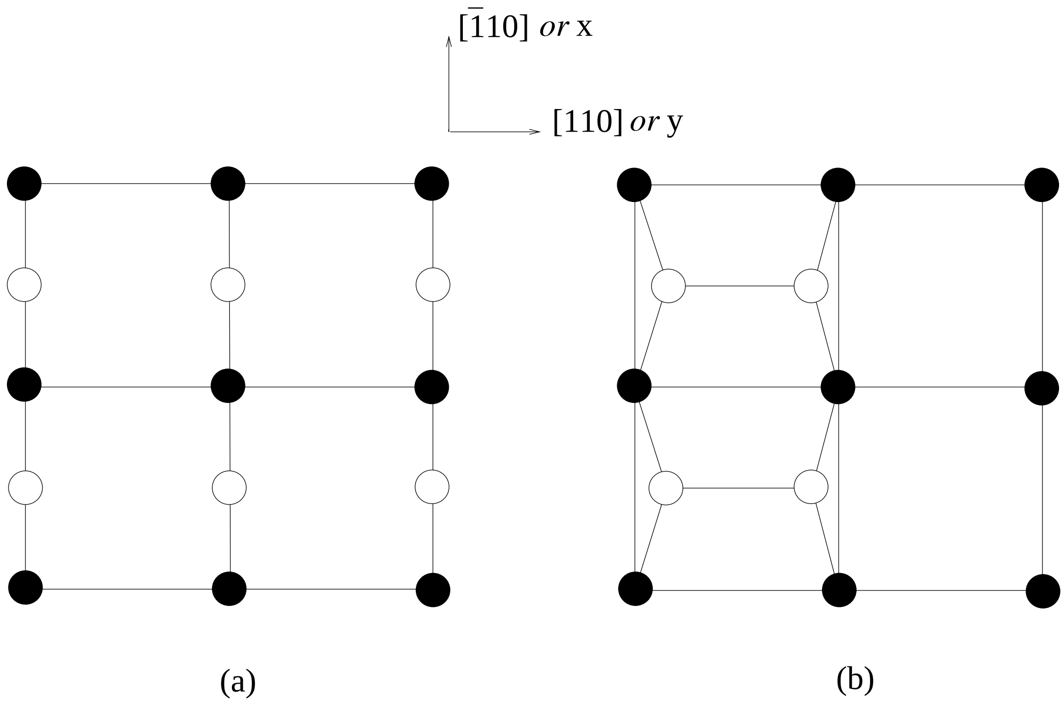

Figure 6.1: Top view of the outermost atomic layers of IV(001) for (a) the ideal bulk geometry, (b) the surface dimer model.

6.2 The Clean IV-(001)-(2×1) surfaces

Fig. 6.1 shows the ideal bulk model and the dimer model. At room temperature the clean Si(001) and Ge(001) surfaces exhibit a 2×1 reconstruction with the formation of tilted dimer atoms. The bond length is approximately 2.25 Å for Si [8] and 2.38 Å for Ge [9]. The dimer tilt angles are approximately 16° for Si [8] and 18.7° for Ge [9] as shown in Fig. 6.2. Experimental results for the dimer bond length lie in the range 2.20-2.47 Å for Si(001) and 2.41-2.44 Å for Ge(001). Theoretical results for dimer bond lengths lie in the range 2.25-2.30 Å for Si(001) and 2.36-2.46 Å for Ge(001). Recent works suggest that the dimer tilt angle is in the range 15-20° for Si(001) and 19-21° for Ge(001) (see e.g. [24, 25]).

The symmetric dimer model of the clean Si(001) and Ge(001) surfaces leads to π and π^* bands which overlap and the surfaces turn out to be metallic [11] as we have shown in Fig. 6.3 for the case of Si. For the asymmetric dimer, the higher-lying dimer component (D_u) is fully occupied with the associated electronic state close to the bulk valence band maximum, and the lower-lying dimer component (D_d) is empty corresponding to the energy state in the upper half of the bulk silicon and germanium band gaps. These are due to the two dangling-bond orbitals per dimer. On the other hand, adatoms can change the reconstruction of systems and lead to a new phase. This new phase again may reduce the total energy of the systems. Without discussing the clean Si(001) and Ge(001) surfaces in detail, the following sections show the effect of S adatom on Si(001) and Ge(001).

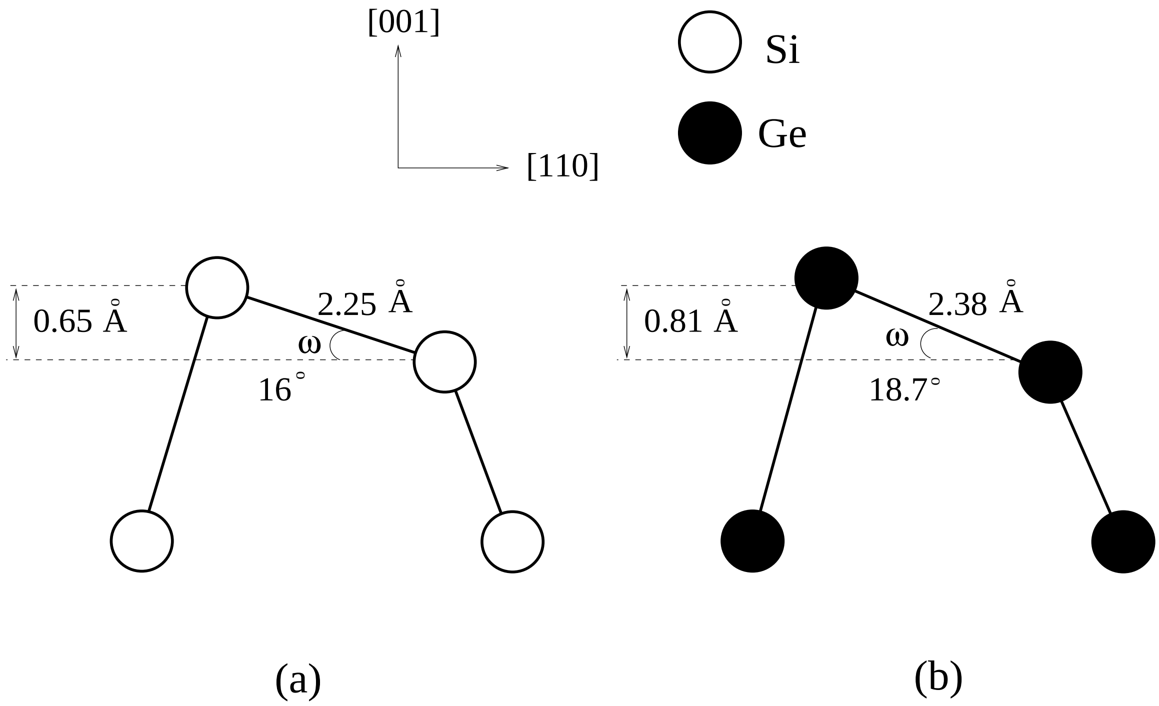

Figure 6.2: Schematic side view of the equilibrium geometries for the surface dimers at (a) the clean Si(001)-(2×1) and (b) the clean Ge(001)-(2×1) surface.

6.3 S adsorption on IV(001)

We consider an artificially constructed periodic geometry along the surface normal. The unit cell included an atomic slab with eight layers of Si (or Ge) substrates plus a vacuum region equivalent to about four Si (or Ge) layers in thickness. The two Si (or Ge) back layers were frozen into their bulk positions, and the back surface was saturated with two pseudo-hydrogen (H_{ps}) per Si (or Ge) atom. The first main advantage of using H_{ps} is saturation of dangling bonds. In this way, surface atoms

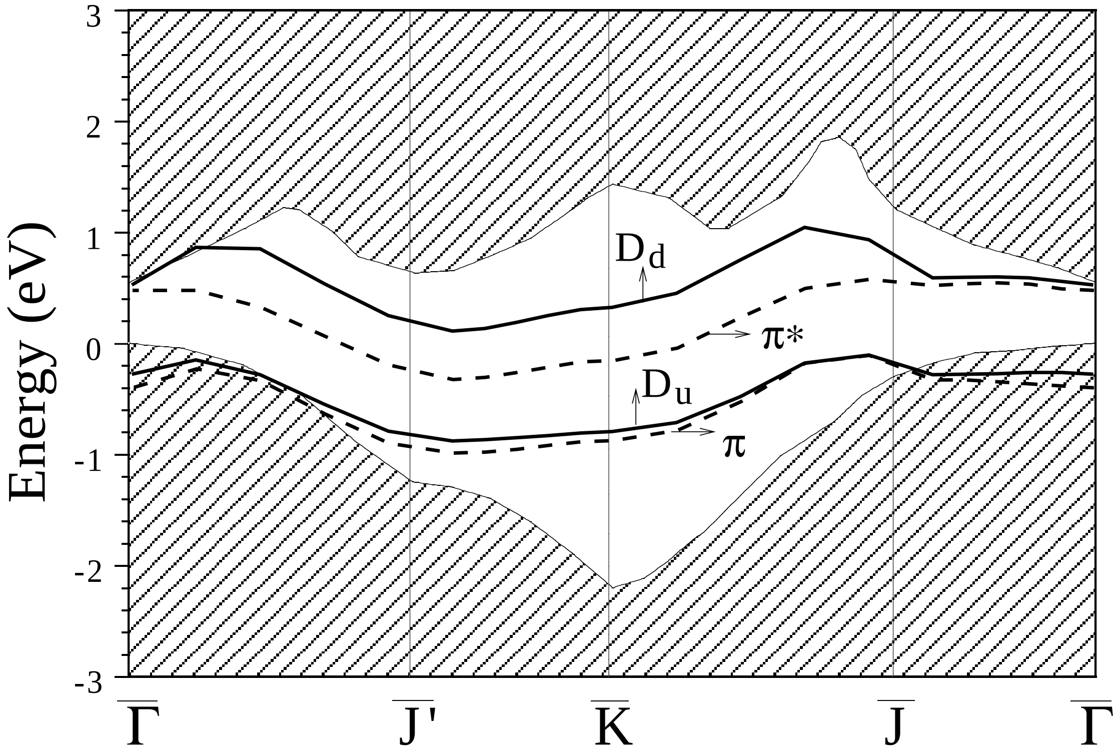

Figure 6.3: Surface states on Si(001)-(2 × 1). The dashes curves are symmetric dimer formation for the clean Si(001). The full curves are asymmetric dimer formation for the clean Si(001).

on the back side of the cell can be fixed at ideal bulk positions. All the remaining Si (or Ge) atoms, the S adatoms and the saturating H_{ps} atoms were allowed to relax into their minimum energy positions using a conjugate gradient method [26]. The calculated theoretical equilibrium lattice constant for bulk Si (5.42 Å) (or Ge (5.53 Å)) has been used in all the surface calculations.

6.3.1 Atomic geometries, Electronic states and Chemical bondings

6.3.1.1 Hemisulfide-Si(001)-(2×1)

As we have discussed earlier, it is well known that on the *clean* Si(001)-(2×1) surface the Si-dimer are tilted. If a constrained symmetric Si-dimers geometry is used for the *clean* surface, then the dimer is slighly shortened to a length of 2.20 Å [8]. For the half-monolayer coverage S atoms are placed on the bridge sites of the Si dimers,

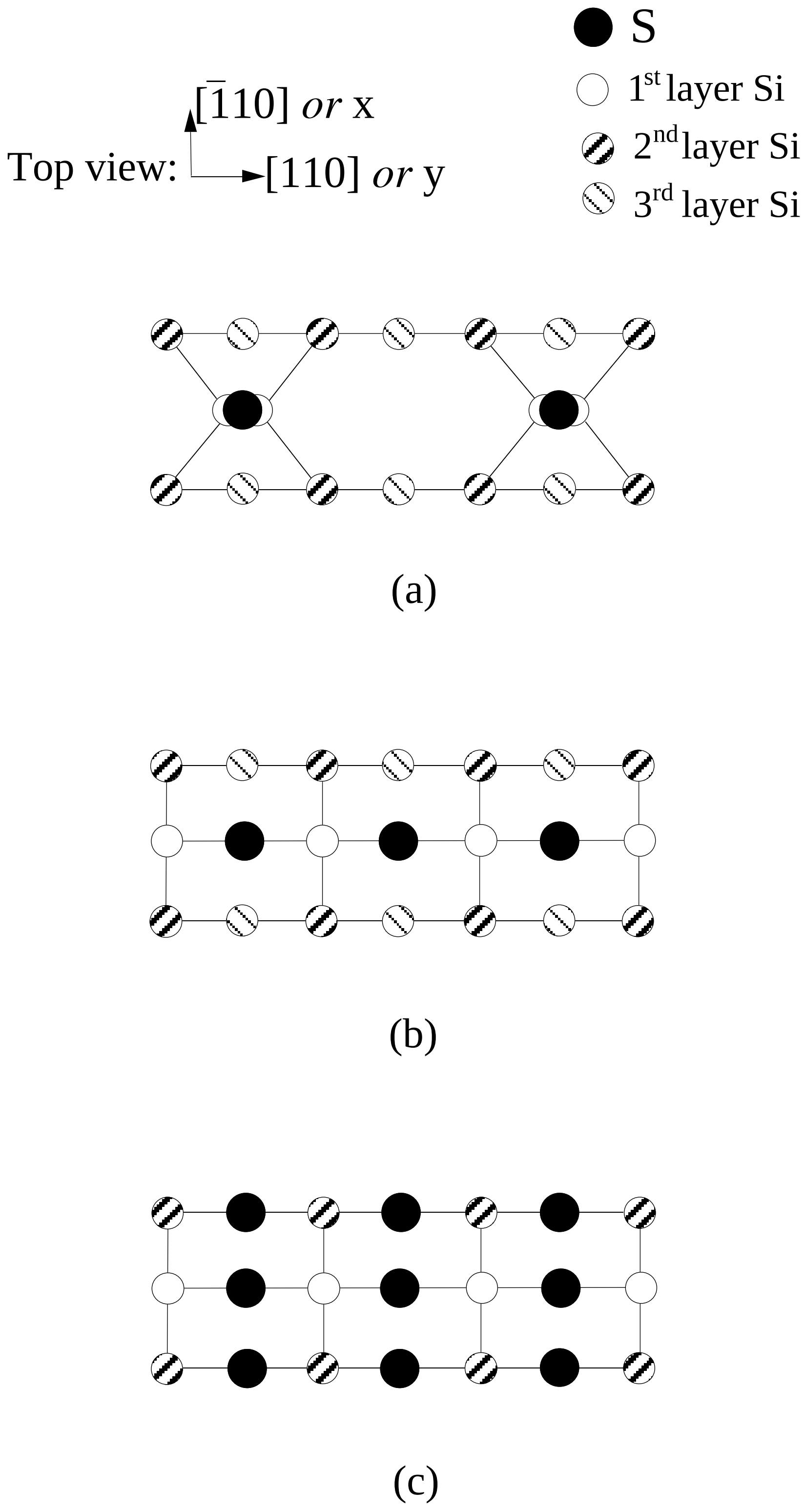

Figure 6.4: Schematic top view of S adsorption on the Si(001) surface, (a) the S-(2×1) (hemisulfide) structure on the Si(001)(2 × 1) surface, (b) the S-(1 × 1) (monosulfide) structure on the (1 × 1) surface, and (c) the S-(1 × 1) (disulfide) structure on the (1 × 1) surface: the first S atoms are bonded to the first layer Si atoms and the second S atoms are bonded to the second layer Si atoms.

with one adsorbate atom per (2×1) surface unit cell, as shown in Fig. 6.4(a). All the Si atoms are four-fold coordinated and the S atoms are two-fold coordinated. Upon adsorption, the Si dimer becomes symmetric and is slightly elongated to a length of 2.30 Å.

It should be pointed that in their measurements, Papageorgopoulos *et al.* [21] could not clearly ascertain the symmetric nature of the Si dimer in the hemisulfide state. From our calculations we find that for the hemisulfide structure there is significant atomic relaxation up to the fourth Si substrate layers. The Si dimer layer is relaxed inward by $\sim$0.2 Å with respect to the ideal bulk silicon position. The perpendicular distance between the Si dimer and the second-topmost Si layer is 1.12 Å shown in Fig. 6.5, which is nearly 18% shorter than the ideal bulk interlayer separation. The S-Si bond length is 2.17 Å, slightly smaller than the sum of the corresponding covalent radii. Similarly, the bond length between a Si dimer atom and its neighbour in the second substrate layer is 2.32 Å, again close to the silicon bulk bond length. The calculated perpendicular distance between the Si dimer and the S atom is 1.84 Å, in excellent agreement with the experimentally obtained value of 1.87 Å by Papageorgopoulos *et al.* [21]. The Si-S-Si bond angle is calculated to be 63.9°. The electronic band structure around the fundamental bad gap region and some charge density contour plots are shown in Figs. 6.6 and 6.7, respectively. By examining the total valence charge density plots in Figs. 6.7(a) and 6.7(b), it can be seen that the bonds between Si dimer atoms, as well as between the dimer and substrate atoms, are somewhat stronger than the Si-Si bond in the bulk region, consistent with their relative bond lengths. The S-Si bonding can be called polar covalent, with a large degree of covalency and some ionic character (the maximum charge density in the S-Si bond is closer to the S atom, as seen in Fig. 6.7(a)). This indicates that the Si end is slightly positively charged and the S end is slightly negatively charged. A similar feature exists in C-O, another IV-VI bond. On the other hand, throughout the structure the Si-Si bonding is purely covalent in character.

The hemisulfide structure results in just one occupied surface state in the band gap region of silicon. In order to understand this state we first recall again that on the clean Si(001)-(2×1) surface with a symmetric dimer there are two overlapping

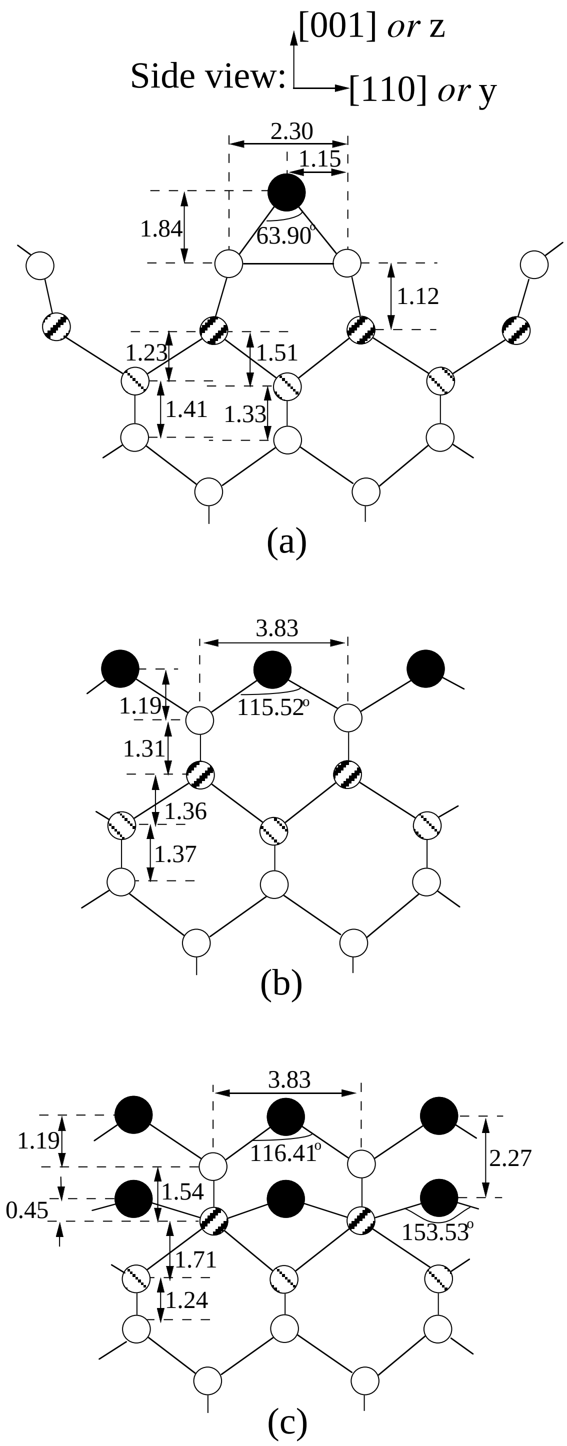

Figure 6.5: Schematic side view of relaxed geometries of (a) hemisulfide Si(001)-(2 $\times$ 1), (b) monosulfide Si(001)-(1 $\times$ 1), and (c) disulfide Si(001)-(1 $\times$ 1).

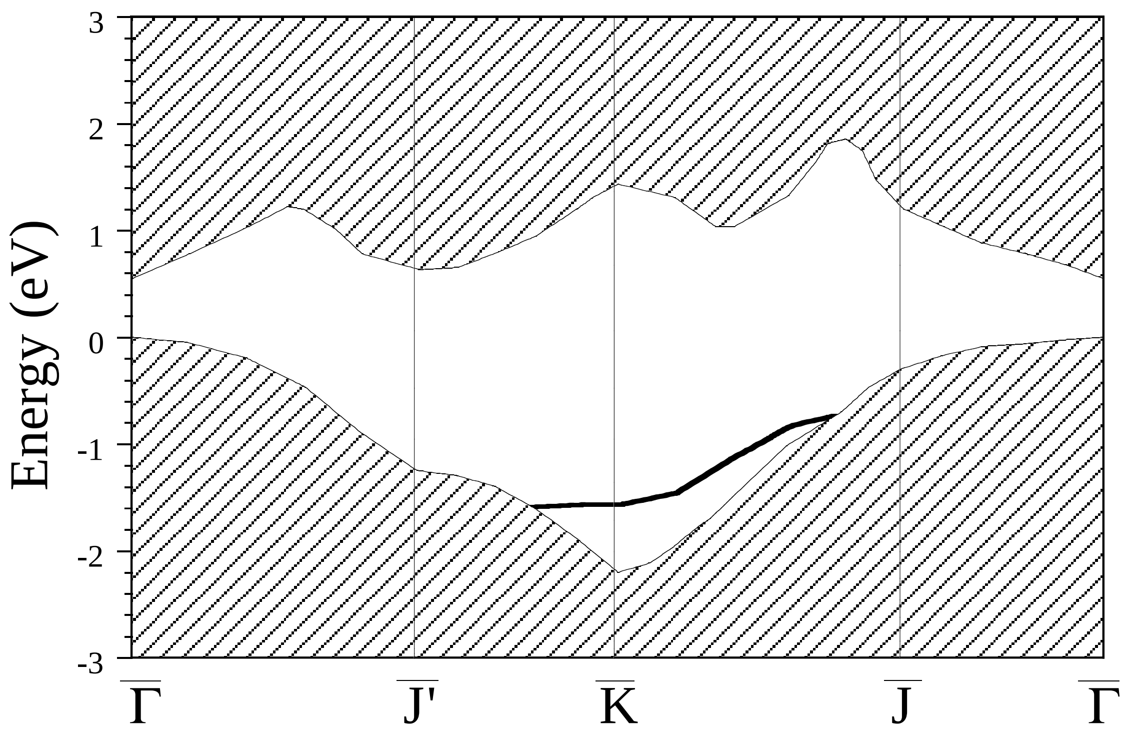

Figure 6.6: Electronic band structure of hemisulfide Si(001)-(2×1) structure. The shadded region is the bulk (2×1) projected band structure for Si, the thick line is the occupied surface band.

π-derived dangling bond states as shown in Fig. 6.3 (see Sect. 6.2): these can be labelled π and π^* according to their orbital symmetries. Both of these are partially occupied, making the surface metallic. Upon adsorption in the hemisulfide geometry, both of these states hybridize with the p_z orbital of sulfur, get fully occupied and their energies are lowered. Only the state with the orbital character p_z^{S}-π^{Si} now lies just above the silicon valence band edge. The orbital character of this state is shown in Fig. 6.7(c).

6.3.1.2 Monosulfide-Si(001)-(1×1)

The LEED, AES, TDS and WF studies by Papageorgopoulos *et al.* [21] suggest that increasing the S coverage from half-monolayer (0.5 ML) to full-monolayer (1 ML) changes the (2×1) surface reconstruction to (1×1), maintaining fourfold coordination of all the Si atoms and twofold coordination of the S atoms, with S atoms sitting above the topmost Si atoms in bridge adsorption sites, as shown

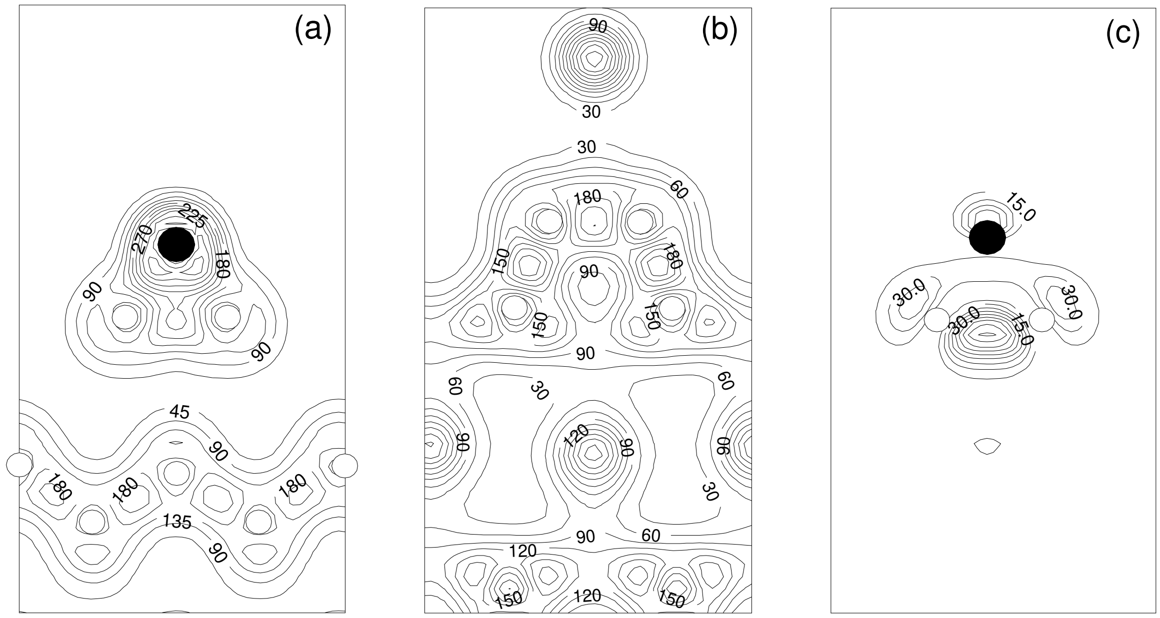

Figure 6.7: Electronic total charge density and electronic charge density plots of the individual state for hemisulfide Si(001)-(2×1) structure. (a) On the plane cutting vertically through the Si atoms with S (Plane 1), and (b) on the plane cutting obliquely through the Si atoms so as to include the S-Si bonds (Plane 2). (c) The highest occupied surface state at $\bar{K}$, shown in Plane 1. The electron charge density is normalised to the number of electrons in the supercell (i.e. 74 electrons per unit cell for total charge density plots and 2 electrons per unit cell for the individual electronic states).

in Figs. 6.4(b) and 6.5(b). On the theoretical side Krüger and Pollmann [19] carried out energy minimization for the 1 ML coverage based on the local density approximation, norm-conserving pseudopotentials, Gaussian orbitals basis, and by employing Green's function scattering method. Starting with several geometries within the (2×1) symmetry, they concluded that the (1×1) was the equilibrium configuration with S adsorbed in bridge positions. Following the above mentioned experimental and theoretical works, we studied the S(1 ML)/Si(001)-(1×1) system and found that this system is characterized by only small atomic relaxation extending up to the third Si substrate layer. With respect to the bulk-terminated Si layers, the S and top two Si layers have relaxed along the surface normal by -0.15 Å, +0.02 Å and +0.07 Å, respectively. These values are in good agreement with the results obtained by Krüger and Pollmann. The vertical height of the S atom from the top substrate layer has decreased from 1.84 Å for 0.5 ML to 1.19 Å for 1 ML. Our calculated value of 1.19 Å is in excellent agreement with the experimental value of 1.09 Å [21]. The relaxed S-Si bond length is 2.26 Å, and the Si-S-Si bond angle is 115.5°. These values are in very good agreement with the results obtained by Kaxiras [18] who used a theoretical method similar to ours. The Si-Si bond lengths have been restored to the bulk value.

A band gap of around 0.45 eV at $\bar{\Gamma}$ is calculated. Two occupied electronic states (S_1 and S_2) and one unoccupied electronic state (S_3) in the gap between the valence and conduction bands have been identified, shown in Fig. 6.8. Similarly positioned surface states were calculated by Krüger and Pollmann for Se/Si(001) and by Kaxiras for S/Si(001). The total and partial charge density plots for S(1 ML)/Si(001)-(1×1) have been shown in Fig. 6.9. Fig. 6.9(a), plotted on the plane cutting vertically through the S atom and the first-topmost Si layer, reveals that the S-Si bond is polar covalent: with a large degree of covalency and with some ionic character, giving rise to a shift in the peak towards the more electronegative species S. This is entirely consistent with the chemical shift observed in the work of Papageorgopoulos *et al.*, which shows strong interaction between S and Si with a covalent bond character. As seen in Figs. 6.9(b) and (d), the state S_1 is primarily derived from the p_z orbital of the S atom, and S_3 can be considered as the related antibonding state. The highest occupied state S_2, plotted on a horizontal plane and shown in Fig. 6.9(c), is derived from the lone-pair orbitals p_y of the S atom. There is evidence of a small overlap of these orbitals between neighbouring S atoms. Similar orbital characteristics for the three states S_1, S_2 and S_3 have been presented by Krüger and Pollmann [19] for Se/Si(001) and by Rohlfing *et al.* [27] for S/Ge(001).

6.3.1.3 Disulfide-Si(001)-(1×1)

The Si(001) surface with 2 ML coverage of S may not be as ideally coordinated as the 1 ML covered surface. Indeed Kaxiras [18] has shown that S(1ML)/Si(001) is stable against structural changes such as embedding of the adsorbates in subsurface sites. However, the experimental work by Papageorgopoulos *et al.* [21] clearly

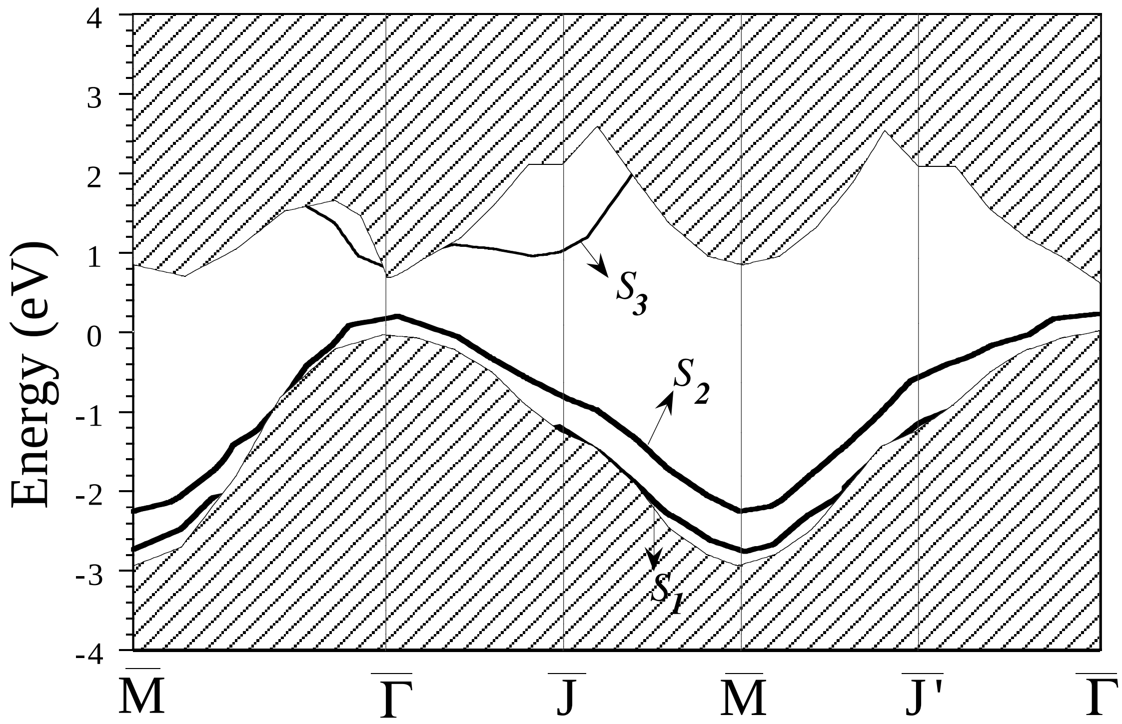

Figure 6.8: Electronic band structure of the S(1 ML)-Si(001)-(1 × 1) structure. The shadded region is the bulk (1 × 1) projected band structure for Si, the thick lines are the occupied surface bands and the thin line the unoccupied band.

demonstrates that at room temperature coverage above 1 ML sulfur is embedded into the Si bulk near the surface. The sticking coefficient of S on the surface is unity for the first 2 ML coverages. These authors have called the 2 ML embedded structure as *disulfide* state, characterized by strong covalent S-Si bonds. This structure is shown in Fig. 6.4(c).

From our calculations we find that the disulfide structure results in a metallic band structure and in significant bonding changes between the overlayer and the substrate. As opposed to the hemisulfide and monosulfide structures, for the disulfide structure the Si substrate experiences significant atomic relaxation up to the sixth layer. In particular, relative to the Si bulk terminated sites, the top S layer has relaxed upwards by 0.28 Å and the top Si layer has relaxed downwards by 0.20 Å. The vertical height between the top-layer S and the top-layer Si is 1.19 Å, as shown in Fig. 6.5(c). This value is the same as obtained for the 1 ML coverage. The vertical height between the top two Si layers has expanded from 1.31 Å for the

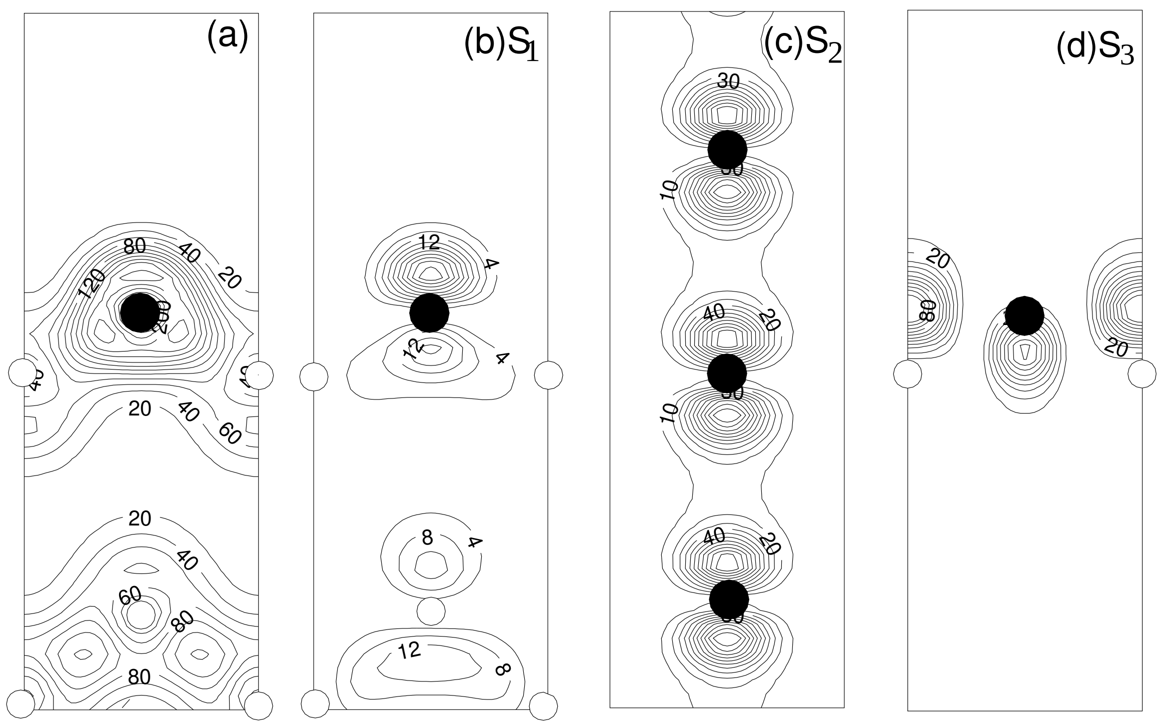

Figure 6.9: Electronic total charge density and electronic charge density plots of the individual states for the S(1 ML)-Si(001)-(1 × 1) structure. (a) On the plane cutting vertically through the Si atoms with S (Plane 1), (b) the surface state S_1 for Plane 1 at $\bar{K}$, (c) the surface state S_2 at $\bar{K}$, on the plane cutting horizontally through the S atoms so as to included the S and the next S neighbors, and (d) the unoccupied surface state S_3 for Plane 1 at $\bar{J}$. The electron charge density is normalised to the number of electrons in the supercell (i.e. 40 electrons per unit cell for total charge density plots and 2 electrons per unit cell for the individual electronic states).

monosulfide structure to 1.54 Å. The expanded vertical height is accompanied by an enlarged bond length of 2.46 Å, signifying weakening of this Si-Si bond. The vertical height between the embedded sulfur and the second-layer Si atoms is 0.45 Å. While the bond length between the top-layer S and Si is the same as in the monosulfide case (viz. 2.26 Å), the bond length between the embedded S and the second-layer Si is much shorter at 1.97 Å. This suggests that the embedded S is more strongly bonded to the substrate than is the top-layer S. This favours the formation of SiS molecules suggested in the work of Papageorgopoulos *et al.*

The bonding characteristics of the top-layer and embedded S atoms are shown in Figs. 6.10(a) and (b), respectively. The bonding between the top-layer S and its neighbouring Si is polar covalent, as in the hemi- and monosulfide cases. The

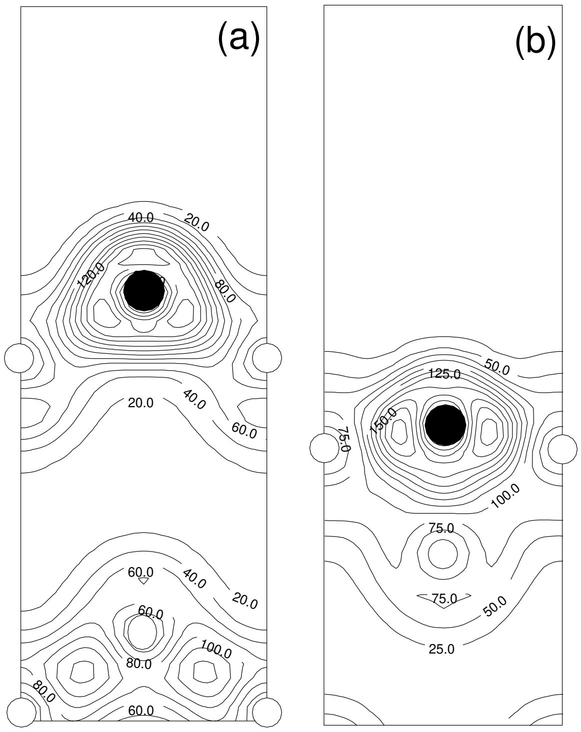

Figure 6.10: Electronic total charge density plots for the S(2 ML)-Si(001)-(1×1) structure. (a) On the plane cutting vertically through the Si atoms with S, and (b) on the plane cutting obliquely through the Si atoms with embedded the S atom. The electron charge density is normalised to the number of electrons in the supercell (i.e. 46 electrons per unit cell).

bonding between the embedded S and its neighbouring Si is slightly more covalent than the previously mentioned bond. Having formed two strong covalent bonds with the neighbouring Si atoms in the second substrate layer, the divalent embedded S does not form a clear bonding with the third-layer Si despite being at a reasonable distance of 2.16 Å. Also, the original covalent bonding between the second- and third-layer Si atoms has been substantially weakened, and the vertical interlayer distance has increased to 1.71 Å. This weakening of Si-Si bonding is in direct agreement with the suggestion forwarded by Papageorgopoulos *et al.* [21] who observed complete desorption of both the top- and second-layer S upon heating the system near 650°C. We suggest that the desorption takes place in the form of the system comprised of the two layers of S and the top two layers of Si, containing strongly bonded SiS units. The remaining substrate may then result in (2×1) or c(4×2) reconstruction, as observed on clean Si(001) surfaces [25]. In the event of incomplete desorption, especially at lower than 400°C, the remaining S may induce (2×1) or $c(4 \times 4)$ reconstructions as observed by Moriarty *et al.* [20].

6.3.2 Relative stability of hemi-, mono- and disulfide phases

The stable surface reconstruction is the one with the lowest surface energy. Total energies for different structures can only be compared when the structures share the same stoichiometries. However, non-stoichiometric surfaces can be considered by allowing the surface to exchange atoms with a reservoir, which is characterised by a chemical potential [28]. As the hemi-, mono- and disulfide phases share different stoichiometries, their relative energetic stabilities can be studied by examining the free energy of each system.

In our case, due to the varying numbers of S and Si atoms per unit cell the comparison of the total energy for the different adsorption configurations considered here has to take into account the chemical potentials of the respective species. The surface free energy of a supercell may be written as

$$F = E - \sum_i n_i \mu_i \tag{6.1}$$

where n_i is the number of atoms and μ_i is the chemical potential of the i^{th} species. The total energy of the supercell, E, is taken from our *ab initio* calculations. Since the Si atoms at the surface must be in equilibrium with the bulk, μ_{Si} must equal $\mu_{\mathrm{Si}}^{\mathrm{bulk}}$, so we have

$$F = E' - n_{\mathrm{S}} \mu_{\mathrm{S}} \tag{6.2}$$

where E'=E-$n_{\mathrm{Si}}\mu_{\mathrm{Si}}^{\mathrm{bulk}}$ is a constant for a chosen structure. Thus the free energy of the system can be considered to vary linearly with the surface chemical potential μ_{S} of sulfur.

To be entirely consistent with respect to numerical details, we calculated the bulk Si chemical potential using the same size supercell and the same number of special **k**-points as described in Sect. II. The S chemical potential should be considered with the constraint $\mu_{\mathrm{S}} - \mu_{\mathrm{S}}^{\mathrm{bulk}} \leq 0$, where $\mu_{\mathrm{S}}^{\mathrm{bulk}}$ is the bulk S chemical potential. We have considered a reasonable range for $\mu_{\mathrm{S}} - \mu_{\mathrm{S}}^{\mathrm{bulk}}$, with $\mu_{\mathrm{S}}^{\mathrm{bulk}}$ considered as follows.

In solid phase S takes different structures, such as ordinary rhombic with 128 atoms/cell, pseudocell rhombic with 32 atoms/cell, monoclinic with 48 atoms/cell, and hexagonal with 18 atoms/cell [29]. This poses a major computational difficulty in calculating the energy of bulk S in our calculation. Two thermodynamically stable forms of sulfur were considered: the S_2 molecule which is stable in high-temperature gas phase [30], and the *cyclo*-S_8 molecule with bulk-like three-dimensional crown ring structure shown in Fig. 6.11. We modelled both forms inside a repeated cubic box of size 15 Å. The structures were relaxed towards their minimum energy configuration by using four special **k** points.

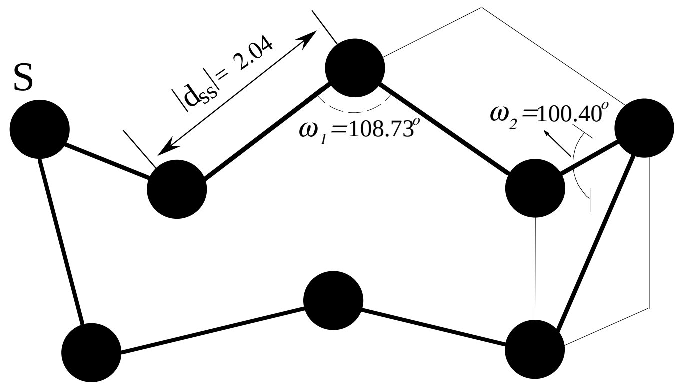

Figure 6.11: Schematic representation of the S_8 ring. ω_1 is the S-S-S angle, and ω_2 is the dihedral angle between successive SSS planes. Calculated structural parameters are in anstromgs (Å) and degrees.

For S_2 the relaxed bond length is 1.92 Å, in good agreement with the experimental value 1.89 Å [30]. The corresponding total energy is -19.919 Ry per atom. For S_8, the S-S-S angle is expected to be around ω_1=108^o and the chain is a zig-zag [30]. In our *ab initio* calculations, we find this angle as ω_1=108.73^o. The dihedral angle between successive SSS planes (see Fig. 6.11) is proposed to be ω_2=98.30^o [30], while we find that to be 100.40^o. Moreover, the S-S bond length minimises the energy to -19.997 Ry at 2.04 Å which is in excellent agreement with the proposed value of 2.06 Å [30]. If we arranged the S_8 sub-units in a different pattern (such as the ordinary rhombic structure) then we might also get a lower total energy. The calculated energy is almost certainly higher than the true energy, but the weak van der Waals S_8-S_8 interaction in the three-dimensional structure means that this overestimate should be small. Based upon these results, we have considered the value of $\mu_{\rm S}$ not to exceed $\mu_{\rm S_8}$ (which is shown as the limiting case in Fig. 6.12.). In other words, our estimate for $\mu_{\rm S}^{\rm bulk}$ is $\mu_{\rm S_8}$.

We performed calculations for the 2×1 surfaces with 0, 0.5 (hemisulfide), 1 (monosulfide) and 2 ML (disulfide) coverages of S on Si(001). The free energy F as a function of $\mu_{\rm S} - \mu_{\rm S}^{\rm bulk}$ in the range 0.0 to -3.5 eV has been plotted in Fig. 6.12. It is clear that the disulfide phase is never the lowest energy phase at any accessible S chemical potential. For $\mu_{\rm S} - \mu_{\rm S}^{\rm bulk} < -2.43$ eV (i.e. in the S poor limit) the clean Si(001) surface is energetically favourable, which also indicates that any S present will tend to form islands. For $\mu_{\rm S} - \mu_{\rm S}^{\rm bulk} > -2.43$ eV the monosulfide phase is favourable. There is never a situation when it is favourable for S to spread out evenly across the surface in a uniform hemisulfide phase. This seems just as interesting a results to us thermodynamically as to disallow the disulfide phase. The thermodynamic instability of the disulfide phase is consistent with the above mentioned experimental observation and the theoretical discussion about SiS desorption.

6.4 S adsorption on Ge(001)

6.4.1 Atomic geometries, Electronic states and Chemical bondings

For the passivation of the Ge(001) surface by sulphur, two adsorption geometries have been proposed. In the hemi-sulfide case S atoms are placed on top of each dimer, breaking the dimer bond and building chemical bonds with the former dimer atoms. But only one-half of the possible surface sites are occupied by adatoms. By adsorption of a full monolayer of sulphur the surface structure changes into a (1×1) geometry. This can be achived by exposing the clean Ge(001) surface to atomic sulphur [31] or to an aqueous $(NH_4)_2S$ solution [32]. Consideration of the experimental works [31, 33] and our previous theoretical results on a Si(001) substrate has motivated us to study monosulfide on Ge(001) system (see Fig. 6.4(b)).

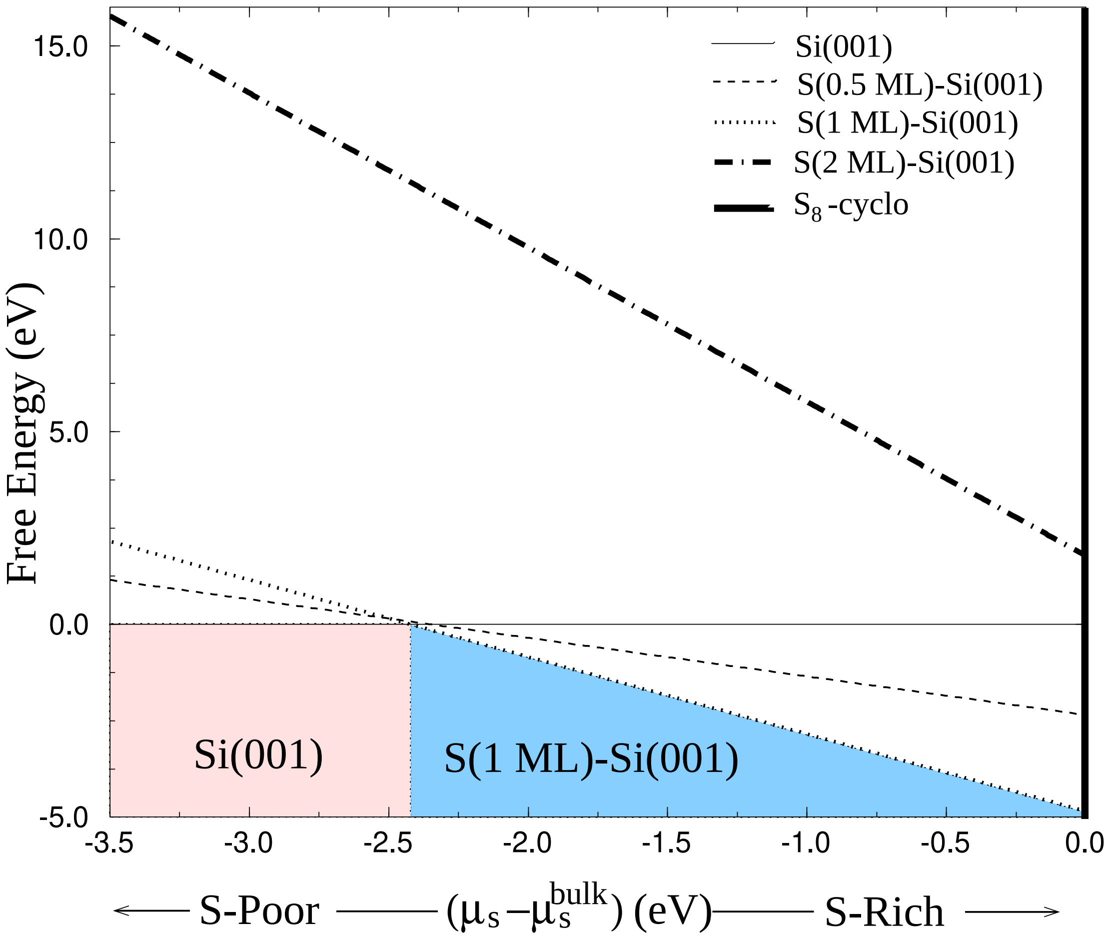

Figure 6.12: Surface free energy of S/Si(001)-(2 × 1) plotted against $\mu_{\rm S} - \mu_{\rm S}^{\rm bulk}$.

6.4.1.1 Monosulfide-Ge(001)-(1 × 1)

Calculations for this system have been made using the procedure discussed in Sec.6.3. All atomic relaxations are found to be very small. Thus the atomic structure of the adsorbate system is nearly identical to that of an ideal clean Ge(001)-(1 × 1). The calculated bond length between S and the neighbouring Ge atom is 2.30 Å, which is only 2% bigger than the sum of their corresponding covalent radii ($r_{\rm Ge-S}$=2.26 Å). This value is in excellent agreement with the photoemission fine structure measurement [34] and surface-extended x-ray-absorption fine-structure data by Newstead *et al.* [35] who found a value of 2.36 ± 0.05 Å for the S-Ge bond length in the case of the S (0.5 ML)/Ge(001)-(2 × 1) surface (hemisulfide).

We have identified a total of six occupied and the lowest one unoccupied electron

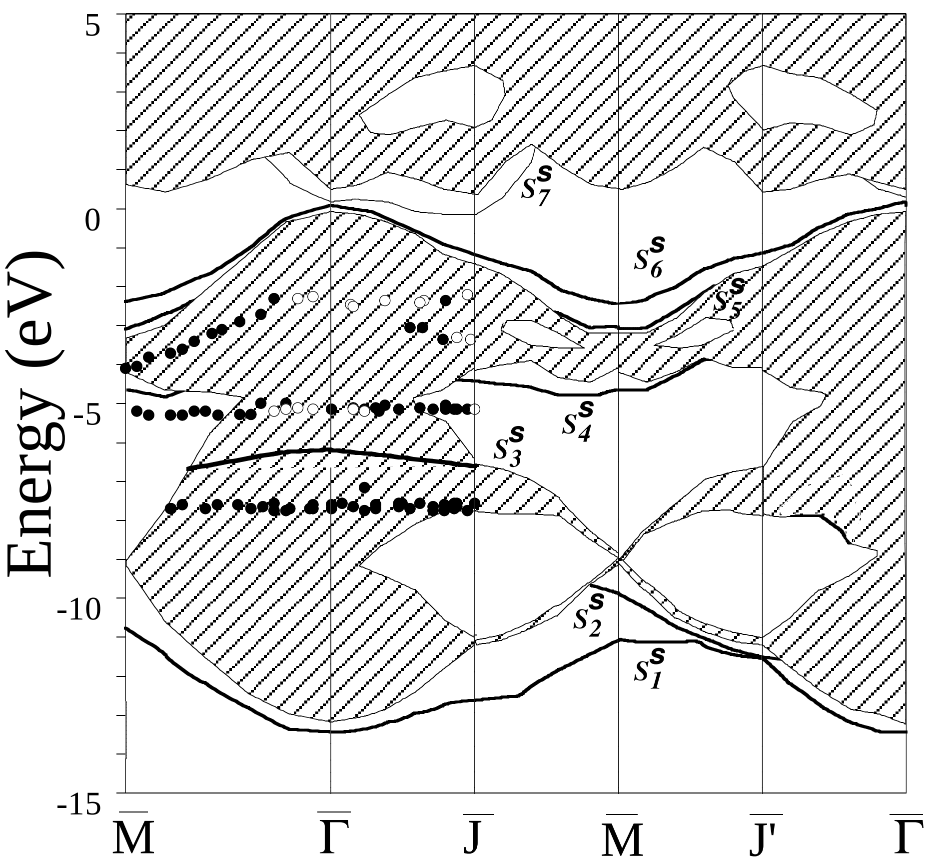

Figure 6.13: Calculated band structure of the 1 ML S coverage on the Ge(001)-(1×1) surface. The shaded region is the bulk (1×1) projected band structure for Ge and the thick lines represent the occupied surface bands and thin line is the lowest unoccupied surface bands. Full circles represents sharp and open circles weak feature in the ARPES spectra [33].

states, labelled S_1-S_7, as shown in Fig. 6.13. These are compared with the ARPES data by Weser *et al.* [33] (full symbols denote clear and empty symbols denote less clear spectral structures). They have observed three bands along the $\bar{M}$-$\bar{\Gamma}$-$\bar{J}$ high symmetry line that are to be compared with the calculated bands S_5, S_4 and S_3. The calculated dispersion of the S_3 and S_4 states is very similar to the experimental measurement, i.e. quite flat. However, the experimental results appear to show a constant downward shift compared to our calculations.

By examining the total valence charge density, shown in Fig. 6.14(a), the S-Ge bonding can be called polar covalent with a large degree of covalency and some ionic character. The maximum charge density in the S-Ge bond is closer to the S atom. It is also well-known that S-Ge compounds have covalent bonding character

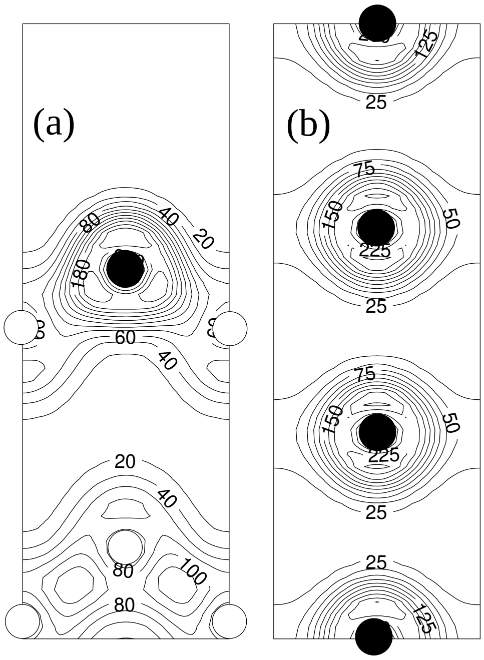

Figure 6.14: Electronic total charge density for monosulfide Ge(001)-(1 × 1) structure. (a) On the plane cutting vertically through the Ge atoms with S (Plane 1), and (b) on the plane cutting horizantally through the S atoms so as to included the S and the next S neighbors (Plane 2). The electron charge density is normalised to the number of electrons in the supercell (i.e. 40 electrons per unitcell for total charge density plots).

[31, 33]. The state S_1 is due to the *s*-orbital of the S atoms as seen in Fig. 6.15(a). The state S_2 is mainly due to a back bond between S and Ge. The state S_3 resonates with bulk. It is mainly anti-bonding between S and Ge and some contribution from the bulk Ge atoms as seen in Fig. 6.15(c). The state S_4 is mainly contributed from the p_y-orbital of the S atom and p_z-orbitals of neighboring Ge atoms as seen in Fig. 6.15(d). The second highest occupied state S_5 is due to the p_z-orbital of S. The highest surface state S_6 consists of the p lone-pair orbitals of the S atom, which is in agreement with the ARUPS results by Weser *et al.* [33] and the theoretical LCAO calculation by Ling *et al.* [36]. The unoccupied state, S_7, is formed by the p_z-orbital of the S atom and of the neighbouring Ge atom. There is a band gap, 0.16 eV at $\bar{\Gamma}$, between the highest occupied state and the lowest unoccupied state.

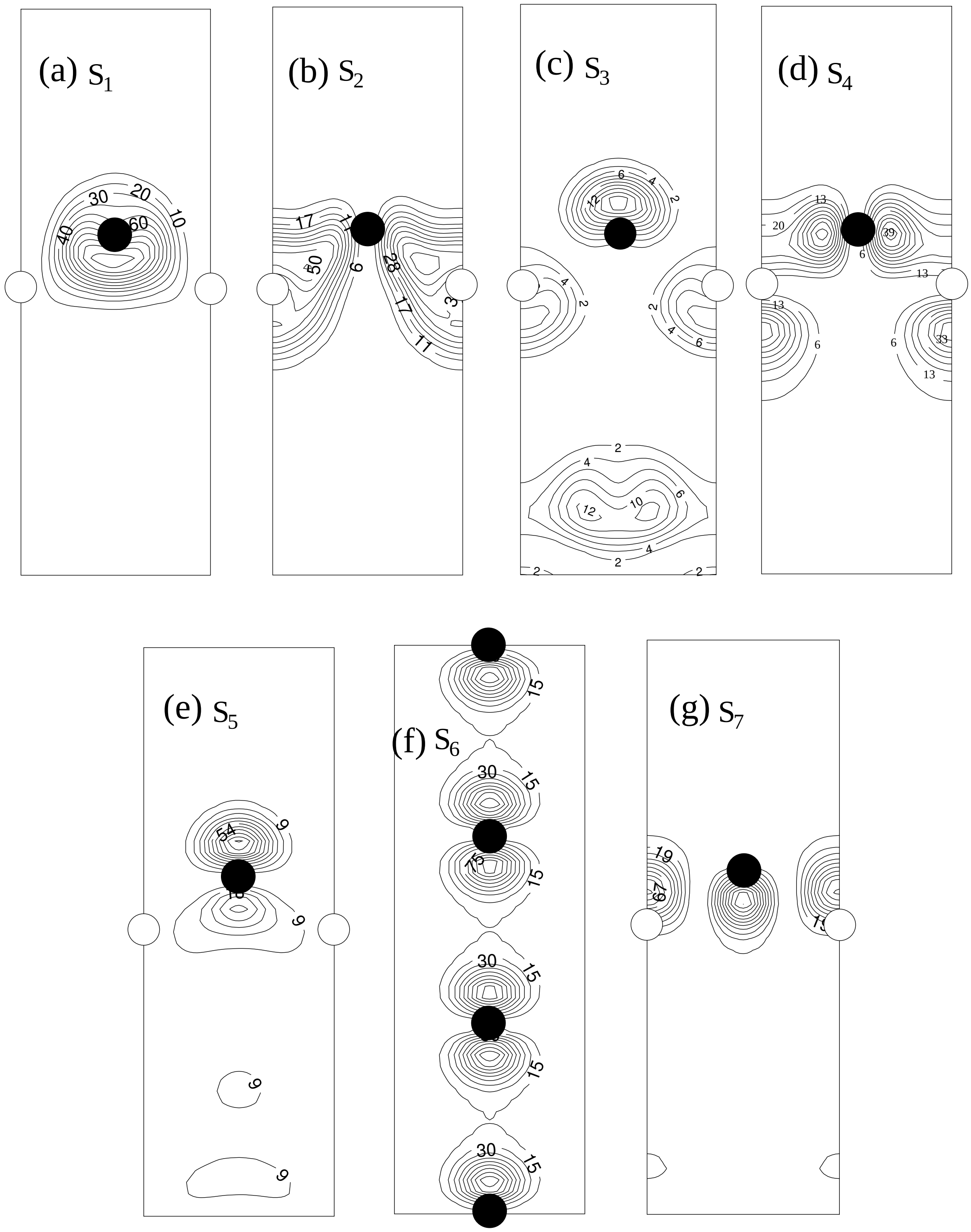

Figure 6.15: Electronic charge density plots of the individual states for the 1 ML S on the Si(001)-(1×2) surface: on the plane cutting vertically through the S atom and the Si atoms, (a) the surface state S_1^s at $\bar{M}$, (b) the surface state S_2^s at $\bar{M}$, (c) the surface state S_3^s at $\bar{\Gamma}$ and (d) the surface state S_4^s at $\bar{M}$, (e) surface state S_5^s at $\bar{M}$, on the plane cutting horizontally through the S atoms and the H atoms, (f) the surface state S_6^s at $\bar{M}$ and (g) the lowest unoccupied surface state S_7^s at $\bar{M}$. The electron charge density is normalised to the number of electrons (i.e. 2 electrons per unit cell for the individual electronic states).

6.5 Summary

In this chapter we have presented a detailed investigation of the atomic structure, bonding and the relative energetic stability of the hemi-, mono- and disulfide adsorption phases on Si(001). The results for the hemisulfide structure are in excellent agreement with experiment. The results for the monosulfide structure are also in excellent agreement with experiment and previous other theoretical studies. In the disulfide phase there is a polar covalent bonding between the top-layer S and the top-layer Si substrate, similar to that found for the hemi- and monosulfide structures. The disulfide structure is, however, characterized by strong covalent bonds between the second-layer S and the second-layer Si substrate. This is accompanied by a substantial weakening of the covalent bond between the Si atoms in the second and third substrate layers. We suggest that this weaking of the interlayer Si-Si bonding in favour of the formation of SiS units provides a signature of sulfur desorption seen in experiment. An analysis of surface free energy suggests that, in the allowed range of S chemical potential, the monosulfide structure is more stable than the hemisulfide and disulfide structures.

We have also studied 1 ML sulphur on the Ge(001)-(1×1) surface. Our calculated geometrical parameters have been compared with avaliable experimental and other theoretical results. Our calculated surface states are in good agreement with the ARUPS data.

Bibliography

[1] S. Ferrer, X. Torrelles, V. H. Etgens, H. A. van der Vegt, and P. Fajardo, Phys. Rev. Lett. **75**, 1771 (1995).

[2] D. Badt, H. Wengelnik, and H. Neddermeyer, J. Vac. Sci. Technol. B **12**, 2015 (1994).

[3] M. Takahasi, S. Nakatani, Y. Ito, T. Takahashi, X.W. Zhang and M. Ando, Surf. Sci. **338**, L846 (1995).

[4] E.L. Bullock, R. Gunnella, L. Patthey, T. Abukawa, S. Kono, C. R. Natoli and L.S.O. Johansson, Phys. Rev. Lett. **74**, 2756 (1995).

[5] L. Kipp, R. Manzke and M. Skibowski, Solid State Commun. **93**, 603 (1995).

[6] R. Rossmann, H. L. Meyerheim, V. Jahns, J. Wever, W. Mortiz, D. Wolf, D. Dornisch and H. Schultz, Surf. Sci. **279**, 199 (1992).

[7] R. J. Culbertson, Y. Kuk and L. C. Feldman, Surf. Sci. **167**, 127 (1986).

[8] H. M. Tütüncü, S. J. Jenkins and G. P. Srivastava, Phys. Rev. B **56**, 4656 (1997).

[9] H. M. Tütüncü, S. J. Jenkins and G. P. Srivastava, Phys. Rev. B **57**, 4649 (1998).

[10] J-H. Cho, S. Jeong, and M-H. Kang, Phys. Rev. B**50**, 17139 (1994).

[11] P. Krüger and J. Pollmann, Phys. Rev. Lett. **74**, 1155 (1995).

[12] M. Needels, M. C. Payne and J. D. Joannopoulous, Phys. Rev. Lett. **58**, 1765 (1987).

[13] S. J. Jenkins and G. P. Srivastava, J. Phys.: Condens. Matter **8**, 6641 (1996).

[14] J. Dabrowski and M. Scheffler, Appl. Surf. Sci. **56**, 15 (1992).

[15] J.E. Northrup, Phys. Rev. B **47**, 10032 (1993).

[16] N. Roberts and R.J. Needs, Surf. Sci. **236**, 112 (1990).

[17] M.T. Yin and M.L. Cohen, Phys. Rev. B **24**, 2303 (1981).

[18] E. Kaxiras, Phys. Rev. B **43**, 6824 (1991).

[19] P. Krüger and J. Pollman, Phys. Rev. B **47**, 1898 (1993).

[20] P. Moriarty, L. Koenders, and G. Hughes, Phys. Rev. B **47**, 15950 (1993).

[21] A. Papageorgopoulos, A. Corner. M. Kamaratos, and C. A. Papageorgopoulos, Phys. Rev. B **55**, 4435 (1997).

[22] M. Göthelid, G. LeLay, C. Wigren, M. Björkqvist, M. Rad, U. O. Karlsson, Appl. Sur. Sci. **115**, 87 (1997).

[23] G. W. Anderson, M. C. Hanf, P. R. Norton, Z. H. Lu, and M. J. Graham, Appl. Phys. Lett. **66**, 1123 (1994).

[24] S. J. Jenkins and G. P. Srivastava, Sur. Sci. **352-354**, 411 (1996).

[25] G. P. Srivastava, Rep. Prog. Phys. **60**, 561 (1997).

[26] A. Umerski and G. P. Srivastava, Phys. Rev. B **51**, 2334 (1995).

[27] M. Rohlfing, P. Krüger, and J. Pollmann, Phys. Rev. B **54**, 13759 (1996).

[28] G.-X. Qian, R. M. Martin and D. J. Chadi, Phys. Rev. B **38**, 7649 (1988).

[29] R. W. G. Wyckoff, *Crystal Structures*, Vol.1. Interscience Publ., New York, 1960.

[30] K. M. Mackay and R. A. Mackay, *Introduction to Modern Inorganic Chemistry*, 3rd ed. Int. Textbook Company, London, 1981.

[31] T. Weser, A. Bogen, B. Konrad, R. D. Schnell, C. A. Schug, and W. Steinmann, Phys. Rev. B **35**, 8184 (1987).

[32] G. W. Anderson, M. C. Hanf, P. R. Norton, Z. H. Lu, and M. J. Graham, Appl. Phys. Lett. **66**, 1123 (1995).

[33] T. Weser, A. Bogen, B. Konrad, R. D. Schnell, C. A. Schug, W. Moritz, and W. Steinmann, Surf. Sci. **201**, 245 (1988).

[34] K. T. Leung, L. J. Terminello, J. Hussain, X. S. Zhag, T. Hayashi, and D. A. Shirley, Phys. Rev. B **38**, 8241 (1988).

[35] K. Newstead, A. W. Robinson, S. d'Addato, A. Patchett, N. P. Prience, R. McGrath, R. Whittle, E. Dudzik, and I. T. McGovern, Surf. Sci. **287-288**, 317 (1993).

[36] D. T. Ling, J. N. Miller, D. L. Weissmann, P. Pianetta, P. M. Stefan, I. Lindau, and W. E. Spicer, Surf. Sci. **95**, 89 (1980).

Chapter 7

H_2S on Si(001) and Ge(001)

7.1 Introduction

The low temperature adsorption of H_2S on III-V(110) surfaces is believed to be in a dissociative form, with the presence of SH and H species [1]. The H_2S and H_2O gases on Si(001) [2] and Ge(001) [3] have been investigated using Auger electron spectroscopy (AES) and photoelectron spectroscopy (UPS). It is well-known that both gases show many general similarities.

Schröder-Bergen and Ranke [2] have concluded that at 150 K the adsorption of the H_2S gas on Si(001) shows an abrupt saturation at half a monolayer (ML) coverage. By examining the difference in the photoelectron spectra for the covered and clean surfaces, Schröder-Bergen and Ranke have reported three sharp peaks at the saturation point. Similarly, the Ge(001) surface is fastly covered with the H_2S gas saturating at half a monolayer coverage at 300 K, and is characterized by three intense and sharp peaks [3]. For both surfaces, the three peaks are attributed to the formation of SH species, advocating partial dissociation of H_2S into SH and H. The adsorption of H_2S at an elevated temperature of 550 K on both Si(001) and Ge(001) results in peaks which are attributed to atomically adsorbed sulfur or a surface-sulfide. Ranke and co-workers [2, 3] suggest that the adsorbate is most likely fully dissociated into S and 2H. A similar behaviour has also been recently found for H_2O on Si(001) by Weldon *et al.* [4]. At 625 K, an oxygen insertion into the Si-Si dimer bond is found more favourable than OH dissociation on thermodynamical grounds using both the density functional cluster calculations and surface infrared absorption spectroscopy [4].

The room temperature adsorption of *elemental* sulfur on Si (or Ge) leads to a 1×2 structure for half-monolayer coverage (hemisulfide structure) [5, 6, 4, 7] and the unreconstructed 1×1 structure for full monolayer coverage (monosulfide structure) [6]. The hemisulfide structure is characterized by S-Si bonds involving the Si dimer atoms. In the monosulfide structure the substrate dimer formation is destroyed and S-Si bonds are formed involving all top-layer substrate atoms.

In the present chapter we report *ab initio* theoretical investigations of the atomic geometry, electronic states, and bonding of H_2S on Si(001) and Ge(001). The partially dissociative adsorption of the molecule is considered with a 1×2 reconstruction of the substrate containing IV-IV (IV = Si or Ge) dimers, i.e. containing HS-IV-IV-H bonding structure. For the fully dissociative adsorption we again consider a 1×2 reconstruction of the substrate, but without dimer formation. In this model we thus consider the H-IV-S-IV-H bonding structure. From our calculations we find that the fundamental band gap is free of surface states, with the highest occupied state lying below the valence band maximum for both geometries. Furthermore, we find that the fully dissociated geometry is energetically more favourable than the partially dissociated geometry. Finally a comparison of the band structure for the partially and fully dissociative adsorption models has been made with that for the hemisulfide and monosulfide adsorptions. We find that the H_2S adsorption possesses better passivating property than the adsorption of *elemental* sulfur.

7.2 Results and Discussions

7.2.1 The monohydride-IV(001)-(1×2) surface

First of all we have studied the H-IV(001)-(1×2) monohydride surface. Starting with an asymmetric geometry with a tilt angle of 6^o we placed the H atoms at the dangling bonds positions of the dimer atom on the clean surface. Upon relaxation the IV-IV dimers became symmetric with dimer-bond lengths of 2.40 Å for Si and of 2.43 Å for Ge. The angle between the Si-H bond and the dimer bond was found

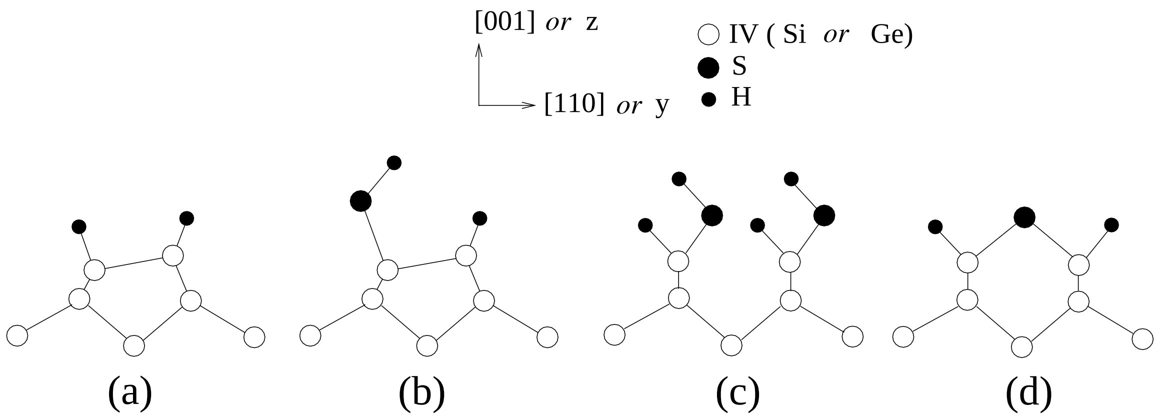

Figure 7.1: Schematic side view of (a) monohydride, (b) and (c) possible partially dissociated H_2S geometries, and (d) fully dissociated H_2S geometry on IV(001).

to be 111.2^o for Si. The Si-H bond length of 1.53 Å is very close to the sum of the corresponding covalent radii ($r_{\mathrm{Si-H}}$=1.47 Å) [8]. Our calculated Si-H bond length is also the same as the value of 1.53 Å calculated by Nardelli *et al.* using both pseudopotential and LMTO methods on the hydrogen covered Si(111) surfaces [9]. For the Ge system, the angle between the Ge-H bond and dimer bond was 111.1^o with the Ge-H bond length of 1.56 Å ($r_{\mathrm{Ge-H}}$=1.52 Å [8]). Both these angles are very close to the tetrahedral angle of 109.5^o. Our calculated Ge-H bond length is nearly identical to the calculated value of 1.55 Å by Rohlfing *et al.* [10] who used a theoretical method similar to ours. The calculated key structural parameters are given in Tab. 7.1 and shown in Fig. 7.2(a).

It is well known that for the constrained *symmetric* dimer model of clean Si(001) and Ge(001) there are two overlapping bands, π and π^*, both being partially occupied [12] (see Chapter 6.2). Upon the adsorption of hydrogen in the monohydride geometry these bands become fully occupied and their energies are lowered down into the bulk valence band. We have identified a total of four occupied states (S_1-S_4) as shown in Fig. 7.4. The total valence charge density and the orbital nature of individual states at the $\bar{K}$ point are shown in Fig. 7.5. Examining the total charge density plot in Fig. 7.5(a), it can be seen that the Si-Si dimer is purely covalent in character as expected, while the Si-H bonds are largely ionic in character with some degree of covalency. The Si-H bond in this work is similar to that calculated

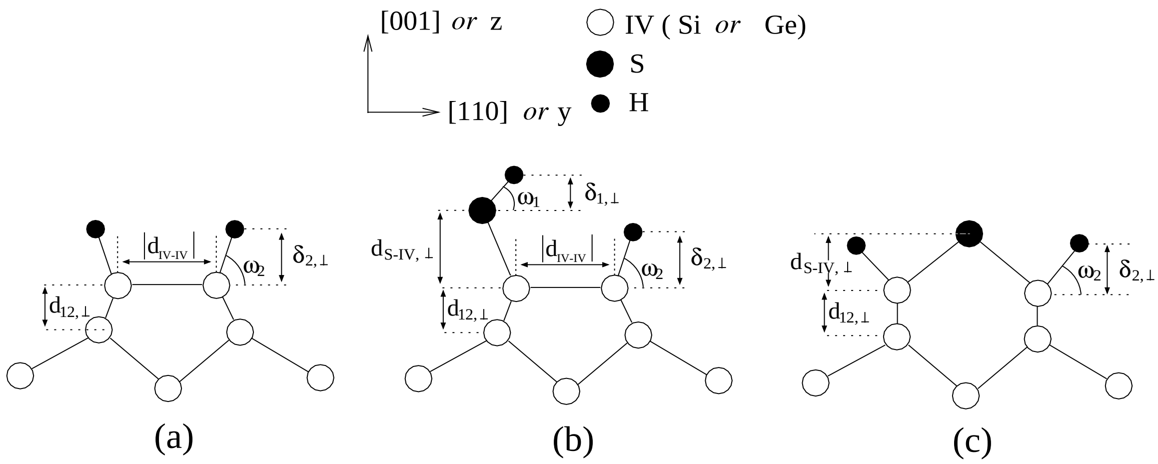

Figure 7.2: Schematic side view with the key structural parameters for (a) monohydride-IV(001)-(1×2), (b) partially dissociated H_2S on IV(001)-(1 × 2), and (c) fully dissociated H_2S on IV(001)-(1×2).

for the SiH_4 system. We modelled SiH_4 molecule inside a repeated cubic box of size 12 Å. The H atoms are placed in the tetrahedral direction with respect to Si atom. The structure was relaxed towards their minimum energy configuration by using four special **k** points. Although we considered three different H pseudopotentials such as Bachelet *et al.*, Gygi [13], and the bare H pseudopotantial, they gave the same bonding picture between the Si atoms and the H atoms. Fig. 7.3(a) shows charactersitic bonding picture between Si and H using the Bachelet *et al.*'s pseudopotential.

The electronic states labelled S_1 and S_2 with the energies between 7 eV - 9 eV below the valence band maximum originate from the hybridization of the s-electron of hydrogen with the σ-bonding (cf. Fig. 7.5(b)) and σ-antibonding (cf. Fig. 7.5(c)) of the dimer atoms. At higher energies we have identified two more states, S_3 and S_4. These originate from the hybridization of the s-electron of hydrogen with the π and π^* orbitals of the surface dimer. The saturation of the Si- and Ge-dimer dangling bonds by hydrogen drives the surface states out of the fundamental gap region. Similar results were found for Ge(001) by Rohlfing *et al.* [10].

	Monohydride structure		Partially dissociative model		Fully dissociative model	
	H-Si-Si-H	H-Ge-Ge-H	HS-Si-Si-H	HS-Ge-Ge-H	H-Si-S-Si-H	H-Ge-S-Ge-H
d_{IV-IV}	2.40	2.44	2.41	2.46	–	–
d_{IV-S}	–	–	2.14	2.18	2.14	2.16
d_{S-H}	–	–	1.40	1.40	–	–
d_{IV-H}	1.53	1.56	1.53	1.56	1.53	1.56
$d_{S-IV,\perp}$	–	–	1.83	1.86	1.22	1.21
$d_{12,\perp}$	1.21	1.23	1.20	1.23	1.33	1.35
$\delta_{1,\perp}$	–	–	0.95	0.94	–	–
$\delta_{2,\perp}$	1.43	1.46	1.46	1.49	1.04	1.07
ω_1	–	–	43.25	42.49	–	–
ω_2	69.56	68.60	72.14	71.70	43.04	43.05

Table 7.1: Calculated values of the structural parameters indicated in Fig.2. Distances are in Å and angles in degrees. Experimental results for the dimer bond length lie in the range 2.20-2.47 Å for the *clean* Si(001) surface and 2.41-2.44 Å for the *clean* Ge(001) surface (see e.g. [11]). Theoretical results for the dimer bond length lie in the range 2.25-2.30 Å for the *clean* Si(001) surface and 2.36-2.46 Å for the *clean* Ge(001) surface (see [11]). All results are obtained with 8 Ry energy cut-off, except indicated otherwise.

7.2.2 Partially dissociated H_2S on Si(001) and Ge(001)

There is no proposed geometry in the literature for the dissociative molecular model on the Si and Ge semiconductors. On the other hand, recently the adsorption of H_2S on III-V(110) has been studied in detail by experimentists and theorists as discussed in Chapter 5. The dissociative molecular model is supported by the observation that the reactivities of different III-V semiconductors scale with the proton affinity of the anion dangling bond [1]. In analogy with the adsorption of H_2S on III-V(110) surfaces, we consider that the $(SH)^-$ species is attached to the lower-lying Si dimer component (whose dangling bond is empty) and the H^+ ion is attached to the upper-lying Si dimer component (whose dangling bond is full) on the clean IV(001)-(1×2) surface. As regards the orientation of the H atom in the $(SH)^-$ complex, we tried two models with all of H, S and Si being in the (001) plane: (i) S-H bond parallel to the Si-H bond and (ii) S-H bond in a direction opposite to

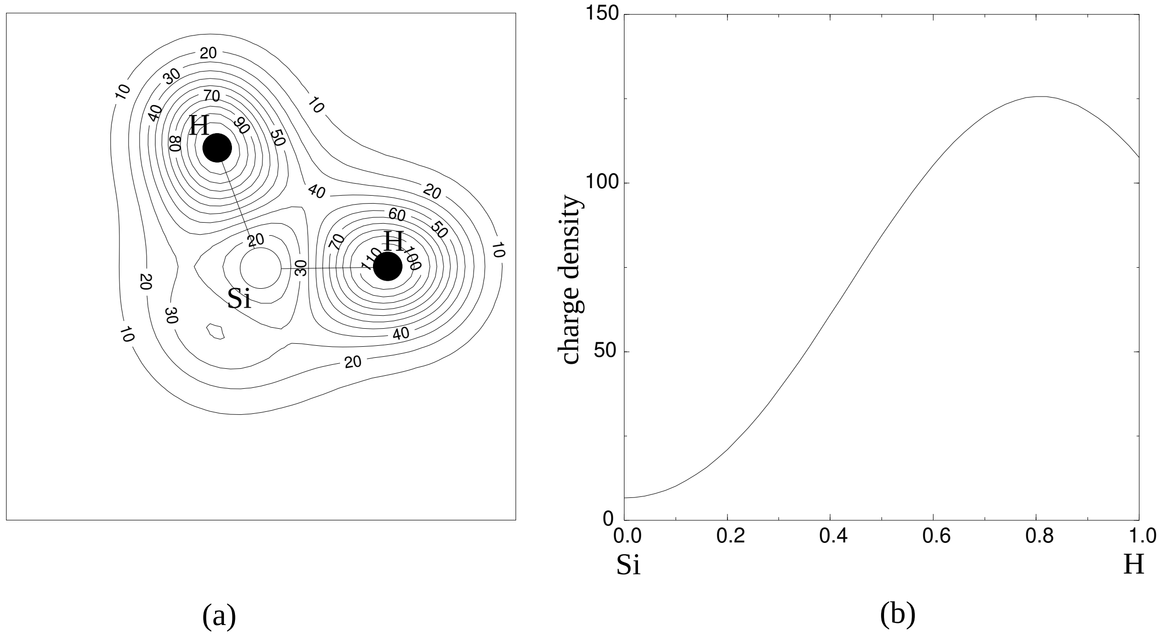

Figure 7.3: (a) Bonding picture of the SiH_4 molecule. Other H atoms are in another plane. (b) One-dimensional charge density plot between Si and H. The maximum charge density is towards the H atom. The charge density values are normalised to 8 electrons per unit cell volume.

that in (i) with respect to the (001) direction. Our energy minimisation procedure suggests that the S atom would stay in the direction of the dangling-bond direction of the lower-lying dimer atom, and the H atom in the $(SH)^-$ complex would stay along the direction given in (i) above and shown in Fig. 7.1(b) (SH-IV-IV-H). The H^+ ion is attached along the dangling bond direction of the upper-lying dimer component.

In Fig. 7.1(c), we show another possible partially dissociated geometry of H_2S on the Si(001) or Ge(001) surfaces with a (1×1) periodicity (one H^+ ion and one $(SH)^-$ complex per Si or Ge atom, Si- or Ge-dimers broken, and Si or Ge atoms in bulk-like sites). For the H_2S-Si(001)-(1×1) system, the calculated value of the adsorption energy with this geometry is 1.2 eV per H_2S molecule higher than that for the partially dissociated case in the (1×2) periodicity. Therefore, the structure in Fig. 7.1(b) was subsequently used in all the partially dissociated cases studied here.

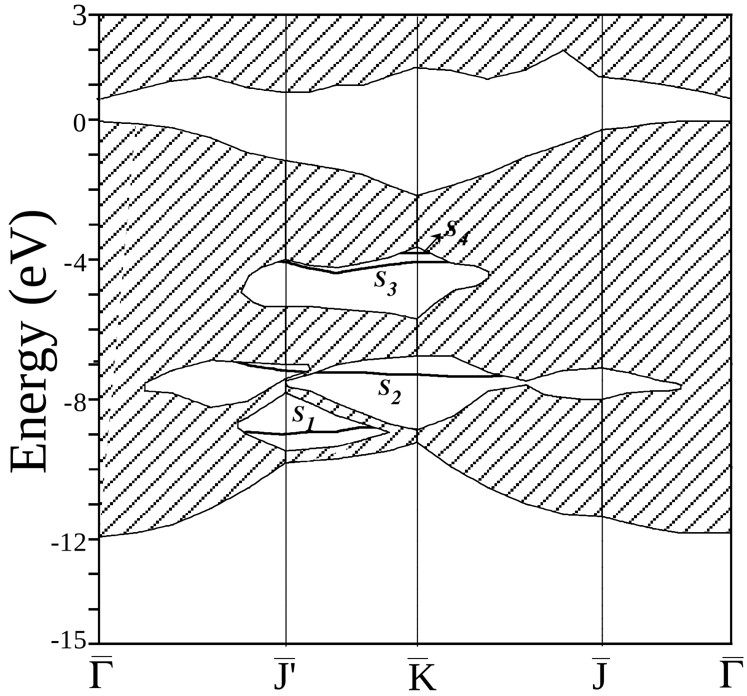

Figure 7.4: Calculated band structure of the hydrogen-terminated H-Si(001)-(1×2) surface. The shaded region is the bulk (1×2) projected band structure for Si and the thick lines represent the occupied surface states.

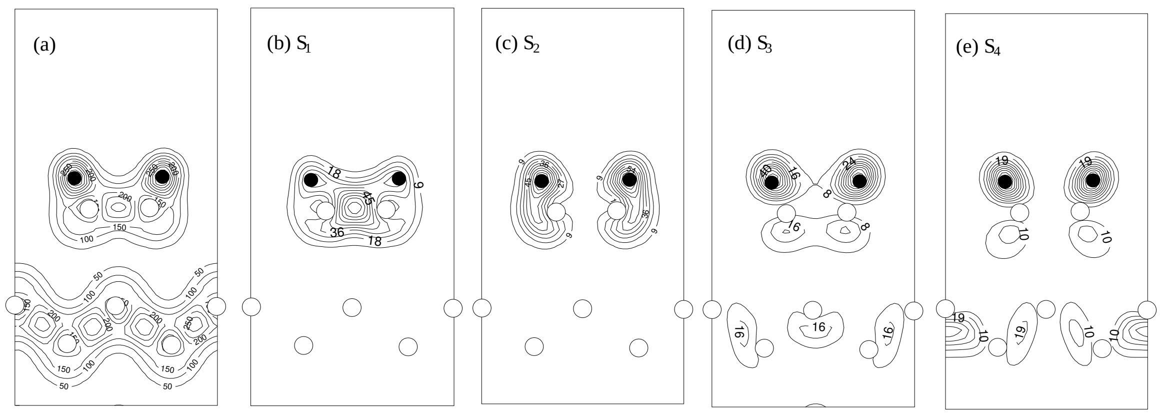

Figure 7.5: Electronic total charge density and electronic charge density plots of the individual states for the monohydride Si(001)-(1×2) structure: (a) on the plane cutting vertically through the Si atoms with the H atoms, (b) the surface state S_1 at $\bar{J}'$, (c) the surface state S_2 at $\bar{K}$, (d) the surface state S_3 at $\bar{K}$ and (e) the surface state S_4 at $\bar{K}$. The electron charge density is normalised to the number of electrons in the supercell (i.e. 70 electrons per unit cell for total charge density plot and 2 electrons per unit cell for the individual electronic states).

7.2.2.1 H_2S on Si(001)-(1×2)

Upon H_2S adsorption on the asymmetric dimer formation of Si(001)-(1×2), we find that the Si-dimer is almost symmetric (tilt angle is about $\sim 2^o$). The dimer bond-length is expanded to 2.41 Å. The calculated Si-H bond length is 1.53 Å, close to the sum of their corresponding covalent radii ($r_{\mathrm{Si-H}}$=1.47 Å) [8]. It is also consistent with the calculated value of 1.53 Å on the H-Si(001)-(1×2) monohyride surface, studied in the previous section. Our calculated S-H bond length is 1.41 Å, somewhat bigger than the sum of their corresponding covalent radii ($r_{\mathrm{S-H}}$=1.34 Å). In Chapter 5 the S-H^- bond length was calculated as 1.38 Å for H_2S-InP(110), 1.40 Å for H_2S-GaAs(110) and 1.41 Å for H_2S-GaP(110). It means that the S-H bond length varies between 1.38 and 1.41 Å upon adsorption of H_2S on semiconductors. The S-Si bond length is 2.15 Å, slightly smaller than the sum of the corresponding covalent radii ($r_{\mathrm{Si-S}}$=2.21 Å) [8]. Our calculated perpendicular distance between the sulphur atom and the Si-dimer, $d_{S-Si,\perp}$, is 1.95 Å. It is somewhat larger than the experimentally measured value of 1.87 Å for a half-monolayer (0.5 ML) coverage of S on Si(001)-(1×2) by Papageorgopoulos *et al.* [6].

The full electronic band structure of this system is shown in Fig. 7.6. We have identified five occupied electronic states. In Fig. 7.7, we show the orbital nature of the electronic total valence charge density (cf. Fig. 7.7(a)) and individuals electronic states (cf. Figs. 7.7(b) to (f) at $\bar{K}$). In Fig. 7.7(a), it can be seen that the Si-Si dimer is purely covalent in character as found in the monohyride case for the Si substrate, while the Si-S bond is partly covalent and partly ionic. The Si-H and S-H bonds are largely ionic in character with some degree of covalency. The calculated surface state S_1 is due to a σ-bonding between S and H. Comparing with our earlier work as studied and discussed in Chapter 5, we can say that upon H_2S adsorption on Si and III-V semiconductors the $(SH)^-$ line appears in the binding energy 12.0-13.4 eV with the same orbital character as shown in Chapter 5. The states S_2, S_3, S_4 are mostly related to orbitals localized between the molecular species and the top-layer substrate. The state S_2 is due to the H *s*-orbital in the $(SH)^-$ complex and has a pronounced contribution from the dimer atoms with a σ-antibonding as seen in Fig. 7.7(c). This state has been seen in the monohyride case for the Si substrate

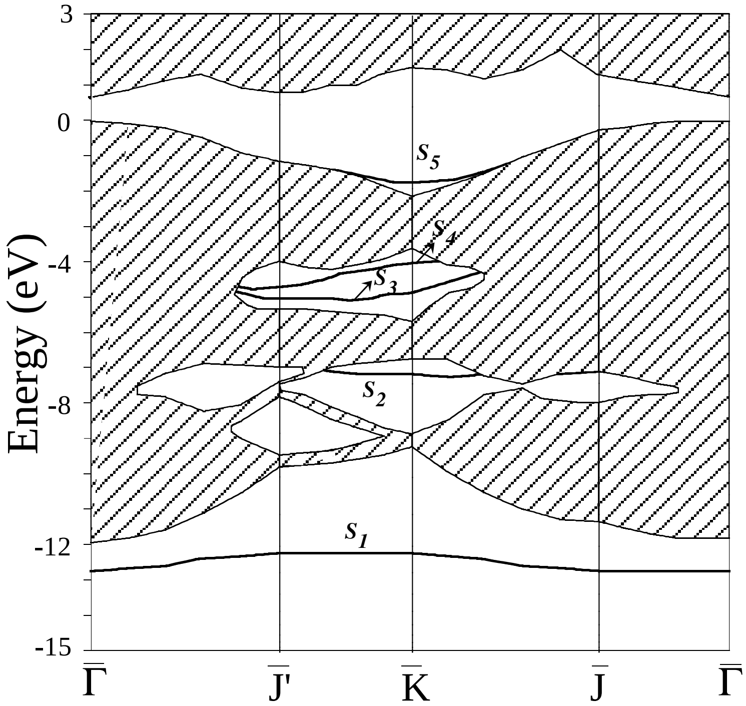

Figure 7.6: Calculated band structure of the partially dissociated H_2S on the Si(001)-(1×2) surface. The shaded region is the bulk (1×2) projected band structure for Si and the thick lines represent the occupied surface bands.

(the state S_2) with almost the same energy level. The state S_3 is mostly due to the H *s*-orbital of the $(SH)^-$ complex and has a small σ-bonding contribution from the dimer back bond with the substrate as shown in Fig. 7.7(d). The surface state S_4 has a complex bonding pattern, with contribution from Si, H and the $(SH)^-$ complex as seen in Fig. 7.7(e). The states S_3 and S_4 can be compared again with the states S_3 and S_4 of the monohydride case for the Si substrate. However, they have now lower energy due to some contribution from the S atom to the system. Another complex bonding picture, involving the Si-Si dimer σ bond orbital and the $(SH)^-$ complex, gives rise to the localised state S_5 at $\bar{K}$ just below the valence band maximum.

7.2.2.2 H_2S on Ge(001)-(1×2)

The calculated Ge-dimer bond length is 2.43 Å. Coincidently, this length is in excellent agreement with the value of 2.44 Å measured using the grazing incidence

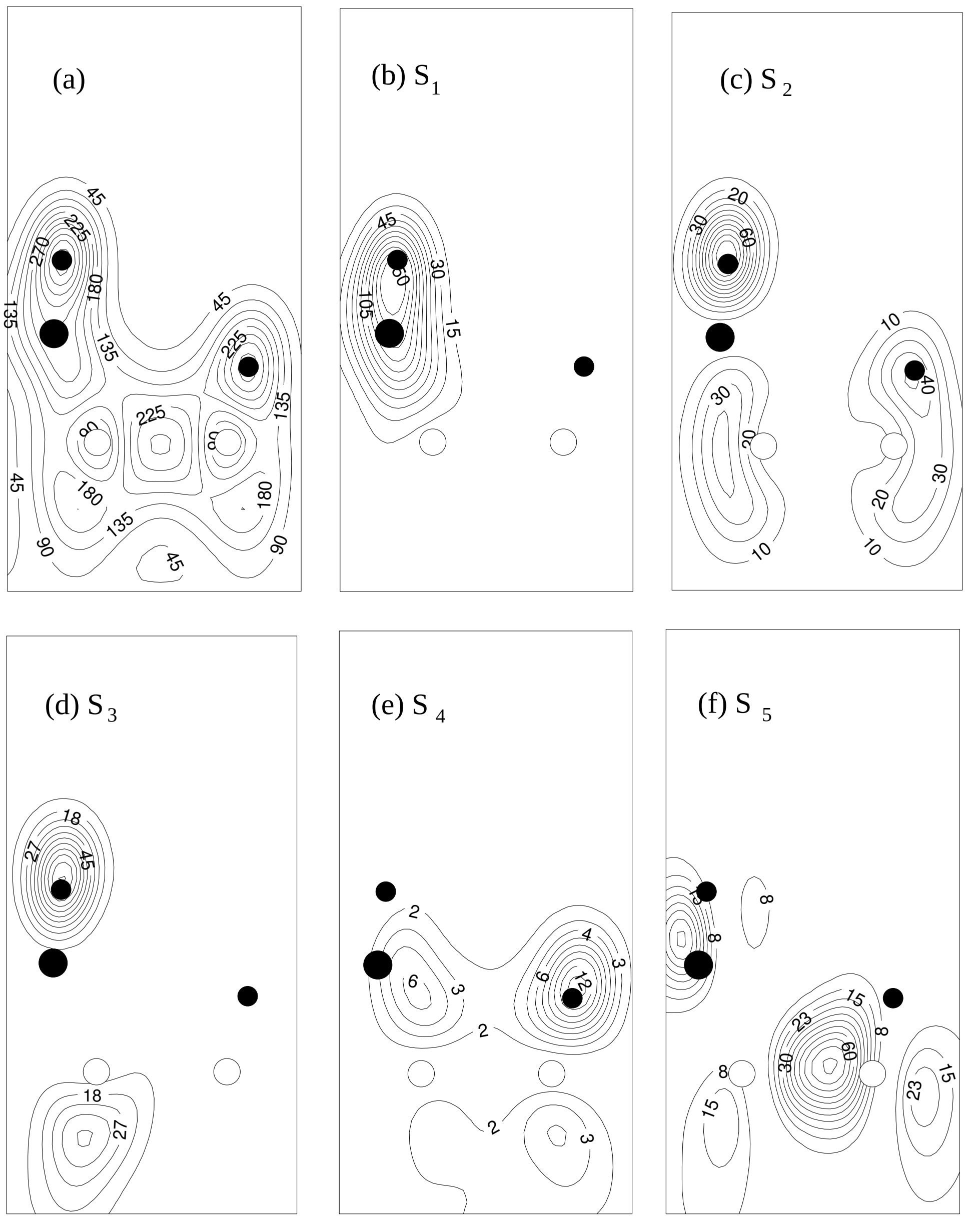

Figure 7.7: Electronic total charge density and electronic charge density plots of the individual states for partially dissociated H_2S on Si(001)-(1×2) structure: (a) on the plane cutting vertically through the Si atoms with $(SH)^-$ line and SiH^+, (b) the surface state S_1 at $\bar{K}$, (c) the surface state S_2 at $\bar{K}$, (d) the surface state S_3 at $\bar{K}$ and (e) the surface state S_4 at $\bar{K}$ and (f) the surface state S_5 at $\bar{K}$. The electron charge density is normalised to the number of electrons in the supercell (i.e. 76 electrons per unit cell for total charge density plot and 2 electrons per unit cell for the individual electronic states).

X-ray diffraction from the clean Ge(001)-(1×2) for an asymmetric dimer [14]. However, it is somewhat bigger than theoretical calculated value of 2.38 Å for the clean Ge(001)-(1×2) surface [15]. The calculated Ge-H bond length is 1.56 Å, close to the sum of their corresponding covalent radii ($r_{\text{Ge-H}}$=1.52 Å) [8]. It is the same as the calculated value of 1.56 Å on the H-Ge(001)-(1×2) monohydride surface. Our calculated S-H bond length is 1.40 Å, somewhat bigger than the sum of their corresponding covalent radii ($r_{\text{S-H}}$=1.34 Å). This calculated bond length is also in the range of 1.38 Å - 1.41 Å upon the adsorption of H_2S on other semiconductors. The S-Ge bond length is 2.20 Å, slightly smaller than the sum of the corresponding covalent radii ($r_{\text{Ge-S}}$=2.26 Å) [8].

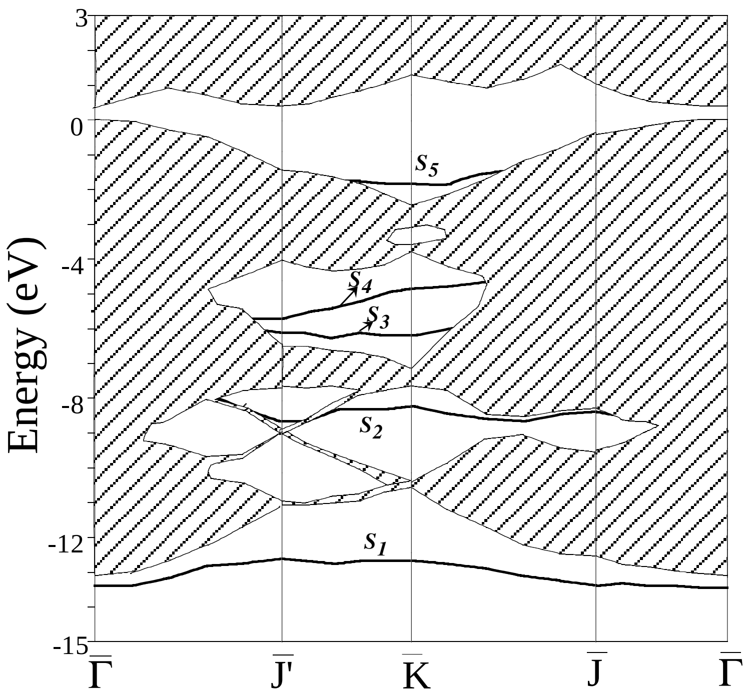

Figure 7.8: Calculated band structure of the partially dissociated H_2S on the Ge(001)-(1×2) surface. The shaded region is the bulk (1×2) projected band structure for Ge and the thick lines represent the occupied surface bands.

We have identified a total of five electronic states, labelled S_1-S_5, as shown in Fig. 7.8. The calculated states S_2, S_3 and S_4 have the same orbital features as for the Si case. These are mostly related to orbitals localised between the molecular species and the top-layer substrate. From the zone-centre UPS measurements at room temperature three intensive and sharp peaks at -3.9, -5.2 and -7.3 eV have been determined by Kuhr and Ranke [3]. While these peaks are in the range of the calculated states S_3 and S_4, detailed angle-resolved UPS measurement along the $\bar{\Gamma}$-$\bar{K}$ or $\bar{J}'$-$\bar{K}$ directions would be helpful to compare our results.

7.2.3 Fully dissociated H_2S on Si(001) and Ge(001)

The elongation of the dimer bond length for both Si(001) and Ge(001) for the partially dissociated geometry signifies weakening of the IV-dimer bond. This weakening is in direct agreement with the suggestion forwarded by Schröder-Bergen and Ranke [2], and Kuhr and Ranke [3] of complete dissociation of the H_2S molecule at high temperature into S and 2H. We find that the fully dissociated geometry as shown in Fig. 7.1(d) is energetically more favourable than the partially dissociated case, lying 0.59 eV lower for Si(001) and 0.56 eV lower for Ge(001). The calculated key structural parameters are given in Tab. 7.1 and shown in Fig. 7.2(c). Our finding about the relative energetics of the partially and fully dissociative models is in full agreement with the recent work by Weldon *et al.* [4] for the adsorption of H_2O on Si(001).

7.2.3.1 H_2S on Si(001)-(1×2)

Upon relaxation of the fully dissociated adsorption of H_2S on Si(001), the change in the Si atomic positions is negligible, resulting in an almost ideal-like situation. For example, the bond length between the topmost Si atom and the rest of the substrate is the same as the ideal bulk bond length. The calculated perpendicular distance between the sulphur atom and the topmost Si layer, $d_{S-Si,\perp}$, is 1.22 Å. It is a little bigger than the experimentally measured value of 1.09 Å for the 1 ML elemental S adsorption on Si(001)-(1×1) by Papageorgopoulos *et al.* [6]. This value is intermediate to the experimentally measured values of 1.87 Å and 1.09 Å for the adsorption of 1 ML and 0.5 ML of *elemental* S, respectively. In our calculation the perpendicular distance of the S atom from the top substrate layer has decreased from 1.95 Å for the partially dissociated model to 1.22 Å for the fully dissociated model. The calculated Si-S bond length is 2.14 Å (r_{Si-S}=2.21 Å [8]), i.e.

approximately the same as in the case of partial dissociation. The perpendicular distance between the topmost Si layer and the second topmost Si layer, $d_{12,\perp}$, is elongated from 1.21 Å to 1.33 Å. Another interesting geometrical change occurs on $\delta_{2,\perp}$. The hydrogens atoms have now come closer to the topmost Si substrate. All these geometrical changes give rise to more stable surface and energetically more favourable system since this system lies 0.59 eV lower in energy than the partially dissociated H_2S on Si(001) as mentioned before.

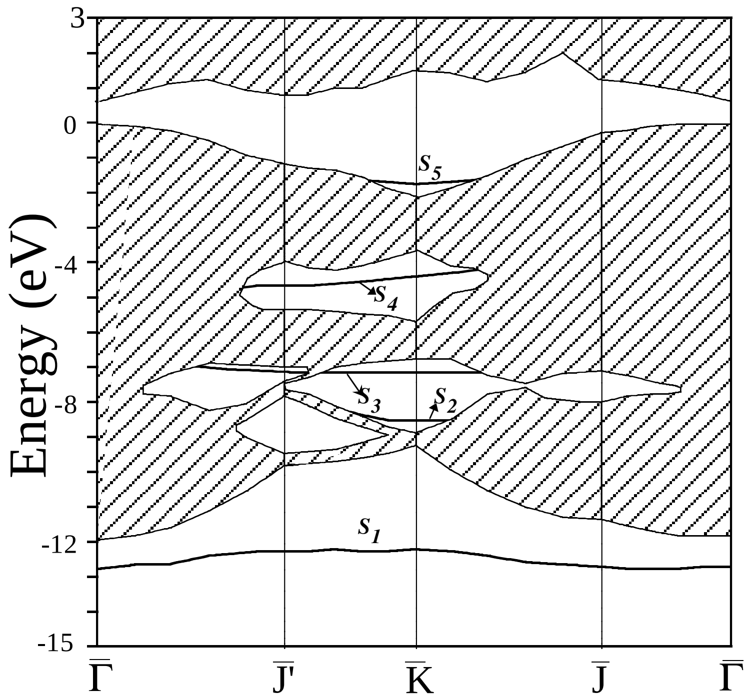

Figure 7.9: Calculated band structure of the fully dissociated H_2S on the Si(001)-(1×2) surface. The shaded region is the bulk (1×2) projected band structure for Si and the thick lines represent the occupied surface bands.

We have identified a total of five occupied electronic states, as shown in Fig. 7.9. In Fig. 7.10 we have shown to total and partial charge density plots for the fully dissociated H_2S on Si(001)-(1×2) surface. Fig. 7.10(a), plotted on the plane cutting vertically through the S and H atoms, and the first-topmost Si layer, reveals that the S-Si bond is polar covalent: with a large degree of covalency and with some ionic character, giving rise to a shift in the peak towards the more electronegative species S (the maximum charge density in the S-Si bond is closer to the S atom).

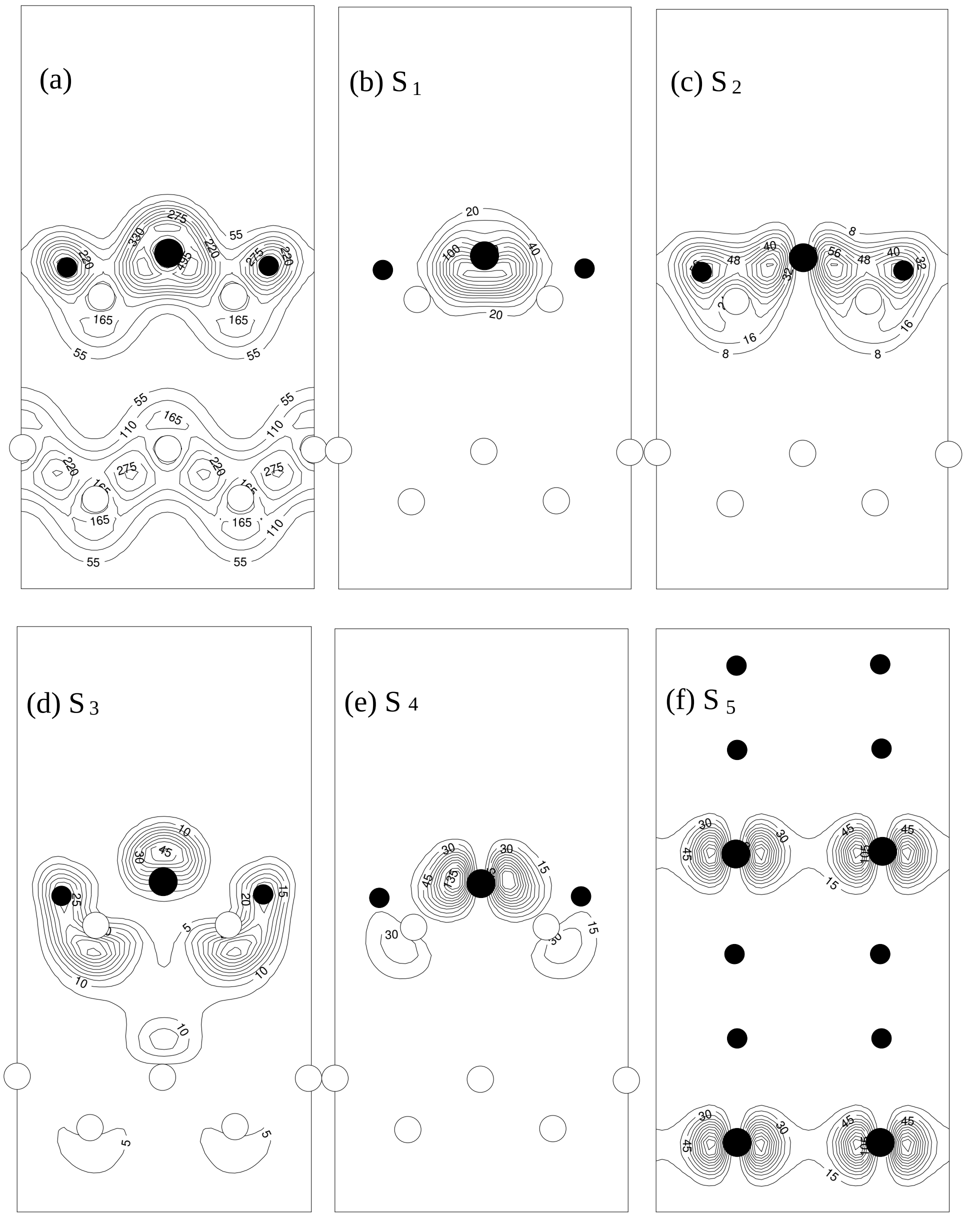

Figure 7.10: Electronic total charge density and electronic charge density plots of the individual states for the fully dissociated H_2S on Si(001)-(1×2) structure: (a) on the plane cutting vertically through the S atom and the Si atoms with the SiH lines, (b) the surface state S_1 at $\bar{K}$, (c) the surface state S_2 at $\bar{K}$, (d) the surface state S_3 at $\bar{K}$ and (e) the surface state S_4 at $\bar{K}$ and (f) surface state S_5 at $\bar{K}$, on the plane cutting horizontally through the S atoms and the H atoms. The electron charge normalisation is the same as in Fig. 7.7.

This indicates that the Si end is slightly positively charged. This is entirely consistent with the chemical shift observed in the work of Papageorpoulos *et al.* [6], which shows strong interaction between S and Si with a covalent bond character. In addition, the Si-H bonding is largely ionic in character with some degree of covalency, with the maximum charge density being is closer to the H atom. The Si-H bonding is also similar to that calculated for the SiH_4 system. The surface state S_1 is due to the s-orbital of the S atom as seen in Fig. 7.10(b). The UPS measurements by Schröder-Bergen and Ranke [2] at 550 K show three spectra at -3.0, -5.7 and -7.2 eV. We calculated three states in the binding energy from -4.5 to -8.5 eV, labelled S_2, S_3 and S_4. They are now related to S-, hydrogen-substrate bondings of the system. The state S_2, examining its charge density plot shown in Fig. 7.10(c), is due to the orbitals of S and H involved in Si-S and Si-H bonding. The surface state S_3 has a complex bonding pattern, with contribution from the sp_z orbital of the S atom, s-orbital of the H atoms and the Si back bond with the substrate. The state S_4 is mainly contributed from the p_y-orbital of the S atom as seen in Fig. 7.10(e). The highest occupied state S_5, plotted on a horizontal plane and shown in Fig. 7.10(f), is derived from the lone-pair p_x orbitals of the S atoms.

7.2.3.2 H_2S on Ge(001)-(1×2)

The fully dissociative adsorption of H_2S on Ge(001) is similar to that on Si(001), with the same sort of geometrical changes (cf. Tab. 7.1). This system is also energetically more favourable, lying 0.56 eV lower in energy than the partially dissociated H_2S on Ge(001).

We have identified a total of five occupied electronic states as shown in Fig. 7.11. These have the same orbital character as seen in the Si case. The zone-centre UPS measurement by Kuhr and Ranke [3] at 550 K shows four intensive peaks at located -8.5, -4.8, -3.8 and -1.8 eV. Our calculated state S_3, S_4 and S_5 can be matched with the peaks -8.5, -4.8 and -1.8 eV, respectively. However, we cannot identify the experimentally observed surface state around -3.8 eV. As we have explained before, the orbital features of S_3, S_4 and S_5 are mainly contributed from the S atom.

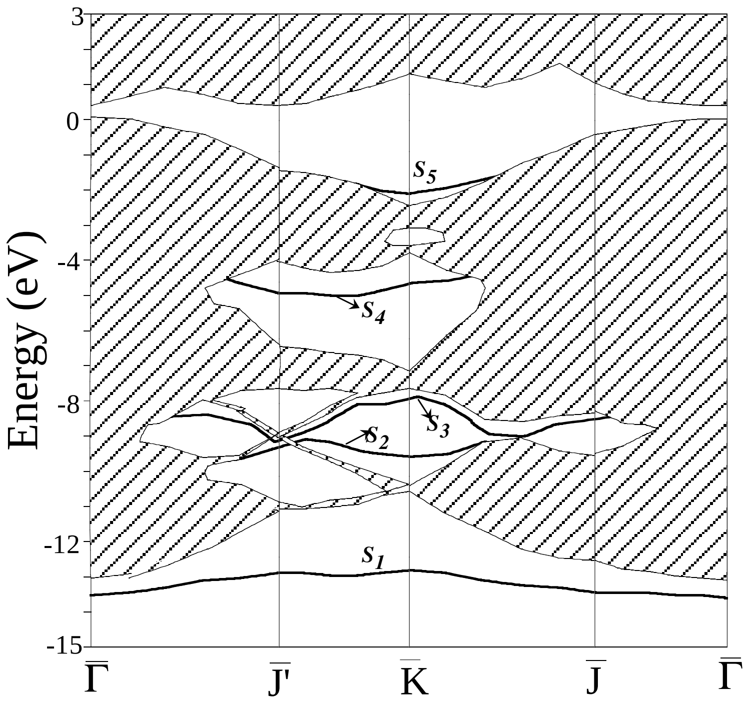

Figure 7.11: Calculated band structure of the fully dissociated H_2S on the Ge(001)-(1×2) surface. The shaded region is the bulk (1×2) projected band structure for Ge and the thick lines represent the occupied surface bands.

7.2.4 Monolayer deposition of elemental sulfur on Ge(001)-(1×1)

For a monolayer coverage of elemental sulfur on Ge(001)-(1×1) we have identified a total of six occupied and one unoccupied surface states as shown in Fig.6.12. We have also displayed the photoelectron spectra measured along the $\bar{M} - \bar{\Gamma} - \bar{J}$ symmetry direction [7]. Our calculated surface states $S_3{}^s$, $S_4{}^s$ and $S_5{}^s$ can be compared with the experimental spectra. While the dispersion of the calculated and measured states are similar, we note that the calculated states are systematically higher in energy than the measured states. A similar energy difference between experiment and theory has also been observed by Rohlfing *et al.* using quasiparticle band calculation approach [10].

There is a close resemblance between the sulfur related states for the elemental covered surface and the fully dissociated H_2S covered surface. We have distinguished the states for the elemental sulfur coverage with a superscript 's', i.e states labelled

S_i^s (cf. Fig.6.14). The state S_1^s has the same bonding character as the state S_1. The state S_2^s is related to the bonding between Ge and S, while the state S_2 is related to the Ge-S and Ge-H bondings. The state S_3^s is similar to S_3 but is resonant with the bulk bands. The states S_4^s and S_4 are also similar in nature. We have not been able to identify the equivalent of the S_5^s state on the H_2S covered surface. The state S_6^s is similar to the S_5 state. In addition, for the elemental sulfur coverage the lowest unoccupied state S_7^s lies inside the bulk band gap and is made up of the sp_z orbitals from S and Ge. A similar comparison can be made between the electronic band structure of the fully dissociative model for H_2S-Si(001) (shown in Fig. 7.9) and the monosulfide structure for S-Si(001) (shown in Fig. 6.5).

7.3 Summary

We have presented a detailed investigation of the equilibrium atomic geometry, electronic states and bonding of the partially and fully dissociated of H_2S molecule on the Si(001) and Ge(001) surface. Our results are compared with available experimental and theoretical results. The fully dissociated geometry is found to be energetically more favourable than the partially dissociated one. In general the adsorption of H_2S on the Si(001) and Ge(001) surfaces shows similar behaviour. For both the partially dissociated and fully dissociated geometries studied here the fundamental band gap is free of surface states, with the highest occupied state close to the valence band maximum. More experimental results on geometry and band structure are desirable to compare with our work.

Bibliography

[1] E. Dudzik, A. Leslie, E. O'Toole, I. T. McGovern, A. Patchett, D. R. T. Zahn, J. Ludecke, D. P. Woodruff and B. C. C. Cowie, J. Phys.: Condens. Matter **8**, (1996) 15.

[2] E. Schröder-Bergen and W. Ranke, Surf. Sci. **236**, 103 (1990).

[3] H. J. Kuhr and W. Ranke, Surf. Sci. **189/190**, 420 (1987).

[4] M. K. Weldon, B. Stefanov, K. Raghavachari, and Y. J. Chabal, Phys. Rev. Lett. **79**, 2851 (1997).

[5] P. Moriarty, L. Koenders, and G. Hughes, Phys. Rev. B **47**, 15950 (1993).

[6] A. Papageorgopoulos, A. Corner. M. Kamaratos, and C. A. Papageorgopoulos, Phys. Rev. B **55**, 4435 (1997).

[7] T. Weser, A. Bogen, B. Konrad, R. D. Schnell, C. A. Schug, W. Moritz and W. Steinmann, Sur. Sci.**201**, 245 (1988).

[8] G. Burns, *Solid State Physics*, International Edition (Acedemic Press) 1990.

[9] M. B. Nardelli, F. Finocchi, M. Palummo, R. Difelice, C. M. Bertoni, F. Bernardini, and S. Ossicini, Surf. Sci. **269/270**, 879 (1992).

[10] M. Rohlfing, P. Krüger, and J. Pollmann, Phys. Rev. B **54**, 13759 (1996).

[11] G. P. Srivastava, Rep. Prog. Phys. **60**, 561 (1997).

[12] P. Krüger and J. Pollmann, Phys. Rev. Lett. **74**, 1155 (1995).

[13] F. Gygi, Phys. Rev. B **48**, 11692 (1993).

[14] R. Rossmann, H. L. Meyerheim, V. Jahns, J. Wever, W. Mortiz, D. Wolf, D. Dornisch, and H. Schultz, Surf. Sci. **279**, 199 (1992).

[15] H. M. Tütüncü, S. J. Jenkins and G. P. Srivastava, Phys. Rev. B **57**, (1998) 4649.

Chapter 8

Concluding Remarks

8.1 Summary of Results

In chapter 2 of this thesis, *ab initio* calculations based on pseudopotentials and the density functional theory have been briefly discussed in conjunction with the computational technique using the EKSETER code. We have used this code to investigate the equilibrium atomic geometry, electronic states and bonding of semiconductor surfaces. In chapter 3 of this thesis, some experimental techniques have been discussed with their basic concepts.

In chapter 4 of this thesis, we have investigated the equilibrium atomic geometry, electronic states and bonding of S adsorbates on the InP(110) surface with (1×1) periodicity. For non-reacted half-monolayer coverage of S, we find that the interchain bridging geometry has the lowest total energy. For non-reacted full monolayer coverage, the epitaxially continued layer structure is found to be the most energetically favourable and it exhibits a good semiconducting nature. We have also studied four geometrical models which involve the reaction of S atoms with the substrate. For an ordered reacted model with the adsorbate S atoms exchanged with their neighbouring P atoms, the average vertical distance between the top two layers is 1.98 Å, which is in agreement with a recent result obtained from x-ray standing wave analysis (1.95 Å), but is characterized by a small band gap.

In chapter 5 of this thesis, we have investigated the equilibrium atomic geometry, electronic states and bonding of the H_2S molecule on the InP(110), GaAs(110) and

GaP(110) surfaces within a dissociative adsorption model. In general the adsorption of H_2S on the three semiconductors shows similar behaviour. The calculated average distances between the topmost InP, GaAs and GaP layer and the sulphur atom are 1.87, 1.67, and 1.65 Å, respectively. In all the cases studied here, the fundamental band gap is free of surface states, with an occupied surface state close to the valence band maximum. The calculated electronic states are in agreement with reported angle-resolved photoemission data.

In chapter 6 of this thesis, we have presented in detail the equilibrium atomic geometry, electronic states and chemical bonding for the adsorption of elemental S on Si(001). Following recently reported room temperature LEED, AES, TDS and WF measurements, three different adsorption models have been studied: hemisulfide-(2×1) structure, monosulfide-(1×1) structure, and disulfide-(1×1) structure. For hemisulfide and monosulfide structures, the calculated location of S above the Si(001) surface is in excellent agreement with experiment. The disulfide structure is, however, characterized by strong covalent bonds between the second-layer S and the second-layer Si substrate. This is accompanied by a substantial weakening of the covalent bond between the Si atoms in the second and third substrate layers. We suggest that this weaking of the interlayer Si-Si bonding in favour of the formation of SiS units provides a signature of sulfur desorption as seen in experiment. An analysis of surface free energy suggests that, in the allowed range of S chemical potential, the monosulfide structure is more stable than the hemisulfide and disulfide structures. Following this result we have also investigated the equilibrium atomic geometry, electronic states and chemical bonding for the adsorption of elemental S on Ge(001) within the monosulfide-(1×1) structure. The calculated electronic states are in modaret agreement with reported ARPES spectra. We have also considered that desorption may take place with the unit of GeS.

In chapter 7 of this thesis, the EKSETER code has again been used to investigate the equilibrium atomic geometry, electronic states and bonding of the H_2S molecule on the Si(001) and Ge(001) surfaces within two dissociative adsorption geometries. First we consider adsorption of partially dissociated species $(SH)^-$ and H^+ onto the Si- or Ge-dimer with a $(1{\times}2)$ surface periodicity. Secondly, we consider adsorption of fully dissociated species S and 2H on the surface with a $(1{\times}2)$ periodicity but without dimer formation. In general, the adsorption of H_2S on the Si(001) and Ge(001) surfaces show similar behaviour. For both geometries studied here, the fundamental band gap is free of surface states, with the highest occupied state lying below the valence band maximum. However, we find that the fully dissociated geometry is energetically more favourable than the partially dissociated case, lying 0.59 eV lower for Si(001) and 0.56 eV lower for Ge(001).

8.2 Future Work

8.2.1 Adsorption of Te on Si(001)

Adsorption structures of Te on a Si(001) surface have been investigated by LEED, thermal desorption spectroscopy and AES [1, 2, 3]. Te is used as a surfactant to compose a Ge/Si heterogeneous structure, because the Ge/Si interface with Te is much sharper than that without Te. It has been proposed that less than 1 ML Te atoms react directly to dangling-bond of Si(001). For more than 1 ML Te atoms, Te atoms desorb at about 350 °C and the (1×1) structure appears. Thus, another direction for future work might be to study the adsorption and desorption of Te on and off Si(001) theoretically.

8.2.2 Si_2H_6 and Ge_2H_6 on the group-IV(001) surfaces

Recently, many experimental growth process have been carried out using Si_2H_6 (disilane) and Ge_2H_6 (digermane) on a Si(001) and a Ge(001) surface [4, 5, 6, 7, 8, 9, 10, 11]. Surface processes during chemical vapor deposition (CVD) and the atomic-layer epitaxy (ALE) of group-IV elements have currently received extensive interest. The Si_2H_6 molecule is exposed to the Si(001) surface in the ALE process. The Si(001)-(2×1) surface adsorbs a 0.5 ML of dissociated fragments (SiH_3 trihydride and SiH_2 dihydride) at more than 400 K and then above 700 K it decomposes to surface monohydride, SiH, through several intermediate steps. The same procedure can happen using the digermane on Si(001) (or Ge(001)) surface at the difference temparatures. On theoretical side, there is no available study for these systems. It would therefore be interesting, and rewarding, to study all the intermediate dissociation steps of disilane and digermane on Si and Ge in order to explain the bonding pictures and electronic band structures.

8.2.3 Growth Simulations

The molecular dynamics (MD) method has been known for several decades and has been used succesfully in atomistic simulation models of thousands of interacting particles to describe structural and dynamical properties of simple physical systems. It is impossible to study such a big system using *ab initio* method even with supercomputers. Simulations with only a few thousands atoms are generally too small to capture realistic densities of defects and growing mechanism. These kinds of simulations help us understand roughening transitions during epitaxial growth, for example, in the manufacture of high quality semiconductor devices.

The classical MD method concerns the solution of Newton's equation of motion for N interacting particles. This general N-body problem involves the calculation of N(N-1)/2 pair interactions in order to compute the total force on any given particle;

$$m_i \frac{d^2 r_i}{dt^2} = -\sum_{i \neq j} \frac{\delta V_{ij}(|\mathbf{r}_j - \mathbf{r}_i|)}{\delta \mathbf{r}_i}. \tag{8.1}$$

The problem of modelling a material can therefore be restated as that of finding a potential function V for that material. The Lennard-Jones potential, is a typical pairwise potential and probably the most common used one. This potential is very suitable for rare gases, where no electrons are available for bonding and atoms are attracted to each other solely through the weak van der Waals forces. However, a system of interacting atoms is really made up of nuclei and electrons which interact with each other. Nowadays, there are a few such many-body potentials for semiconductors. For example, the Stillinger-Weber potential is one of the first attempts to model a semiconductor with a classical model [12]. It is based on a two-body term and a three-body term;

$$V = \frac{1}{2}\sum_{ij} \psi(r_{ij}) + \sum_{i<j<k} h(r_{ij})h(r_{ik})\left(\cos\theta_{jik} + \frac{1}{3}\right)^2 \tag{8.2}$$

where θ_{jik} is the angle between $\mathbf{r}_j$ and $\mathbf{r}_k$ subtended at vertex i and *h(r)* is a decaying function, where angles are as close as possible to the ideal tetrahedral structure and making this structure more stable than compact structure. Another familiar potential has been developed by Tersoff [13]. It depends on the concept of bond order. This means that the strength of a bond between two atoms is not constant. In a semiconductor, the focus is on bonds rather than atoms.

After the potential between the atoms has been modelled, one needs to considere the time integration of the equation of motion of the interacting particles and follow their trajectories. Most commonly used time integration algorithm is probably the Verlet algorithm [14]. Using interatomic potential and this algorithm, the growing kinetics of semiconductors may be researched. However, this type of potential uses a rich parametric data. Recently, a scheme called 'force matching method' [15] has been developed. It consists of a numerical matching procedure which tries to match as closely as possible *ab initio* derived forces with a classical potential. Therefore, information from *ab initio* calculations can be usefully included in classical MD simulations of complicated semiconductor growth process. This work is still in its early stages.

Bibliography

[1] K. Tamiya, T. Ohtani, Y. Takeda, T. Urano and S. Hongo, Surf. Sci. **408**, 268 (1998).

[2] T. Ohtani, K. Tamiya, Y. Takeda, T. Urano and S. Hongo, Surf. Sci. **130**, 112 (1998).

[3] S. Higuchi and Y. Nakanishi, J. Appl. Phys. **71**, 39 (1992).

[4] Deng-Sung Lin, Surf. Sci. **402**, 831 (1998).

[5] Y. Suda, Y, Misato, D. Shiratori, K. Oryu, and M. Yamashita, Appl. Surf. Sci. **130**, 304 (1998).

[6] K-H. Huang, T-S. Ku, and D-S. Lin, Phys. Rev. B. **56**, 4878 (1997).

[7] M. Fehrenbacher, J. Spitzmüller, M. Pitter, H. Rauscher, and R. J. Behm, Jpn. J. Appl. Phys. **36**, 3804 (1997).

[8] J. Spitzmüller, M. Fehrenbacher, M. Pitter, H. Rauscher, and R. J. Behm, Phys. Rev. B. **55**, 4659 (1997).

[9] X. F. Hu, Z. Xu, D. Lim, M. C. Downer, P. S. Parkinson, B. Gong, G. Hess, and J. G. Ekerdt, Appl. Phys. Lett. **71**, 1376 (1997).

[10] D-S. Lin, K-H. Huang, T-W. and Pi, R-T. Wu, Phys. Rev. B **54**, 16958 (1996).

[11] D. Steinmetz, S. Van, F. Ringeisen, D. Bolmont, J. J. Koulmann, Surf. Sci. **307**, 253 (1994).

[12] F. Stillinger and T. A. Weber, Phys. Rev. B **31**, 5262 (1985).

[13] J. Tersoff, Phys. Rev. B **37**, 6991 (1988).

[14] L. Verlet, Phys. Rev. **159**, 98 (1967) and Phys. Rev. **165**, 201 (1967).

[15] F. Ercolessi and J. B. Adams, Europhys. Lett. **26**, 583 (1994)